CONVECTIVE MIXING IN THE EARTH'S MANTLE

by

Michael Christopher Gurnis

A Thesis Submitted for the Degree of
DOCTOR OF PHILOSOPHY
of
THE AUSTRALIAN NATIONAL UNIVERSITY

October, 1986

This thesis is the result of research performed during the period October, 1983 to October, 1986 while I was a full-time student at the Research School of Earth Sciences, Australian National University. This work is entirely my own, unless otherwise acknowledged. This thesis has never been submitted to another University or similar institution

Michael C. Gurnis

Michael C. Gurnis
October, 1986

ACKNOWLEDGEMENTS

I wish to thank the many individuals at RSES who have helped bring this research to fruition. I wish to thank: Herb McQueen for his patient assistance with the many mathematical problems which arose; Malcolm McCulloch and Bill McDonough for many hours of discourse on the chemical aspects of geodynamics; Ross Griffiths for sharing his clear understanding of fluid dynamics, for his comments on my papers (which later made their way into this thesis), and for introducing me to some experimental fluid mechanics during my final months; Greg Houseman for often playing the devil's advocate, especially during my mid-course, and, by so doing, helped sharpen my thinking; and Mark Richards for bring fresh and exciting new ideas from California on how the Earth may work. I sincerely thank Geoff Davies, my conscientious and humble supervisor, for molding me into a clear thinking scientist; for giving me a research topic on the very forefront of geodynamics and letting me take off with it; for untold of hours discussing how the earth works (and especially the merits of whole-mantle convection); for reading my many papers and for adding the crucial punch line at the beginning of each one; for putting up with a reclusive and often cranky student for four years; for being completely honest about his plans to come to Australia; and finally for carefully reading this thesis.

ABSTRACT

The process by which subducted lithosphere is mixed by plate-scale mantle convection is investigated in numerical calculations. The results show that the observed isotopic heterogeneity of mantle sources and their ancient (1-2 b.y.) apparent ages are consistent with convective mixing.

The perimeter of small, initially circular, heterogeneities are followed in unsteady, periodic flows. It is shown that after tens of transit times (one transit time is the time to traverse the fluid depth with the boundary velocity) that there are always relatively large-sized blobs (on the order of the initial dimension). Heterogeneities survive because they are primarily stirred by laminar mixing and because they are frequently transferred to adjacent convection cells where they are partially unmixed by laminar flow. In particular, it is shown for whole-mantle convection that for an initial 10 km sized heterogeneity there will still be, on average, one 1 km sized heterogeneity after 3.3 b.y. of stirring, even assuming the mantle was convecting much more rapidly in the past.

Mixing calculations have been primarily carried out in two-dimensional thermal convection calculations which incorporate features of the mantle-mixing system: plate kinematics (including its intrinsic unsteadiness), introduction of chemical heterogeneity at converging plate margins (subduction), and sampling of heterogeneities near diverging margins (sub-ridge magmatism). If the heterogeneity is initially injected as a sheet on the margin of unsteady cells, it is mixed by laminar flow, because the thickness of the sheet is smaller than the scale of flow. Clumps of passive tracers, corresponding to sizable "blobs", survive for 40 transit times in constant viscosity flows with plausible plate evolution models. This survival time scales to > 1 b.y. for whole-mantle convection. If the viscosity through the box increases with depth, then chemical heterogeneity survives for 100 transit times if $\bar{\eta}/\eta_0$ (e.g. average viscosity normalized by the value at the top) > 50. If the tracers are made intrinsically "heavy", they tend to segregate to the base of hot-upwelling regions and form discontinuous aggregations. However, only for densities appropriate for pure oceanic crust can any significant amount of segregation take place.

Despite the survival of chemical heterogeneity, the average time passive tracers remain in the box from subduction at trenches to sampling at ridges (i.e., the residence time) is within 20% of the mean residence time expected from an analytic model in which tracers are assumed to be sampled randomly. Model ages of the mantle that explicitly incorporate both increased convection rates in the past and random sampling of heterogeneities bracket the ~ 1-2 b.y. apparent Pb-Pb and Rb-Sr isochrons of midocean ridge basalts and oceanic island basalts. If $\bar{\eta}/\eta_0 > 50$, then recycled material is sampled before it has time to be stirred into the basal regions; consequently, the average age of recycled material cannot be made much larger than ~ 2 b.y. assuming a realistic thermal history. If an exponential viscosity distribution is used and $\bar{\eta}/\eta_0 > 50$, then segments of mantle, initially in the basal parts of the flow, can survive sampling and significant stirring for > 4.5 b.y. This suggests that rare gas isotopic systematics are consistent with whole-mantle convection.

TABLE OF CONTENTS

CHAPTER 1
INTRODUCTION

The lateral motion of continents and the spreading and subduction of sea floor are the result of the largest scale and perhaps the most fundamental processes of geological activity. The observed lateral motion of the earth's surface is an expression of a thermally convecting mantle. Convection is the process by which heat, principally generated by radioactive decay, is removed from the interior. Understanding how this process operates and how it has varied over the course of the 4.5 b.y. history of the earth is a premier goal of the earth sciences.

Direct measurements of flow in the deep interior are not possible and we must rely on indirect observations from both geophysics and geochemistry. Geophysical observations like the gravity field, seismic velocity structure, and the present configuration and motions of lithospheric plates, provide detailed constraints on how convection presently operates, but give few constraints on how convection has behaved over earth history. However, geochemical observations, in particular isotopic systematics of mantle derived rocks, provide important constraints on time-integrated properties of the convecting system over much of its several billion year history. In particular, the radiogenic isotopic ratio of a mantle derived rock can constrain two features of its mantle source: its time integrated chemical composition and the length of time it has remained distinct or isolated from other segments of the earth. Isotopic observations trace where a mantle component has come from, how its has been modified, and the time it has survived in the mantle. In order to exploit such isotopic observations in our efforts to infer aspects of mantle convection, we must understand how mantle convection mixes chemical heterogeneities. Through an understanding of mixing, we can relate geophysical and geochemical observations to provided a unified picture of mantle processes.

This thesis was motivated, in part, by two fundamental features of the mantle: that it has isotopic heterogeneities on many scales persisting for billions of years and that chemical heterogeneities are injected into the mantle at subduction zones. These observations provide the basis for a number of first order questions relevant to both geophysics and geochemistry. First, if the mantle is convecting with velocities O(1-10 cm/yr) how can chemical heterogeneities persist for 1-2 b.y. ? Second, what kind of mixing is experienced by parcels of fluid which are injected on the edge of convection cells, or in other words, what is the ultimate fate of subducted oceanic lithosphere and oceanic crust?

The approach employed is primarily a forward modeling one, in that mixing is explored in model flows which were developed in response to geophysical observations. The research presented in this thesis falls within the realm of computational fluid dynamics, the discipline where the basic fluid dynamic equations of complex physical situations are solved on a computer.

1.1 Two Simple Examples of Mixing

In order to introduce some of the problems addressed in this thesis two simple models of mixing (laminar mixing and turbulent mixing) are presented. These simple ideas will also serve to introduce a review of work by other investigators in the section which follows. At this stage it is best to define "mixing". Mixing two fluids together can be divided into a stirring and a diffusion component. Stirring is when one fluid is advected within another: the two fluids are always distinct and there is always a boundary separating the two. At the interface, however, chemical species from one fluid diffuse into the other fluid and the fluid is neither of the original two; therefore, mixing is caused by both stirring and diffusion. Given enough time diffusion will operate and homogenize the fluids.

The first simple model is laminar mixing which occurs in steady flow with only a component of simple shear. An example of simple shear is given Figure 1.1 where there is a horizontal velocity and a gradient in only the vertical direction. The two points shown in Figure 1.1 at t_o (solid circles) will horizontally separate at a constant rate and for long times the distance between the two points will increase linearly. Now consider a passive, circular heterogeneity, in two dimensions, bound by a material line, ℓ (i.e. a line which always consists of the same fluid particles). Initially the line integral of ℓ is the circumference $\pi\theta_o$, where θ_o is the diameter. The material line increases at a rate proportional to the separation velocity of two fluid particles separated vertically, say by θ_o, and for long times

$$\frac{\partial \ell}{\partial t} \approx \dot{\varepsilon}_s \ell_o = \pi\theta_o\dot{\varepsilon}_s \qquad (1.1)$$

where $\dot{\varepsilon}_s$ is the shear strain rate. The rate at which the material line increases is constant. The solution to (1.1) is

$$\ell \approx \pi\theta_o(\dot{\varepsilon}_s t + 1) \qquad (1.2)$$

The area of the two-dimensional heterogeneity must remain constant, so an average width in the shortest dimension is

$$\langle\theta\rangle \approx \frac{\pi\,\theta_o^2}{\ell} = \frac{\theta_o}{(\dot{\varepsilon}_s t + 1)} \qquad (1.3)$$

such that for long times $\langle\theta\rangle/\theta_o \propto t^{-1}$. The time, τ_{lm}, for an anomaly to be stirred by laminar flow below a minimum width, θ_{min}, is

$$\tau_{lm} \approx \frac{\theta_o}{\dot{\varepsilon}_s\,\theta_{min}} \qquad (1.4)$$

The second model, turbulent mixing, [Batchelor, 1952] can also be simply developed. This mode of mixing is sometimes call "normal" mixing because it is the normal strains at stagnation points which produce the relevant mixing characteristics. Consider a flow with spatially homogeneous turbulence, such that a fluid particle experiences pure shear and that fluid particles will, in a statistical sense, be subject to the same flow properties over time. The total material line of the passive heterogeneity, ℓ, is divided up into small segments, $\delta\ell$, such that for each segment the homogeneous turbulence assumption holds. This assumption will hold, if at any instance, $\delta\ell$, is close to a stagnation point (Figure 1.1). At a point close to a stagnation point, the velocity toward (or away from) the stagnation point is proportional to the distance from the center of the stagnation point [cf. Batchelor, 1967]. Thus, for a small parcel of fluid close to a stagnation point, of size $\delta\ell$, the rate at which it stretches in one direction (and compresses in the other) is proportional to $\delta\ell$; as shown at the stagnation point in Figure 1.1, if the distance between the two points is $\delta\ell$, then $\delta\ell$ will increase as

$$\frac{\partial}{\partial t}\ \delta\ell = \langle\dot{\varepsilon}_n\rangle\delta\ell \tag{1.5}$$

where $\langle\dot{\varepsilon}_n\rangle$ is a spatial and time average of the normal strains. Turbulent mixing contrasts with laminar mixing, as shown in Figure 1.1, in that two points in laminar flow recede from each other at a constant rate, while in turbulent mixing, the rate of separation increases as the two points separate from each other.

The solution to (1.5) is

$$\delta\ell = \delta\ell_o\exp(\langle\dot{\varepsilon}_n\rangle\ t) \tag{1.6}$$

The material line is the integral over all elements defining its length and in the limit that the small segments can be made infinitesimally small, i.e. $\delta\ell = d\ell$,

$$\ell = \oint d\ell = \pi\theta_o\exp(\langle\dot{\varepsilon}_n\rangle t) \tag{1.7}$$

and the average width in the shortest dimension is

$$\langle\theta\rangle = \theta_o\exp(-\langle\dot{\varepsilon}_n\rangle t) \tag{1.8}$$

The time, τ_{tm}, to reduce the average width of the anomaly by turbulent mixing below a minimum width, $\langle\theta_{min}\rangle$, is

$$\tau_{tm} \approx \langle\dot{\varepsilon}_n\rangle^{-1}\ \ln\frac{\theta_o}{\langle\theta_{min}\rangle} \tag{1.9}$$

These two mixing models can be applied to the mantle by assuming appropriate strain rates. Assume for simplicity that

$$\dot{\varepsilon}_s \sim \langle\dot{\varepsilon}_n\rangle \sim \frac{U_p}{D/2} \tag{1.10}$$

where U_p is the plate velocity of convection and D is the depth. The two models of mixing are shown in Figure 1.2. The initial size of the heterogeneity, θ_o, is 10 km (~ the average thickness of oceanic crust), the curves w.m. are for whole-mantle convection, D = 3000 km, and the curves u.m. are for upper mantle convection, D = 700 km. The difference between the two mixing models is extreme; after 100 m.y., for example, the 10 km initial heterogeneity has been drawn out and has a thickness of 2 km in laminar mixing, but only 5 m in turbulent mixing.

Also displayed in Figure 1.2 is the time-space domain within which diffusion would homogenize chemical variations. This domain is approximately bound by

$$\theta \sim \sqrt{\kappa_{chem} t} \qquad (1.12)$$

where κ_{chem} is an upper limit on the chemical diffusivity, ~ 10^{-13} cm^2/s [Hofmann and Hart, 1978]. The intersection between a $<\theta>$ curve and the region bound by diffusion, approximately defines the time to mix (not just stir) the heterogeneity; after this mixing time has elapsed all chemical and isotopic variation would be erased and the fluid would be homogeneous. A 10 km sized heterogeneity will be mixed O(100 m.y.) for turbulent mixing and O(1 to 10 b.y) for laminar mixing. The enormous difference between these two cases indicates that the applicability of these two models to the mantle will have to be carefully explored. Since chemical diffusion operates on scales of meters or less over geological times, it will be ignored for the research presented here.

1.2 Previous Work Related to Convective Mixing

Some work has appeared on the subject of mixing by mantle convection; most appeared in the literature during the thesis work. There have been investigations of mixing in steady circulations (e.g. McKenzie [1979], Richter and Ribe [1979], and Olson et al. [1984a,b]) and in unsteady or time-dependent circulations (e.g. Richter et al. [1982], Richter [1984], and Hoffman and McKenzie [1985]). Three features of mixing have been investigated by theoretical geodynamicists: (i) the rate or time scale of stirring, (ii) the form an anomaly takes after being stirred, and (iii) the effective lateral dispersion of heterogeneities by convection.

The mixing by steady flows, probably, only provides an upper limit on the efficiency of mixing. The studies on mixing by steady flows are fairly general in terms of their applicability to scenarios of mantle flow. On the other hand, some of the convective circulations employed in unsteady mixing calculations assume an unconstrained secondary mode of convection. There have been no studies specifically concerned with the mixing by plate-scale mantle convection.

McKenzie [1979] investigated the deformation associated with finite fluid elements in steady convective circulations. He found that an initially circular element would deform into an elliptical shape. The degree of deformation varied considerably depending on where the element was located, with the largest amount of deformation occurring near the edge of the cell and virtually none through much of the core. Elements near the margin of the cell elongate such that the rate of elongation is approximately consistent with stirring by pure shear. The deformed element was characterized by the largest dimension/shortest dimension (= f). After one circulation, one turnover, $f \sim 10^3$ near the edge of the cell, while $f \sim 1$-2 near the center, much less than predicted by simple shear for an average strain rate. Using the largest mixing rate in the circulation, McKenzie [1979] concluded that the mantle would be well mixed on O(100 m.y.).

Richter and Ribe [1979] employed an analytic approximation to a steady convection cell in a square region and employed a distribution of tracers extending from the center of the cell to the wall (like a slice of pie) as well as a distribution with a vertical gradient in concentration through the box. In both cases the tracers formed spirals centered in the middle of the cell after a few turnovers and the spiral "arms" became thinner as time progressed. They concluded heterogeneities would be stretched out into long thin sheets. The cause of this behavior and that in McKenzie's [1979] model is well known as there is a radial gradient in angular velocity (smaller velocities, but more rapid rotation towards the center).

Olson et al. [1984a,b], using a combination of analytical and numerical techniques, studied the mixing (stirring plus diffusion) by a single, steady convection cell. In Olson et al. [1984a] the tracers were initially distributed uniformly on one half of the region and in Olson et al. [1984b] the tracers were in the form of a subducted slab on the margin of a cell. The analysis was much more general than the one by McKenzie [1979] because the relevant mixing times were averages for the whole box. Olson et al. observed three important features of the mixing by steady, cellular flow: (1) mixing is dominated by simple shear (laminar flow), (2) the process is a "cascade" phenomenon with individual spectral components of an anomaly being transferred from low to high frequencies, in other words an anomaly is stirred into ever finer streaks, and (3) the laminar mixing time, in the limit of no chemical diffusion, was found be well approximated by equation (1.5), as simply derived above. Moreover, at long times, or after an anomaly had been drawn out into very fine streaks, Olson et al. [1984b] found that normal strains eventually dominate over shear strains, as would be expected from equations (1.3) and (1.8), if $\dot{\varepsilon}_s >> <\dot{\varepsilon}_n>$. For a compositional anomaly of 5 km across, Olson et al. [1984a] calculated that the anomaly would be mixed in 2.3 b.y. for flow confined to the upper mantle, while it would mix in 10 b.y. for whole-mantle convection.

Mixing in time-dependent flows was investigated by Richter et al. [1982]. The tracers are initially distributed through a square (sides equal to the box depth) in the center of a 8x1 box. The entire box was heated uniformly throughout and cooled from above. With a Rayleigh number, i.e. ratio of buoyancy to viscous forces, of 1.4×10^6 and constant viscosity, the top thermal boundary layer is unstable and the cold blobs detached in a fairly random pattern; the boundary layer instability caused the flow to be unsteady. Tracer motion exhibited a diffusional pattern at long length scales (about as large as the box depth) as the tracers moved laterally away from the center. Richter et al. concluded that at plate scales, dispersal of heterogeneities can only be accomplished by unsteady flow. The initial size of the anomaly had a length scale equivalent to the circulation scale which was also the scale of unsteadiness.

Hoffman and McKenzie [1985] further investigated the mixing in the type of flows studied by Richter et al. [1982]. Hoffman and McKenzie [1985] followed the material line of a fluid initially defined as a unit square in the center of the 8x1 box. They corroborated the result of Richter et al. [1982] that tracer dispersion exhibited a diffusional character at large scales. Moreover, by following the material line of an initial parcel of fluid, they were able to track the total length of the material line (or surface area) as a function of time. Apparently, this length increased exponentially in time as predicted by equation 1.7 simply derived above, although the authors did not present the actual numerical results. The length-scale of the anomaly was equivalent to the scale of circulation and flow unsteadiness. Hoffman and McKenzie concluded that mantle convection would mix heterogeneities in a turbulent fashion and that oceanic crust would be mixed in less than a few hundred million years.

1.3 Outline of This Thesis

The primary question which will be addressed in this thesis is: what is the form or type of mixing associated with plate-scale mantle convection? This question is motivated in the next two chapters, where the relevant geophysical and geochemical observations are presented. In Chapter 4 the methods employed to study mixing in thermal convection are systematically presented. The results of the mixing calculations are then given: mixing of purely passive material (Chapter 5), mixing in a medium with a depth-dependent viscosity (Chapter 6), and mixing of material with intrinsic density (Chapter 7). Throughout these three chapters every effort was made to present the fluid dynamical results in terms of non-dimensional quantities. The mixing times are then scaled to the mantle in Chapters 8-10, where the earth's thermal history is taken into account.

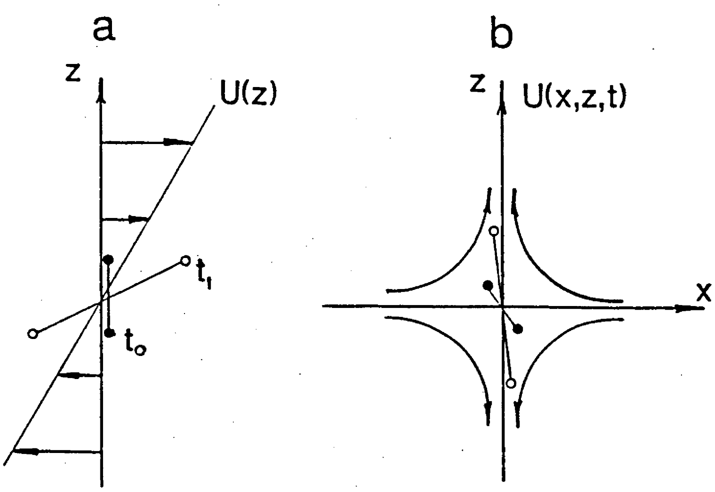

Fig. 1.1. Comparison of the generalized flow patterns which give rise to (a) laminar mixing (steady shear flow) and (b) turbulent mixing (unsteady flow). The deformation of a one dimensional element, defined by two end points, is compared in the two flows: the solid circles are for the initial position and the open circles are for a short time latter.

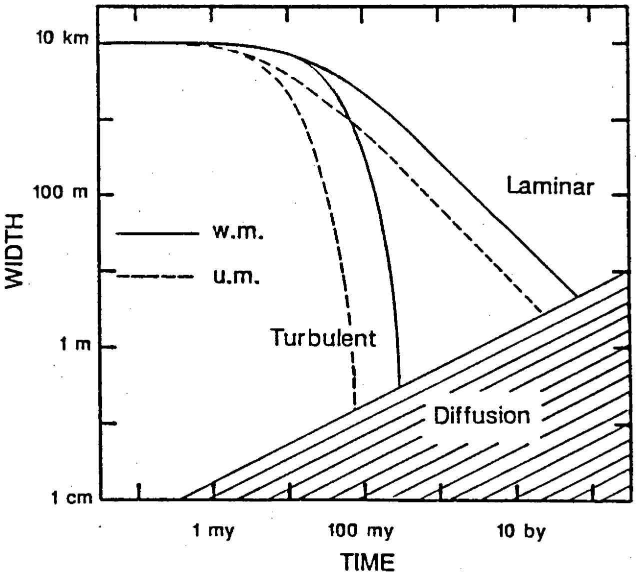

Fig. 1.2. Comparison of simple turbulent and laminar mixing laws for whole (w.m.) and upper mantle (u.m.) convection. The initial size of the heterogeneity is 10 km (~ dimension of subducted crust). The cross hatched area is the space-time domain where chemical diffusion would be important. The two simple mixing models predict very different mixing times. If mixing is dominated by laminar flow, then chemical heterogeneities can survive for the age of the earth.

CHAPTER 2

OBSERVATIONS WHICH PLACE PHYSICAL CONSTRAINTS ON CONVECTIVE MIXING

As will be seen later, the length-scale of a flow, its velocity, and its degree of unsteadiness control the rate at which it mixes a chemical heterogeneity. Furthermore, the viscosity structure of the ambient fluid and the intrinsic buoyancy of the chemical heterogeneity also affect the mixing rate. In this chapter observations which constrain the corresponding mantle quantities are summarized.

2.1 Plate-Scale and Other Modes of Mantle Convection

A chemical heterogeneity will be mixed by any mode of flow which occurs in the earth's interior. Mixing calculations can be constrained if the length and velocity scales of modes of mantle convection can be observationally constrained. We will see that only one mode (namely plate-scale flow) can be well constrained. It will be shown that the motion and cooling of the oceanic lithosphere is a dominant (if not the dominant) mode of mantle convection and that the horizontal velocities of the lithosphere are probably typical of mantle flow velocities. There are probably other modes of convection within the mantle (of smaller scale), one of which is partly constrained, hot-spot "plumes", while others are merely conjectural. This is not to say that some observationally undetected mode could not be important: some modes of convection may efficiently mix heterogeneities, while only weakly shaping geophysical signatures at the surface.

The motion of the lithosphere is known to be an important mode of mantle convection because it accounts for most of the heat loss out of the earth. Davies [1980a] and O'Connell and Hager [1980] have shown that the formation and cooling of the oceanic lithosphere accounts for about 70 % of the total terrestrial heat loss. Since a large fraction of the remaining heat is generated by radioactive decay in the crust and transported out by conduction, very little heat remains for some other mode of convection to transport; this seems to rule out any other significant large-scale mode of convection.

The heat flow argument indicates that the motion and cooling of the lithosphere is a dominant mode of convection, but it does not necessarily indicate that the motion of the lithosphere is coupled to the deeper interior. In other words, is the lithosphere a surficial process confined to the outer ~100 km of the earth and "decoupled" from the deeper interior? It is a common misconception among earth scientists that the lithosphere can "glide" over the low viscosity zone under plates. However, it is now well established that such a low viscosity channel would have to be 10^3 to 10^4 times less viscous for the lithosphere to be decoupled from the deeper mantle [Davies, 1977; Hager and O'Connell, 1979], whereas, the viscosity of the ~ 100 km thick, low viscosity zone is only between 10 and 100 times lower than the deeper viscosity [Cathles, 1975]. Schubert and Turcotte [1972], moreover, have argued, that counterflow of plates, confined to a thin channel, produces unreasonably large topographic variations. The return flow associated with plates, therefore, must extent deeper than just a few hundred kilometers into the earth and the lithosphere must be an integral part of a large-scale and deeply extending mode of mantle convection; independent observations further constrain the depth, see below. However, coupling does not demand that all deeper flow resemble the motion of plates, e.g. there could be downwellings and upwellings in the mantle not simply related to subduction zones and trenches, respectively.

If the motion of the lithosphere is the result of thermal convection, the average velocity of plates and the transported heat must be internally consistent. In other words, for a Rayleigh number estimated from the heat flux, the inferred velocity must be comparable with observed plate velocities. It has been established that plate velocities and heat flux are within predicted values by a factor of three (see, for example, Turcotte and Oxburgh [1967] or Turcotte and Schubert [1982]). Moreover, Hager and O'Connell [1981] have shown, in a global model, that the buoyancy associated with the observed thickening of oceanic lithosphere can easily account for observed plate motions.

Therefore, the plate velocities observed on the earth's surface, on average ≈ 5 cm/yr, provide a first order constraint on what the convective velocity is through the upper mantle.

Thus, there is little doubt that the oceanic lithosphere is a dominant mode of convection within the earth. However, are there other modes of convection within the earth? The possibility of larger than plate-scale modes has already been touched on. A mode of larger than plate-scale convection must have a smaller velocity than plates, since there is no significant, unaccounted, terrestrial heat flux. Therefore, since mixing is controlled by the strain rate ($\propto$ velocity/length scale), a larger scale mode must have a smaller strain rate. Larger scales of convection must be of less importance than plate-scale convection in mixing heterogeneities.

On the other hand, smaller than plate-scale modes of convection could be, locally, associated with high convection velocities without necessarily contributing to a significant heat flux. In fact, theoretically, we expect small-scale convection to exist in the mantle because it has such a high Rayleigh number (up to $\sim 10^9$). One often discussed scenario is the instability of an internal thermal boundary layer, perhaps like the core mantle boundary, which could give rise to small scale ($\sim$ 100 km sized) thermals. Such phenomena are observed in numerical calculations of thermal convection at a Rayleigh number of $\sim 10^9$ in a constant viscosity fluid [Jarvis, 1984]. Unfortunately, it is unlikely these small-scale modes of convection could be unambiguously detected with geophysical observations. Small-scale modes cannot extend to the surface because of the high viscosity of the lithosphere. Moreover, a large fractions of small thermals would unlikely be able traverse the entire mantle [Griffiths, 1986] and be detected, but they could well stir the lower mantle.

One small-scale mode of convection which is observed, is the so-called hot-spot plume mode which causes hot-spot swells, which are the 1000 km wide topographic, geoid and heat flow anomalies in the oceanic lithosphere [Crough, 1983]. A simple explanation of hot-spot swells is the existence of axisymmetric buoyant elements under the lithosphere [Olson and Nam, 1986]. The plume style of convection, however, probably only accounts for a small heat and mass flux within the mantle compared to plate-scale flow [e.g. Davies, 1980a]. The axisymmetric form of this convection means that strain rates fall off as $(\text{radial distance})^{-2}$ and therefore stirring is closely confined around plumes. Since there are only a small number of hot-spot plumes, a few dozen, it seems unlikely this could be an effective stirring mechanism of chemical heterogeneities. This assumption should be tested; it is, however, beyond the scope of the present work.

In addition to the plume mode of convection, a number of investigators have speculated, within the context of upper mantle convection, that there is a mode of flow perpendicular to plate motion [McKenzie and Weiss, 1974; Richter, 1978; McKenzie et al., 1980]. This hypothesis has been motivated by observations which seem to indicate that the lithosphere is a "plate" whose base is maintained at a constant temperature, as opposed to being a thermal boundary layer on a half space. Parsons and Sclater [1977], and earlier authors, showed that oceanic bathymetry flattens after 80 Ma; they argued that this supports the plate model and requires the existence some kind of small scale convection which maintains the "base" of the lithosphere at a constant temperature. However, O'Connell and Hager [1980] have argued that small scale convection would do just the opposite: cause bathymetry to deepen not shallow out. In any case, a mode of convection other than "hot-spot plumes" may not be required to explain the bathymetry: Heestand and Crough [1981] and Schroeder [1984] have shown that there is a clear correlation between how close a segment of the ocean floor passes a hot-spot and the height of its anomalous bathymetry. Further confusion comes from the work of Cazenave [1984], who showed that the geoid offset across fracture zones are not explained well by either the plate or the half space model. In light of these conflicting observations and models, this mode of small-scale convection, perpendicular to plate motion, is judged conjectural at best and must be ignored for this first study on the mixing by plate-scale flow.

The dominant mode of convection within the mantle is plate-scale flow, which is well constrained, see following sections. Smaller than plate scale modes of convection could also mix heterogeneities, but they are at present either poorly constrained or conjectural. Therefore, the primary goal of this study is to better understand the effects of plate-scale flow on mixing; the neglect of secondary scales of flow is a justifiable place to start. Since other small-scale modes could exist, some of the results that are presented in this thesis regarding the mixing rates should be considered lower bounds on the true mixing rate within the mantle. More fundamentally, however, mixing by plate-scale flow must be understood because the major sources of chemical variation within the mantle (e.g. fractionation under ridges and subduction of altered lithosphere at trenches) are intimately connected with plate-scale flow.

2.2 Plate Kinematics and Flow Unsteadiness

As will be shown later, the unsteady nature of a flow could contribute significantly to the way the flow stirs a chemical heterogeneity; therefore is plate scale flow unsteady? A principal feature of plate kinematics is that active margins between lithospheric plates, i.e. ridges and trenches, migrate with respect to each other. Therefore deep mantle flow associated with lithospheric plates must be unsteady. Plate kinematics are the only presently available observation related to the large-scale unsteadiness of mantle flow.

To fully constrain the unsteady flow that might exist in the mantle, we would need a kinematic history of all oceanic and continental plates. The history of the Atlantic is known quite well because essentially no lithosphere has been lost by subduction since the ocean first formed; unfortunately this history is on the order of hundreds of millions of years and only about one transit time of the mantle. The situation is similar in the Indian ocean, although more complex. The history of the Pacific is uncertain because it is presently surrounded by subduction zones and has possibly been in such a situation for hundreds of millions of years [Hilde _et al._, 1977]. Much of the Pacific basin tectonic history, originally recorded on the ocean floor, has been lost by subduction. As we try to reconstruct combined oceanic and continental histories, the constraints become sparse as we move further back in time. Except for one "snap-shot" in the early Tertiary [Jurdy, 1978], there are no global histories of combined oceanic and continental history, even for a short period back in time.

A brief overview is given of the general features of plate tectonics which are used to constrain the convective mixing models (shown schematically in Figure 2.1). The steady-state situation of Fig. 2.1a illustrates two well know features of plates, velocity is uniform over the extent of plates and ridges spread symmetrically. Conversely, converging margins have asymmetrical flow (Figure 2.1a). There are no present geological analogues of the steady-state shown. Figure 2.1b illustrates how symmetrical spreading can be maintained with a migrating ridge. The ridge moves to the left with a non-dimensional velocity of -1/3 while the outward velocity from the ridge of the right and left plates are each 2/3 with respect to the ridge; in a frame relative to the adjacent third plate, the plate to the left is moving three times as fast as the plate to the right. One of the better examples of ridge migration is the migration of the south Atlantic ridge westward from the Carlsberg ridge in the Indian Ocean. In the example shown in Figure 2.1b, the ridge migrates into a trench; the best known example of this is the ridge which migrated through the Gulf of Alaska and subducted beneath Alaska and British Columbia, leaving the magnetic anomalies of the northeast Pacific behind. The last example in Figure 2.1c shows the tendency for the overriding plate to migrate oceanward. This feature is most easily seen in the plate velocity vectors in the hot-spot reference frame shown in Figure 2.2 (from Chase [1978]). The velocities for the overriding plates generally point seaward. The overriding plate in Fig. 2.1c has the same velocity as its margin. It must be emphasized that there is a fundamental ambiguity in that the cases shown in Figure 2.1 b and c are, in fact, indistinguishable observationally.

The features just summarized, Figure 2.1, occur over time scales on the order of 100 m.y. and are well documented; however, there is considerable uncertainty in what happens after two margins coalesce. We do not know what the long term arrangements of these basic rules are. Many of the large-scale features of unsteady plate kinematics remain elusive. Consequently, although the short term (less than 100 m.y.) boundary conditions of convection models can be well constrained and are easily introduced into the calculations, longer term features are uncertain. This uncertainty will require the use of a range in long-term plate models, see Chapter 4.

2.3 The Viscosity Structure of the Mantle

The surface velocity of mantle convection is directly constrained, but the variation of velocity through the interior is affected by variations in viscosity. The models to be presented, bounded by surface velocity, are not sensitive to the absolute viscosity, but are sensitive to spatial variations in viscosity. An increase in viscosity with depth, for example, will cause velocities and strain rates to be reduced at depth [Davies, 1984].

For mixing by convection, we must know the viscosity at deep levels within the mantle and this can be constrained through global models of the response of the earth to glacial ice loads which occur $O(10^4$ yr) [O'Connell, 1971; Cathles, 1975; Peltier, 1983]. In these models the mantle is assumed, out of computational simplicity, to effectively have a Newtonian viscosity. With such models, deformations during loading and unloading are calculated at various surface points and compared to observed values. In general, the conclusion drawn from such studies is that the effective viscosity is constant through the upper and lower mantle and with an absolute value of about 10^{21} Pa s [O'Connell, 1971; Cathles, 1975; Peltier, 1983]. However, as emphasized by Nakada and Lambeck [1986] the depth resolving power of such models may not be very great and a range of models other than the constant 10^{21} Pa s model may be consistent with the given constraints.

Recently, however, Hager [1984] has introduced an independent technique which constrains the depth-dependence of effective viscosity. Density heterogeneities within a viscous mantle deform the boundaries of the mantle (e.g. the surface and the core mantle boundary) such that the geoid is a function of both the density of the heterogeneity as well as the deformed boundaries; because the amount of boundary deformation depends upon spatial variations in viscosity, so too is the geoid a sensitive function of viscosity. Hager [1984] concludes that the viscosity of the lower mantle must be 30 times higher than the upper mantle in order to explain the observed geoid highs over subducted slabs. If the viscosity is greater at depth, then the deformation of the earth's surface is reduced and the positive anomaly of the cold, dense slab dominates the geoid signal.

O'Connell and Hager [1984] place further independent bounds on the viscosity of the lower mantle by using the observed long wavelength seismic velocity variations through the lower mantle. A coupled momentum/heat equation is solved such that flow velocities are driven by density variations constrained by seismic velocity. Temperatures are proportional to such density variations and are advected by the flow. In order that the heat flux advected out of the lower mantle be less than the observed flux out of the mantle, the viscosity must be $\geq 10^{22}$ Pa s, which is consistent with an increase in viscosity with depth through the mantle.

2.4 Upper Mantle vs. Whole-Mantle: What is the Depth of Convection?

The depth of convection strongly controls the shear strain rate and hence mixing as shown in Chapter 1. The purpose of this section is to give an overview of observations which constrain the depth of convection associated with the horizontal motions of the earth's surface. There have been two prevailing views on the depth of mantle flow: flow confined above 670 km and flow extending throughout the whole mantle. A number of strong observational arguments have emerged which argue against layered convection. However, when this thesis research was first undertaken, the depth of convection was more of an open question. Here, the major observational arguments for both models are systematically presented. Both models will be considered as working hypotheses for this thesis, although it is argued that whole-mantle convection is to be preferred. This change in perspective came about after it was realized that the observations which apparently demanded upper mantle convection were shown to be inherently weak in that they were also consistent with whole-mantle convection [Davies, 1977; O'Connell, 1977].

2.4.1 Upper-Mantle Convection.

Two features of slab seismicity are the main arguments used in favor of upper mantle convection: the global cut-off in seismicity at 670 km and the transition from down-dip tension to down-dip compression in slabs as they approach 670 km. The deepest locations of earthquakes in slabs almost invariably are ≈ 670 km. The argument in the past has been, no seismicity, no penetration into the lower mantle [McKenzie and Weiss, 1975; McKenzie and Richter, 1981]. Moreover, the focal mechanisms of earthquakes in slabs with seismicity extending down to 670 km have down-dip compression, while those with seismicity extending only half way through the upper mantle have down-dip tension [Isacks and Molnar, 1971]. This suggest that slabs may be pulled down through the center of the upper mantle, but as they approach 670 km they meet increased resistance and cannot penetrate into the lower mantle [McKenzie and Weiss, 1975].

These observations have also been shown to be compatible with whole-mantle convection. The cut-off in seismicity does not demand flow confined to the upper mantle. The data can just as easily be explained in terms of whole-mantle flow: after the slab passes through the 670 km discontinuity the material can no longer undergo brittle failure. Presumably, the mantle minerals are more densely packed after passage through the phase transition and either the mechanism causing earthquakes may no longer be able to occur or stress is relieved during transition. This poses the question as to why, in the upper mantle convection hypothesis, seismicity ceases after the slab bends horizontally along the 670 km boundary. All slabs are not all at the same temperature when they reach 670 km and they have not thermally equilibrated. These arguments demonstrate that the cut off in seismicity does not demand confinement of flow to the upper mantle: the observations can easily be explained in terms of whole-mantle flow.

The transition from down dip tension to compression can also be satisfied by slab penetration into the lower mantle if there is a jump in viscosity across the 670 km discontinuity [Vassiliou et al., 1984]. The study of Vassiliou et al. [1984] corroborates the original hypothesis that stress patterns require increased resistance to slab penetration [Isacks and Molnar, 1971]. However, the level of resistance actually required to satisfy the stress pattern seems to have been vastly overestimated and an order of magnitude increase in viscosity can easily match the stress patterns.

Some geochemical observations were thought to demand layered convection. In particular, it was thought that part of the mantle was "primitive" and mass balance calculations indicated that 1/3 to 1/2 of the mantle was depleted [O'Nions et al., 1979; DePaolo, 1980] with the rest assumed primitive. The depleted part was associated with the upper mantle, which is about 1/3 of the mantle by volume. Moreover, there is a mantle flux of ^{3}He, "primitive helium", and it was presumed that if there was whole-mantle convection all the ^{3}He would be lost by now; thus, it was thought, this required layered mantle convection [Allègre et al., 1983; O'Nions and Oxburgh, 1983].

The geochemical arguments are weak. The mass balance calculations are based on the premise that part of the mantle is geochemically primitive. There is no compelling evidence from geochemistry to support this contention [Zindler and Hart, 1986]; the source for the Hawaiian hot-spot may approach a primitive reservoir [White, 1985], but the data do not demand that it is primitive. Moreover, assuming there is a primitive reservoir, the mass balance calculations can give primitive/depleted reservoirs anywhere between 0.1/0.9 to 0.9/0.1 [Goldstein et al., 1982; Davies, 1984; Zindler and Hart, 1986]. In other words, almost any mass fraction of depleted versus primitive is permissible by current constraints.

2.4.2 Depth of Convection: Strong Arguments.

There have in the last few years emerged a series of observations, which seem incompatible with flow layered above 670 km. These arguments include: the shapes and dips of Benioff zones, the "imaging" of seismic velocity in the vicinity of slabs, and the correlation of the geoid with various surface fields.

The locations of earthquakes in slabs trace the path slabs take as it moves through the mantle. There is a clear and consistent pattern to Benioff zone shapes: there is a positive dip throughout and they do not flatten out or turn backwards under the subducting plates, Figure 2.3. Hager and O'Connell [1979] have shown that if observed velocities of plates are imposed onto a model mantle with flow confined above 670 km that the dips of flow do not correlate with the dips of Benioff zones, but if flow is allowed to penetrate through the whole-mantle then there is a strong correlation between dips of flow and Benioff zones. Davies [1986b; manuscript in preparation] has shown that the Benioff zone shapes in numerical convection models scaled to the upper mantle show either a flattening out or a reversal as they approach 670 km; this phenomenon is observed in models through a large range of reasonable upper mantle parameters. No observed Benioff zones show this behavior. However, in models scaled to whole-mantle convection, the modeled Benioff zone shapes have the same pattern as observed (cf. Figure 2.3). This is a strong argument against upper mantle convection.

Seismic waves emerging from deep slab earthquakes (> 150 km depth) sample the velocity structure in the vicinity of slabs. Some seismic rays pass through the mantle under Benioff zones below 670 km. The slab, being colder, has a higher seismic velocity than ambient mantle and rays passing through the slab should arrive sooner at the receiver than predicted. Jordan [1977] and Creager and Jordan [1984,1986] have shown that the seismic waves from slab earthquakes which pass along slabs and into the lower mantle consistently arrive sooner relative to standard travel times than those rays which pass perpendicularly out of slabs. Extensive ray tracing through 3-D slab models derived from thermal modeling indicates that the slabs must penetrate at least to 1000 km, well below the 670 km seismic discontinuity.

A further constraint on the depth of mantle flow comes from the study of geoid highs over subducting slabs (Hager [1984], as discussed in section 2.3). The geoid highs can be modeled in two ways: whole mantle flow with a depth-dependent viscosity or flow confined to the upper mantle. The upper mantle model, however, requires the slabs to be five times more dense than predicted from conductive warming models. Since the density contrast of slabs is well constrained, such a large excess density contrast seems implausible and thus geoid highs over slabs are most consistent with whole-mantle convection.

There is a wide variety of geophysical observations which constrain the depth of convection. Some of these observations are consistent with both upper mantle and whole-mantle convection. A number of observations seem inconsistent with a simply layered mantle. However, because these observations have only been clarified recently, both styles of convection were considered working hypotheses during the course of the research.

2.5 Slow Moving Hot-Spot Sources and Ancient Plate Boundaries

Some indirect observations, especially the slow motion of hot-spots with respect to each other, strongly suggest that the deep mantle may convect rather sluggishly with respect to plate motions. If so, then convection velocities and strain rates deduced directly from observed plate velocities and the depth of convection may significantly over-estimate average mantle strain rates. Such observations are consistent with more direct observations related to the depth-dependence of the mantle viscosity (section 2.3).

Individual plates move with respect to individual hot-spots and this indicates that the plate moves with respect to the source of the individual hot-spot. Hot-spots taken as a single population, however, move slowly with respect to each other and this strongly indicates that hot-spot sources reside within a rather sluggish deep mantle. The conventional hypothesis is that the source of hot-spots is located on the core-mantle boundary (CMB) [Morgan, 1971], and requires that the actual position of plume instability on the boundary layer be spatially persistent. Although it is not fluid dynamically impossible for a diapir or plume source to remain stationary at some position on a thermal boundary layer in an isoviscous fluid, it does require special pleading. In any event, postulating the deep mantle behaves rather sluggishly is a much simpler hypothesis because it does not require the hot-spot source to be a stationary boundary layer instability; large blobs, entrained in flow, could produce slow sources as well [Davies, 1984]. Blob sources within an isoviscous mantle would be expected to produce hot-spots which rapidly migrate with respect to each other.

Other geological/geophysical observations support the hypothesis that the deep mantle convects more slowly than oceanic lithosphere: in particular, the observation that ancient plate boundaries correlate with the long wavelength geoid [Chase and Sprowl, 1983]. Geoid lows correlate with the zones of subduction which existed 125 m.y. ago; these ancient subduction zones were spatially persistent for at least 100 m.y. and probably for even longer. Chase and Sprowl [1983] argue that this indicates that the lower mantle lags at least 100 m.y. behind the lithospheric plates.

2.6 Intrinsic Buoyancy of Subducting Lithosphere

The final important parameter controlling mixing is the intrinsic density difference between the two fluids mixing together and in this case the density difference is between the oceanic crust (or the oceanic lithosphere) and average mantle. Constraints on this parameter come from experimental petrology.

The subducting lithosphere is not a simple sheet of fluid with uniform compositional buoyancy, but rather has a layered structure [Ringwood, 1975; 1982]. Such a stratification forms because when basaltic oceanic crust is created by ridge magmatism, it depletes the top part of the mantle and gives rise to residual (or depleted) harzburgite and lhertzolite layers. Extensive laboratory work on basalts at high pressure indicates that the crustal part is more dense by about 200 kg/m^3 to at least 900 km depth within the mantle compared to average pyrolite [Ringwood, 1982]. On the other hand, the depleted layers are less dense, on average; because of the many minerals which make up the rock layers, phase transitions occur at different depths and temperatures, such that the distribution of buoyancy with depth is fairly complex and many of the details are still being worked out. However, an upper bound can be placed onto the "chemical" lithosphere as a whole; the chemical lithosphere includes the oceanic crust and the residual harzburgite layers, which have a total depth of about 30 km [Ringwood, 1982]. Integrating the density across the entire chemical lithosphere from the data summarized by Ringwood [1982], it is unlikely the lithosphere could have a density differences greater than about 10 kg/m^3. This estimate, however, must be considered preliminary.

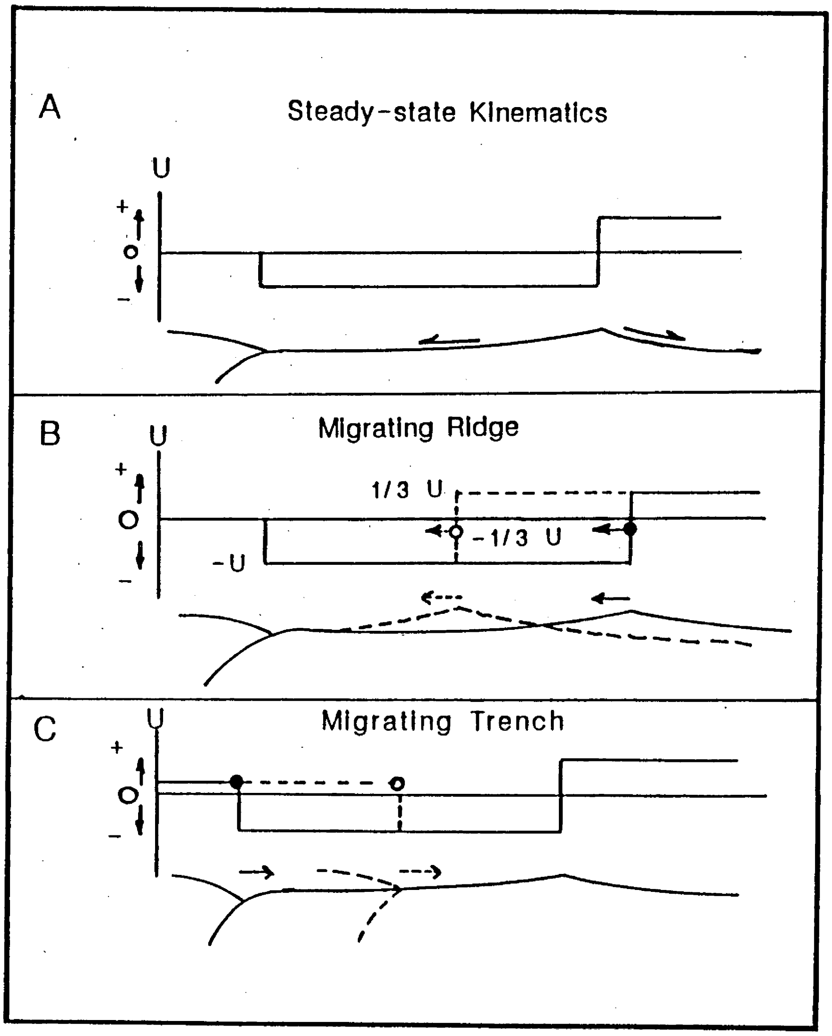

Fig. 2.1. Schematic of the general rules of plate kinematics. For each case the plate tectonic analogue is shown below the velocity boundary condition. Show are: (a) steady-state plate kinematics, (b) a ridge migrating toward a stationary trench on the left, (c) a trench migrating toward a stationary ridge on the right.

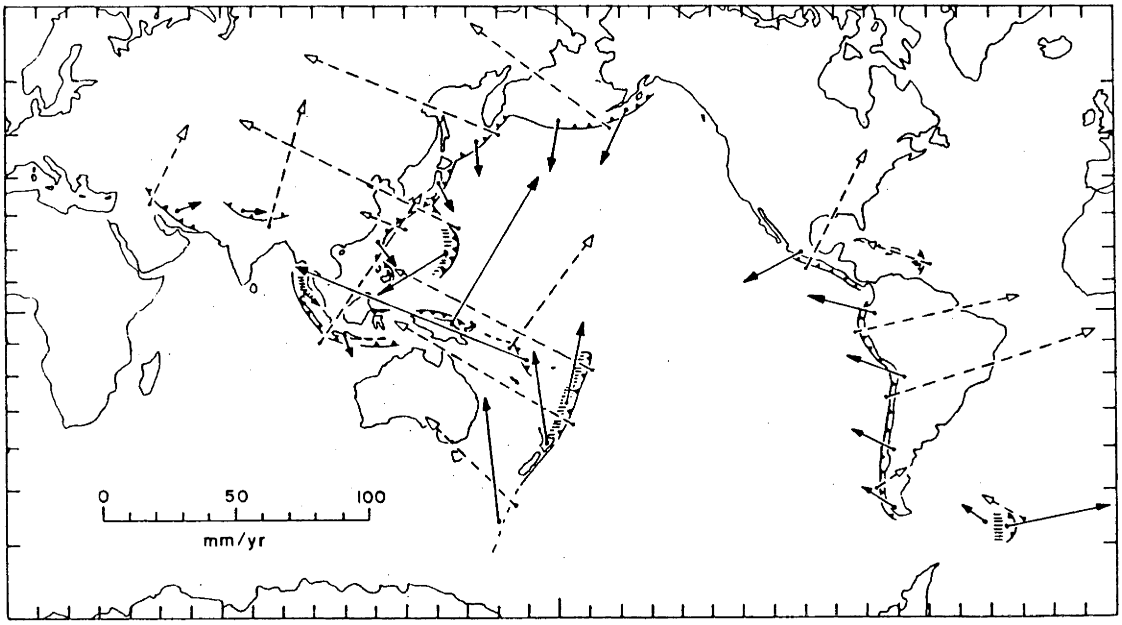

Fig. 2.2. Motion of various points in the mean hot-spot reference frame. The significant feature is the motion of the plates overlying subduction zones (solid arrows) which move "oceanward" (from Chase [1978]).

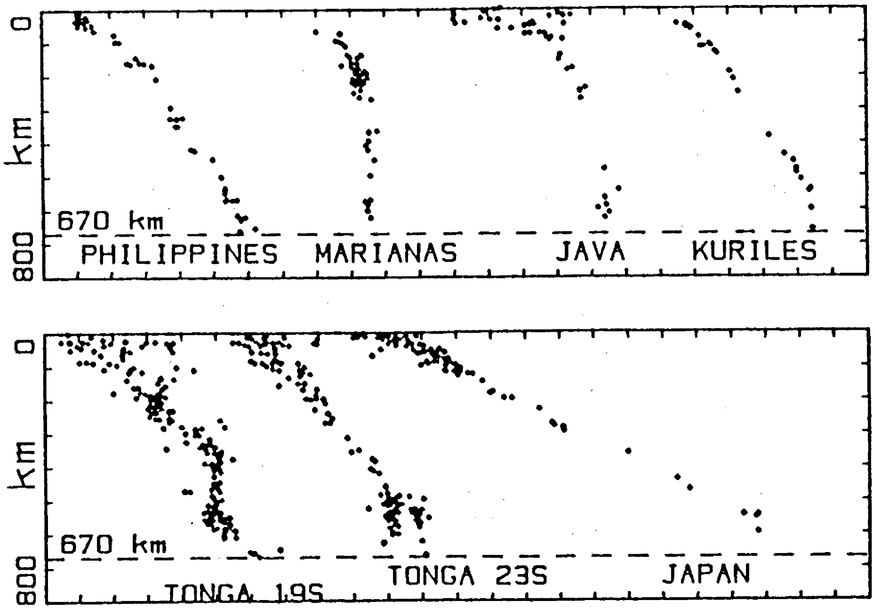

Fig. 2.3. Earthquake hypocenters defining Benioff subduction zones. The benioff zones never bend away from the cut off point in seismicity (670 km) as would be expected if flow were confined above 670 km. The shapes of Benioff zones are only explicable in terms of flow extending deeper than 670 km (from G. F. Davies, manuscript in preparation).

CHAPTER 3

ISOTOPIC AND OTHER GEOLOGICAL/GEOCHEMICAL CONSTRAINTS ON CONVECTIVE MIXING

The geochemical observations motivating the mixing calculations are reviewed here. There are three principal observations which give important insight into mantle processes: (1) the mantle is isotopically heterogeneous, (2) the heterogeneities have existed, on average, for 1 to 2 b.y., and (3) the heterogeneities exist over length-scales from hundreds of meters to ~ 10^4 km. These follow mainly from the study of Sr, Nd, and Pb isotopes in mid-ocean ridge basalts (MORB's) and oceanic island basalts (OIB's). Rare gas systematics supplement the Sr, Nd, and Pb isotopes in deducing the origin of mantle heterogeneities and they are also briefly reviewed. Since the only directly observed source of chemical variation is the subduction of chemically anomalous oceanic lithosphere it is of principal interest in this thesis; a number of diverse observations constrain the chemistry of subducted altered lithosphere and these are described.

3.1 General Isotopic Systematics of Sr, Nd, and Pb

Studies of oceanic basalts have revealed that the sources for oceanic volcanism must be isotopically heterogeneous. Analysis of oceanic basalts have revealed that there are significant variations in $^{87}Sr/^{86}Sr$, $^{143}Nd/^{144}Nd$, and $^{206}Pb/^{204}Pb$. Since there is no expectation of heavy isotope fractionation during the formation of MORB and OIB, the source within the mantle must have these isotope variations.

Moreover, simple correlations are not found between these three isotope systems. For example, oceanic basalts do not have a simple linear correlation between the $^{87}Sr/^{86}Sr$ versus $^{143}Nd/^{144}Nd$ ratios (Figure 3.1 b), as was originally thought [DePaolo and Wasserburg, 1976]. Some island fields (such as Samoa and St. Helena) fall off the mantle array, and some islands have $^{143}Nd/^{144}Nd$ ratios less than "primitive," for example, Kerguelen [White and Hofmann, 1982]. This means that the mantle is more heterogeneous than accounted for by the mixing between two components and that at least one component must be more enriched than primitive [White and Hofmann, 1982]. A much more extreme case is found for the $^{87}Sr/^{86}Sr$ versus $^{206}Pb/^{204}Pb$ ratios (Figure 3.1a), which show extreme scatter [Sun, 1980; Sun and Hanson, 1975], and this indicates that the observed isotope ratios cannot be explained by simple mixing of two components.

Since the work of Hofmann and White [1982], considerable effort has gone into discerning the minimum number and nature of isotopic components. White [1985] argues that at least five distinct basalt groups are recognised in terms of their Sr, Nd, and Pb isotopic signatures. Zindler and Hart [1986] using even a larger data set argue that all of the variation can be explained by variable amounts of mixing between four components. The data are also consistent with a much greater number of sources.

3.2 The Age of Mantle Heterogeneities

A time scale is also indicated by the spread in isotope ratios. The linear correlations of the Pb ratios for OIB's and MORB on the $^{207}Pb/^{204}Pb$ versus $^{206}Pb/^{204}Pb$ diagram (Figure 3.1 c) and on the $^{208}Pb/^{204}Pb$ versus $^{206}Pb/^{204}Pb$ diagram can be interpreted as if they were isochrons with an average age of about 1.8 b.y. [Church and Tatsumoto, 1975; Tatsumoto, 1978; Chase, 1981].

This apparent Pb-age is corroborated by Rb-Sr isotope systematics which implies an age of about 1.6 b.y. [Sun and Hanson, 1975; Brooks et al., 1976; Duncan and Compston, 1976]. Brooks et al. [1976] assembled Rb-Sr data and plotted Rb/Sr versus $^{87}Sr/^{86}Sr$ and found a strong correlation for oceanic island tholeiites and island and MOR tholeiites and interpreted the slopes as isochrons, with ages 1.4 and 1.6 b.y., respectively. Duncan and Compston [1976] determined the Rb-Sr isotopic systematics for basalts from 15 islands from French Polynesia and found a very strong correlation between $^{87}Rb/^{86}Sr$

versus $^{87}Sr/^{86}Sr$ on an isochron diagram (Figure 3.2). The implied age is 1.4 b.y. The correspondence between the Rb-Sr and Pb-Pb ages suggests that isotopic reservoirs (however many there are) have persisted, on average, for 1 to 2 b.y. [Sun and Hanson, 1975].

Moreover, when two-stage Pb-models are calculated for oceanic islands individually (see Figure 3.3), the same primary parent to daughter ratio results [Chase, 1981], and this implies that the source region for all the islands may have been the same. Because the island arrays intersect tightly in the MORB field (see Figure 3.3), Chase [1981] proposed that ancient subducted MORB was the primary OIB source. This involvement of ancient MORB as the source for present-day OIB is consistent with crustal recycling. Moreover, the "ages" for the individual island sources vary from 1 to 2.5 b.y.

3.3 Rare Gas Systematics

Rare gases, in particular the isotopic systemtics of He and Xe, are complementary to those of Sr, Nd, and Pb, principally because these gases are partially lost (degassed) from the solid earth during the formation of basalts; Sr, Nd, and Pb, on the other hand, can be recycled back into the earth.

There are two isotopes of helium, ^3He and ^4He. ^3He is not a radioactive daughter, execpt for a small amount involving a nuclear reaction with Li, and is often called "primordial" because none has been added to the solid earth since accretion. ^4He is the α decay product of U and Th. $^3He/^4He$ values quoted here, are normalized by the atmospheric value [Lupton, 1983]. $^3He/^4He$ from mantle-derived basalts presently range from about 1 to 32 times atmospheric.

In general, the lowest values are for MORB and the highest values for Hawaii and Iceland (Figure 3.4). The isotopic ratio $^3He/^4He$ in basalts from some hot-spots (most notably from the Hawaiian seamount Loihi) have values three to four times higher than the values for mid-ocean ridge basalts [Kurz et al., 1983]. These observations imply parts of the mantle are less degassed than other parts and have been interpreted in terms of a primitive, undegassed lower mantle which convects separately from the upper mantle [Allègre et al., 1983; O'Nions and Oxburgh, 1983]. Conventional thinking suggests that if whole-mantle convection occurs the entire mantle would be degassed by now and little or no ^{3}He would be presently emerging from the mantle [Allègre et al., 1983], contrary to what is observed.

The helium isotope systematics are fundamentally ambiguous because they do not directly constrain how much helium was incorporated into the primitive earth. It is possible that true primitive mantle could have values much larger than 30 times atmospheric (the largest values observed for terrestrial rocks); primordial estimates range from 100 to 200 times atmospheric [Lupton and Craig, 1978]. In other words, the source(s) of Loihi or Iceland, although often call "primitive" [e.g. Allègre et al.,1983], could have been degassed under ridges at some earlier epoch. In any case, the helium systematics do indicate that parts of the mantle have been degassed less than other parts.

The survival of ancient segments of the mantle is supported by differences in the ^{129}Xe/^{130}Xe ratio between MORB and OIB [Allègre et al., 1983]. ^{129}Xe is the decay product of the extinct nuclide ^{129}I which has a half life of about 16 m.y.; this means that any difference in the ^{129}Xe/^{130}Xe ratio must have been produced between distinct reservoirs in the first ~ 50 m.y. of the earth. The detection of such ratios today implies that the those reservoirs must have remain distinct (have not been mixed together) for the last ~ 4.4 b.y. The ^{129}Xe/^{130}Xe differences have yet to be corroborated.

Moreover, helium isotopes have also provided important corroborating evidence for recycling. Mantle rocks cycled through the oceanic crust (subjected to magmatic fractionation at ridges) lose helium by degassing. Segments of the mantle previously recycled should be strongly depleted in primitive He, and hence have low ^{3}He/^{4}He ratios, because of the production of radiogenic ^{4}He. The islands of Tahiti, Tristan da Cunha, and Gough have as high or higher ^{87}Sr/^{86}Sr ratios compared with Hawaii, but significantly smaller ^{3}He/^{4}He ratios than MORB. An interpretation of these isotope systematics is that not only has there been preferential degassing but there has also been time integrated enrichment of Rb compared with Sr in the sources of some islands (like Tahiti, Tristan da Cunha, and Gough). A simple and a plausible actualistic hypothesis is that the sources for some oceanic islands have been cycled through the oceanic crust [Kurz et al., 1982].

3.4 The Size-Spectrum of Heterogeneities

The question arises as to whether the isotopic heterogeneities exist over one length scale, over all scales, or does isotopic variation increase with length-scale? In other words, what is the size-spectrum ? Unfortunately the size-spectrum cannot be measured directly, but it can be indirectly constrained (bounded) by isotopic ratios of basalts produced through magmatism [cf. Zindler and Hart, 1986]. In the past, geochemists have not tried to place bounds on this quantity, so that, as described in Gurnis [1986], constaints on size-spectrum were assembled here from a literature search. The apparent size-spectrum is presented in Figure 3.5.

The size-spectrum of Figure 3.5 has been constrained by both the $^{87}Sr/^{86}Sr$ ratios in basalts sampled down axes of oceanic ridges and $^{87}Sr/^{86}Sr$ ratios in OIB's over various length scales. The $^{87}Sr/^{86}Sr$ ratio was chosen because it has been the most extensively measured radiogenic isotope in oceanic basalts; the data were gleaned from an extensive literature search. Moreover, the analysis has been confined entirely to oceanic (MORB and OIB) samples in order to ensure that the spectrum has not been subject to continental contamination.

When both ridge axes and island variations are taken together, the spectrum, Figure 3.5, shows that at any frequency there is a wide range in amplitudes. However, no frequency is preferred over any other -- there is no hint of a peak at any particular frequency nor is any positive or negative trend evident. Moreover, the maximum amplitude for the different sampled features (eg. single islands, island chains, oceans, and ridge axes) was found to be constant within a factor of 1.4 from 10 km to 1.5×10^4 km. This quantitatively substantiates that isotopic heterogeneity exists on all observable length-scales. More fundamentally, however, the spectrum cannot be distinguished from a flat or white-noise spectrum.

Hart [1984] has assembled Pb and Sr data over the entire globe and contoured Pb and Sr isotopic anomalies. An over-all pattern seems to emerge with a broad scale isotopic anomaly centered in the Indian and South Atlantic oceans. This large-scale feature presumably corresponds to the longest wavelength (10^3 and 10^4 km) components in the Sr size-spectrum (Figure 3.5).

There must be a lower size limit on the detection of isotopic heterogeneity within the mantle as sampled through magmatism. This lower limit is poorly known. However, there are rock bodies known as orogenic lherozlites which are presumably mantle material tectonically emplaced into the crust. A detailed Sr and Nd isotopic study by Reisberg and Zindler [1986] of the Ronda Ultramafic Complex in Spain reveals that over a distance of ~ 50 meters the amplitude in $^{87}Sr/^{86}Sr$ is half as large as the global maximum found above; presumably the mantle has such variations [Reisberg and Zindler, 1986]. Thus isotopic variations, of comparable magnitude exist over more than five orders of magnitude.

3.5 Further Evidence for Recycling in the Recent Geological Past

There is also a large base of data that demonstrates that sediments subduct in significant quantities. Sediments have been recognized in the tensional grabens in lithosphere about to subduct [Isacks et al., 1968], and sediment-filled grabens have been detected by seismic reflection under overriding plates [Hilde, 1983]. Geologic and mass balances deduced from recent DSDP/IPOD drilling in trenches requires that at least 50 % of sediments reaching trenches subduct [Von Huene et al., 1982; Hussong and Uyeda, 1982]. The detection of ^{10}Be anomalies in island arc volcanics (IAV's), but not in other volcanics, demonstrates the subduction of sediments [Brown et al., 1982].

The geological data do not prove sediments and oceanic crust subduct into the deep mantle because it is possible they are largely tapped off by IAV's. Sediment off-tapping has to exist, at least to a small extent, to explain the ^{10}Be anomalies. The sources of IAV can be constrained by using Sr, Nd, and Pb isotopes as tracers. Unfortunately, IAV's show increased amounts of continental contamination in more continental settings [White and Patchett, 1984]; therefore only those settings entirely oceanic can be used to test the incorporation of crust and sediments into IAV's by using isotopes as tracers.

A detailed study of the Pb isotope variations in Mariana arc andesites and oceanic sediments converging toward the trench is presented by Meijer [1976]. The data clearly demonstrate that the Mariana Frontal Arc and active arc lavas are isotopically indistinguishable from MORB. Because the sediments converging toward the Mariana trench have such high $^{207}Pb/^{204}Pb$ (and $^{208}Pb/^{204}Pb$) ratios compared with $^{206}Pb/^{204}Pb$ and because the concentration of Pb in the sediment is approximately 25 times the concentration in Mariana arc volcanics and oceanic basalts, even a small amount of sediment contaminating the IAV source would give Pb isotopic ratios significantly different from those observed. Meijer [1976] calculates that the sediment contribution to IAV cannot be greater than 1%. It follows, at least in the Marianas, that most sediment and crust is recycled into the deep mantle.

3.6 Conclusions

The data reviewed here indicate the existence of mantle heterogeneities that have persisted for billions of years. Since there are at least four components or reservoir "types" within the mantle, the isotopic variation does not seem to be explicable in terms of two uniform mantle layers. This poses the question of how heterogeneities can persist for so long in the presence of convection that must exist in each layer, whether there is one mantle layer or several. Moreover, the subducting oceanic lithosphere and crust is associated with distinct chemical signatures: how is this chemical anomaly stirred by mantle convection. These are two of the questions addressed in this thesis.

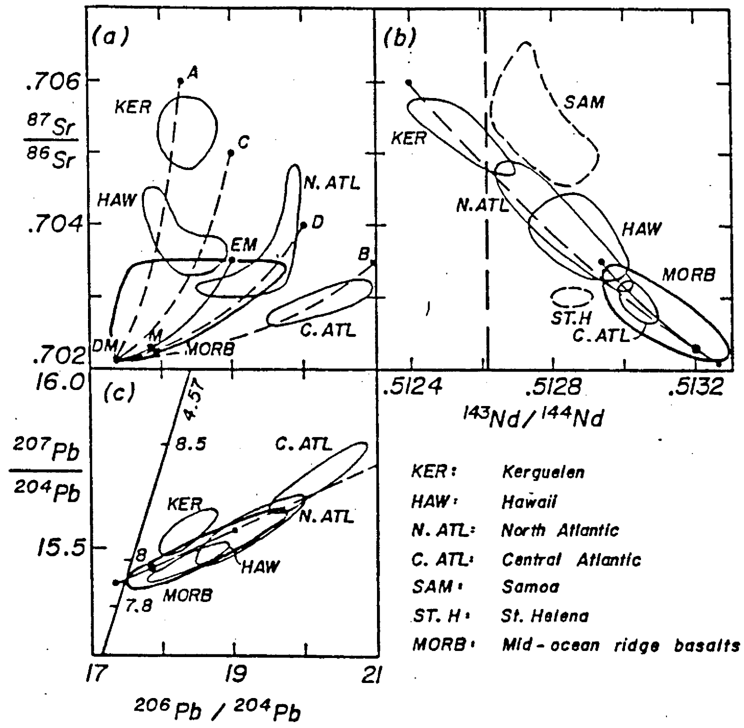

Fig. 3.1 Sr-Pb, Pb-Pb, and Sr-Nd isotope correlation diagrams for various oceanic basalts. The variation of the isotopic systematics requires at least three mantle components. The linear correlations on the Pb-Pb diagram are most easily interpreted as isochrons with ages of ~ 1-2 b.y. (from Davies [1984]).

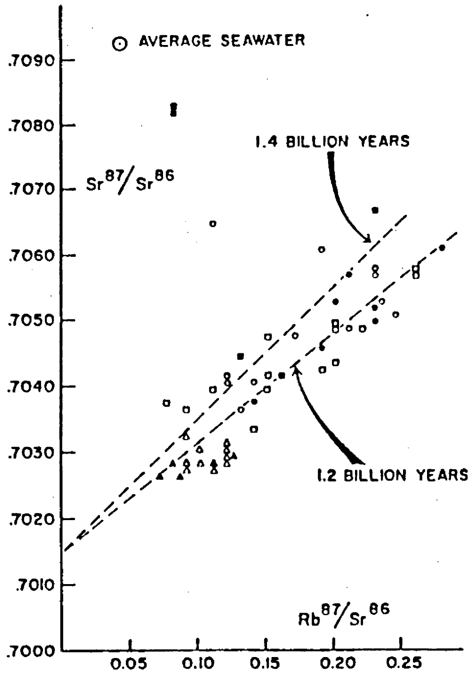

Fig. 3.2. Variation of $^{87}Sr/^{86}Sr$ versus $^{87}Rb/^{86}Sr$ for basalts from French Polynesia. The correlation can be intepreted in terms of an average isochron for the source of these Polynesian volcanics with an age of ≈ 1.2 b.y. (from Duncan and Compston [1976]).

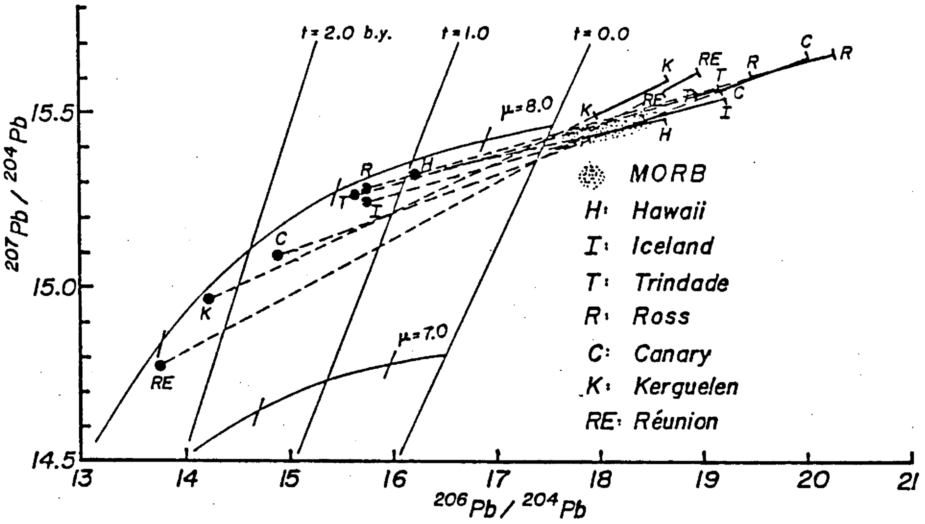

Fig. 3.3 Pb-Pb isotope plot for selected oceanic islands. The heavy lines are regressions through the linear arrays for the the particular islands. The dashed line is an extrapolation back to the primary parent to daughter ratio derived from two-stage evolution models assuming the linear arrays are isochrons. All the ialnds have the same growth curve, which also appears the to be the average growth curve for MORB. (from Davies [1984]).

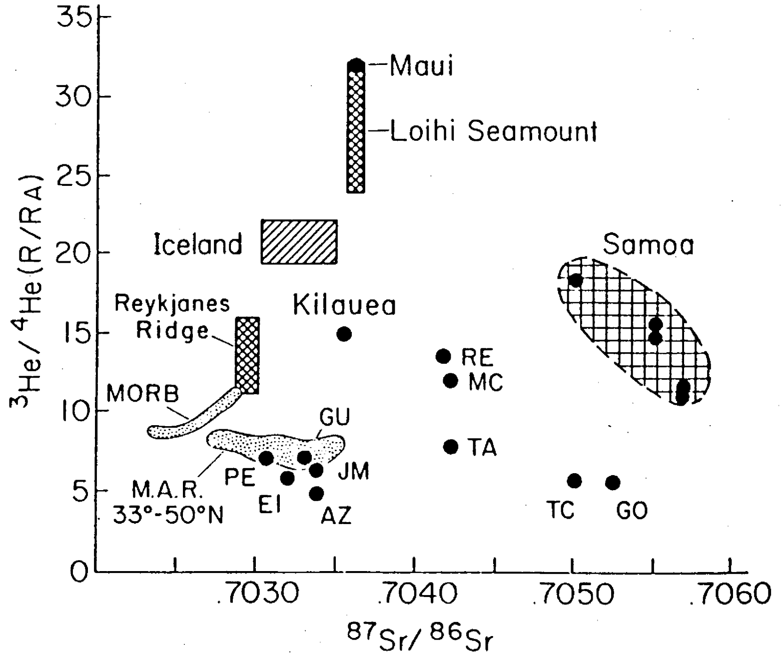

Fig. 3.4 Helium-Sr isotopic variations for oceanic basalts. Higher ^{3}He/^{4}He indicates less degassed mantle; most islands are less degassed than MORB. Some islands, in particular Tristan da Cuhna (TC) and Gough (GO) are more degassed than MORB and have a higher ^{87}Sr/^{86}Sr; these systematics suggest that the sources for TC and GO are recycled oceanic crust or sediments. (from Lupton [1983]).

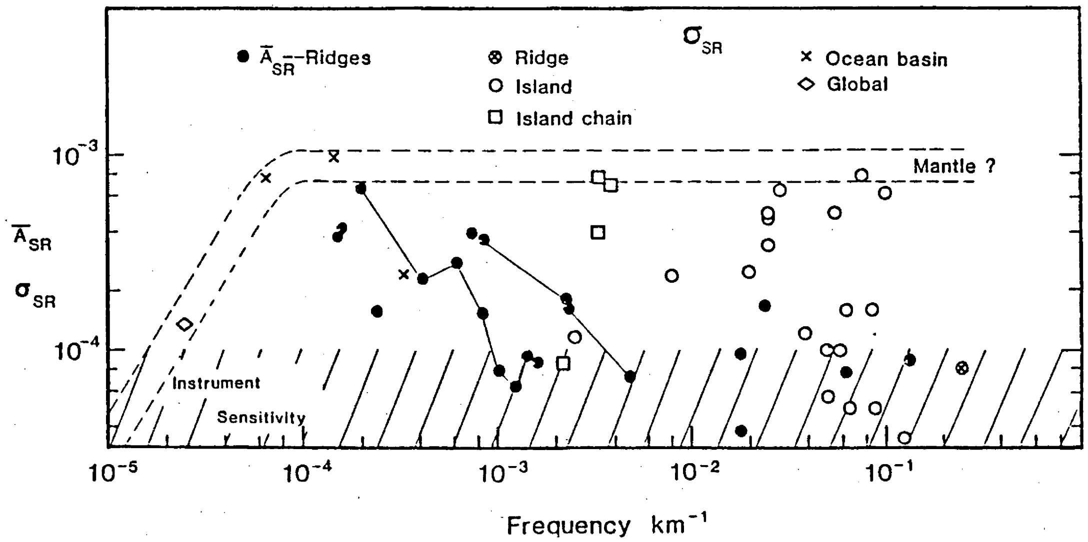

Fig. 3.5 Size-spectrum of $^{87}Sr/^{86}Sr$ variations in oceanic basalts. This demonstrates that comparable isotopic variations can be found over lengths from 10 km to nearly 10^4 km.

CHAPTER 4
DESCRIPTION OF NUMERICAL MODELS

4.1 Introduction to Model Set-Up

The central model-problem studied here is the mixing of chemically anomalous lithosphere by plate-scale mantle convection. Both kinematic and dynamic flows are employed. The mixing of passive material is well studied with kinematic flows, but for cases with variable viscosity and intrinsic chemical buoyancy, dynamic models are necessary. The models computed are idealized, but do retain dominant features of the mantle, including: unsteady plate kinematics, depth-dependent viscosity distributions, and introduction of chemical heterogeneity by subduction. The calculations should provide first order approximations to the mixing by plate-scale mantle flow.

For the dynamic models, the coupled heat and momentum equations are solved in a two-dimensional rectangular geometry. Although the flows are primarily driven by thermal buoyancy, they are organized by the use of velocity boundary conditions which allow the overall pattern of unsteady plate kinematics to be imposed. Some of the relevant features introduced into the computations are illustrated in Figure 4.1. As shown, tracers are introduced below the implicit trench to simulate subduction of chemically distinct lithosphere. The tracers are stirred by the convecting fluid and, in order to simulate recycling, are sampled when they pass through the lithosphere. The time each tracer spends in the box is recorded. In this way, the "residence time", the average time between successive cycling through the lithosphere is calculated. The residence time is significant for interpreting the isotopic systematics of the mantle. Also illustrated in Figure 4.1 are some of the complications, discussed in Chapter 2, which are introduced into the computations. The subducting lithosphere has intrinsic density because of its distinct mineralogy and this is denoted in the figure by the density ρ_L for the lithosphere compared to ambient mantle of density ρ_O. Two viscosity distributions are shown off to the right in Figure 4.1.

This chapter is organized in the following way. First, the governing equations are set out in an appropriate, non-dimensional format. Then the set of equations describing an unsteady analytical flow, used to study mixing of passive material, are set out. Then the numerical methods are reviewed. Some of the important boundary conditions and their assigned values are discussed in the final section of this chapter.

4.2 Governing Equations

There are essentially three equations governing the fluid flows: the equation of continuity, the momentum equation (sometimes called Stokes equation), and the energy (or heat) equation. With the use of the stream function formulation, see below, the continuity equation is essentially subsumed into the momentum equation. Moreover, with the existence of tracers in the models there is also an equation describing the advection of tracers.

4.2.1 Momentum Equation

Neglecting inertial terms [cf. McKenzie *et al.* 1974], the momentum equation [e.g. Landau and Lifshitz, 1959] with buoyancy, is written in tensor notation as

$$\frac{\partial \sigma_{ij}}{\partial x_j} - \rho g \lambda_i = 0 \qquad (4.1)$$

where $\lambda = (0,-1)$ and is the unit vector pointing in the direction of gravity, ρ is the density and is composed of both a thermal and a chemical component (see below), and σ_{ij} is the stress tensor:

$$\sigma_{ij} = -p\delta_{ij} + \tau_{ij} \qquad (4.2)$$

In (4.2) p is the pressure, δ_{ij} is the Kronecker delta, and τ_{ij} is the deviatoric stress tensor. In many of the flows considered in this thesis the viscosity is not spatially constant and the stress tensor is written as

$$\tau_{ij} = 2\eta \left(e_{ij} - \frac{1}{3} e_{ii}\delta_{ij} \right) \qquad (4.3)$$

where

$$e_{ij} = \frac{1}{2}\left(\frac{\partial u_i}{\partial x_j} + \frac{\partial u_j}{\partial x_i} \right) \qquad (4.4)$$

and η is the dynamic viscosity and depends only on position.

The equations will be non-dimensionalized as

$$\begin{aligned} (x',y') &= (x,y)/D \\ (u',v') &= (u,v)/V_o \\ T' &= T/\Delta T \qquad (4.5) \\ \eta' &= \eta/\eta_o \end{aligned}$$

where D is the depth of the box, ΔT is a temperature scale defined below, η_o is the dynamic viscosity at the top and

$$V_o = \frac{\rho_o g \ \alpha \ \Delta T \ D^2}{\eta} \qquad (4.6)$$

In (4.5) primed (') quantities are non-dimensional and un-primed quantities are dimensional. Hereafter, the primes are dropped from the non-dimensional quantities.

With this dimensionalizing scheme and with $(x_1,x_2) = (x,y)$ and $(u_1,u_2) = (u,v)$ equations (4.2), (4.3), and (4.4) are substituted into (4.1) and the curl is taken to eliminate the pressure [cf. Torrance and Turcotte, 1971]:

$$\nabla^2(\eta\omega) = - \frac{\partial}{\partial x}(\rho g) + \Lambda(\eta,u,v) \qquad (4.7)$$

where

$$\Lambda(\eta,u,v) = -2\left[\frac{\partial^2\eta}{\partial x^2}\frac{\partial u}{\partial y} - \frac{\partial^2\eta}{\partial y^2}\frac{\partial v}{\partial x} + \frac{\partial^2\eta}{\partial x\partial y}\left(\frac{\partial v}{\partial y} - \frac{\partial u}{\partial x}\right)\right] \qquad (4.8)$$

where x and y are the horizontal and vertical directions (y measured from the bottom upwards and x from the left), u and v the horizontal and vertical velocities, and ω is the vorticity and is defined as

$$\omega = \omega_{12} = \left(\frac{\partial v}{\partial x} - \frac{\partial u}{\partial y} \right) \qquad (4.9)$$

In the cases considered in this thesis only vertical variations in viscosity are considered, so that $\partial\eta/\partial x = 0$ and (4.8) becomes

$$\Lambda = \Lambda(\eta, v) = 2\,\frac{\partial^2 \eta}{\partial y^2}\,\frac{\partial v}{\partial x} \qquad (4.10)$$

In order to satisfy the equation of continuity,

$$\frac{\partial \rho}{\partial t} + \nabla\cdot(\rho\mathbf{u}) = 0 \qquad (4.11)$$

where t is time and $\mathbf{u} = (u,v)$, the stream function will be introduced. Moreover, the density varies as

$$\rho = -\rho_o\alpha(T-T_o) + \Delta\rho\Gamma \qquad (4.12)$$

where $\Delta\rho$ is the density difference between a parcel of fluid with ambient density, ρ_o, and a parcel with pure intrinsic density, and Γ is the volume fraction of chemically anomalous material. By employing the Boussinesq approximation, $\rho << \rho_o$, (4.11) becomes

$$\nabla\cdot\mathbf{u} = 0 \qquad (4.13)$$

The equation of continuity, (4.13), can be satisfied if a stream function, ψ, is defined as

$$u = \frac{\partial\Psi}{\partial y}, \qquad v = -\frac{\partial\Psi}{\partial x} \qquad (4.14)$$

With (4.14), equation (4.7) and (4.10) become

$$\nabla^2(\eta\omega) = \frac{\partial\rho}{\partial x} + 2\,\frac{\partial^2\eta}{\partial y^2}\,\frac{\partial^2\Psi}{\partial x^2} \qquad (4.15)$$

and with

$$\nabla^2\Psi = -\omega \qquad (4.16)$$

(4.15) and (4.16) comprise the complete momentum equation.

If the viscosity is spatially constant and there is no source of chemical buoyancy, then the momentum equation reduces to

$$\nabla^4\Psi = \frac{\partial T}{\partial x} \tag{4.17}$$

which is often called the biharmonic equation. Equation (4.17) can also be written as two coupled Poisson equations as

$$\nabla^2\omega = -\frac{\partial T}{\partial x} \tag{4.18}$$

$$\nabla^2\Psi = -\omega \tag{4.16}$$

If the viscosity remains constant, but there are sources of both thermal and chemical buoyancy, then the momentum equation becomes

$$\nabla^4\Psi = \frac{\partial T}{\partial x} - A\frac{\partial \Gamma}{\partial x} \tag{4.19}$$

where A is the density anomaly ratio,

$$A = \frac{\Delta\rho}{\rho_o \; \alpha \; \Delta T} \tag{4.20}$$

or

$$\nabla^2\omega = -\frac{\partial T}{\partial x} + A\frac{\partial \Gamma}{\partial x} \tag{4.21}$$

and eq (4.16).

Finally, if there is depth-dependent viscosity, but only thermal buoyancy, the momentum equation becomes

$$\nabla^2(\eta\omega) = -\frac{\partial T}{\partial x} - 2\frac{\partial^2\eta}{\partial y^2}\frac{\partial^2\Psi}{\partial x^2} \tag{4.22}$$

and eq (4.16). Moreover, if the viscosity is assumed to exponentially increase with depth as

$$\eta = 10^{\beta(1-y)} \tag{4.23}$$

equation (4.22) becomes

$$\nabla^2(\eta\omega) = -\frac{\partial T}{\partial x} - 2(\beta \ln 10)^2\eta\frac{\partial^2\Psi}{\partial x^2} \tag{4.24}$$

4.2.2. Energy Equation

The energy equation [McKenzie et al., 1974] which describes the production, advection, and diffusion of heat is not effected by either variable viscosity or chemical buoyancy. Using the non-dimensionalizing scheme of (4.5) the energy equation becomes

$$\frac{\partial T}{\partial t} + \nabla\cdot(\mathbf{u}T) = \frac{1}{Ra}\,(\nabla^2 T + \mu) \qquad (4.25)$$

where Ra is the Rayleigh number

$$Ra = \frac{g\ \rho_o \alpha\ \Delta T\ D^3}{\kappa\ \eta_o} \qquad (4.26)$$

and μ is the ratio of internal to total heat production

$$\mu = \frac{H\ D^2}{K\ \Delta T} \qquad (4.27)$$

In (4.26) and (4.27), H is the rate of internal heat production per unit volume, K is the thermal conductivity, and κ is the thermal diffusivity, defined as

$$\kappa = \frac{K}{\rho c_p} \qquad (4.28)$$

ΔT in equations (4.5) and (4.26) can be defined in two ways. If the bottom and top of the fluid are held at the constant values of T_b and T_t, respectively, then

$$\Delta T = T_b - T_t \qquad (4.29)$$

while if heat input Q is specified

$$\Delta T = \frac{Q\ D}{K} \qquad (4.30)$$

With these two definitions of ΔT, the Rayleigh number (4.26) can be redefined in two ways

$$R_T = \frac{g\ \rho_o\ \alpha\ D^3\ (T_b - T_t)}{\kappa\ \eta_o} \qquad (4.31)$$

where the subscript T is used to emphasize a definition in terms of a temperature difference. Alternatively, the Rayleigh number maybe defined with the use of (4.30)

$$R_Q = \frac{g\ \alpha\ \rho_o\ D^4\ Q}{K\ \kappa\ \eta_o} \qquad (4.32)$$

where the subscript Q is used to emphasize the fact that Ra is defined in terms if a constant heat flux. For the various definitions of Ra, η_o is the viscosity at the top of the convecting layer when depth-dependent viscosity is employed. Other definitions are obviously possible, as discussed in Chapter 6.

4.3 Analytic Flows

Insight into the mixing of tracers can be gained with simple kinematic flows prescribed by analytic stream functions; the analytic flows exhibit features displayed by the full solution of the governing equations. These calculations are valuable because both a wider range and a better controlled set of parameter values can be employed. Moreover, material lines, which are defined by tracers, can be accurately followed. The principal features incorporated into the flows are growth and shrinkage of cells and the positioning of a source of chemical anomaly on the edge of cells. This can be accomplished with two cells rotating in opposite directions (descending flow between them) and with tracers being introduced at a point source between the cells. A stream function for such a flow is

$$\begin{aligned} \Psi &= A(t)\ \sin\left\{\pi \frac{x}{X(t)}\right\}\ \sin(\pi y) \qquad x < X(t) \\ & \qquad\qquad\qquad\qquad\qquad\qquad\qquad\qquad (4.33) \\ \Psi &= B(t)\ \sin\left\{\pi \frac{x-X(t)}{w-X(t)}\right\}\ \sin(\pi y) \qquad x > X(t) \end{aligned}$$

In (4.33) the stream function, Ψ, is defined in (4.14). Similar equations have been used to approximate convection cells previously [Richter <u>et</u> <u>al</u>., 1982; Olson <u>et</u> <u>al</u>., 1984a]. In (4.33) the width of the box is w (depth being unity), and the x coordinate is positive to the right and y positive upward. The boundary between the cells is X(t). With the definition of the stream function in (4.14), (4.33) characterizes clockwise flow on the left and counter-clockwise on the right; this gives downwelling at X(t). The vertical velocity of the flow must be continuous at X(t),

$$\left[\frac{\partial\psi}{\partial x}\bigg|_{+} = \frac{\partial\psi}{\partial x}\bigg|_{-} \right]_{x=X} \qquad (4.34)$$

If A and B have the following form

$$A(t) = CX(t) \qquad (4.35a)$$

$$B(t) = C\,[w-X(t)] \qquad (4.35b)$$

then the flow (4.33) satisfies (4.34). The coefficient, C, is the flow amplitude. The boundary between the cells oscillates as

$$X(t) = w/2\left[\ 1 + E\sin(\Omega t)\ \right] \qquad (4.36)$$

where E is the margin amplitude and Ω is the margin frequency. The velocity field is easily found by differentiating (4.33) using the definition of Ψ in (4.14).

4.4 Numerical Solution

4.4.1 Fluid Flow

The problem set-up described in section 4.1 requires that the sides of the box be insulating and free slip, that the bottom be free slip and have either an isothermal or an imposed heat flux, and that the top have an imposed surface velocity and be isothermal. In the context of the parameters presented in section 4.2, these boundary conditions are

All boundaries: $\Psi = 0$

Sides: $\omega = 0$
$\partial T/\partial x = 0$

Top: $\partial\Psi/\partial y = u_b U^u(x,t)$ (4.37)
$T = 0$

Bottom: $\omega = 0$
$T = 1,$
or $\partial T/\partial y = 0$

Where $U^u(x,t)$ is referred to as the plate evolution model and u_b is the non-dimensional boundary velocity.

The heat and momentum equations are solved on a discrete mesh with finite differences. ψ and ω are known on one mesh which is staggered with respect to the T and Γ mesh, as shown in Figure 4.2. An efficient cyclic reduction method is used [Sweet, 1974] to solve the Poisson equation and the subroutine was coded and extensively tested by the National Center for Atmospheric Research (NCAR), USA [Swarztrauber and Sweet, 1975]. The momentum equation is broken into a pair of Poisson equations (e.g. either 4.18, 4.21, or 4.22 and 4.16 depending upon the type of variable viscosity and driving densities); each Poisson equation is solved successively by the cyclic reduction method. The methods of solving the momentum equation in conjunction with the stream function/vorticity formulation when velocities are imposed has been described by Lux [1978] and Davies [1986a]. The heat equation (4.25) is solved by the Alternating Direction Implicit (ADI) method as formulated in this case by Lux [1978], who followed Houston and DeBremaecker [1974]. Upwind differences have been employed.

The purpose of the top velocity boundary condition is to simulate an important characteristic of the high viscosity oceanic lithosphere, which tends to organize the flow (as discussed in Chapter 2). $u_b U^u(x,t)$ is the full dimensionless velocity boundary condition imposed on the top surface of the box. The dimensional imposed velocity is characterized by a Peclet number which is defined as

$$Pe = \frac{U_b D}{\kappa} \qquad (4.38)$$

V_o, the characteristic velocity defined in (4.6), can be rewritten using (4.26) as

$$V_o = \kappa Ra/D \qquad (4.39)$$

Therefore, the non-dimensional velocity, $u_b = U_b/V_o$, can be recast using (4.38) and (4.39)

$$u_b = \frac{U_b}{V_o} = \frac{Pe}{Ra} \tag{4.40}$$

In the presence of variable viscosity, an iterative solution was used. In particular, the second term on the right hand side of (4.24), arising from the viscosity variations, is not known a priori, and was found by iteration, as follows. A parameter ξ is define as

$$\xi_{ij} = \nabla^2(\eta\ \omega)_{ij} \tag{4.41}$$

The algorithm consists of the following sequence of operations:

1. $\xi^{n+1}_{ij} = (1-\phi)\ \xi^{n}_{ij} + \phi\ C^2\ \eta\ (\psi^{n}_{i,j+2} + \psi^{n}_{i,j} - 2\ \psi^{n}_{i,j+1})$ (4.42)

   where n is an iteration counter and $C = \beta \ln 10$

2. $\varepsilon = \max \left| \xi^{n+1}_{i,j} - \xi^{n}_{i,j} \right|$ all i,j (4.43)

3. The Poisson equation of (4.24) is solved for ω.
4. The Poisson equation (4.16) is solved for ψ.
5. If $\varepsilon > \varepsilon_o$ return to step 1 and carry out the sequence again. If $\varepsilon < \varepsilon_o$ go on to solve the heat equation.

The quantity ξ converged quickly at every time step, and in general required no more than 2 passes through steps 1 - 5, except for the first 2 time steps when the calculation starts, when n up to 5 is required. A $\phi = 0.5$ was used for all cases with depth-dependent viscosity of the exponential form, except for the few runs at $\beta = 3$, when a ϕ of 0.3 was used; when a layered viscosity distribution was employed, then an $\phi = 0.1$ was required. An ε_o of 3×10^{-5} was used in all cases.

In high Rayleigh number convection, the thermal boundary layers become quite thin [McKenzie et al., 1974] and therefore a fine numerical mesh is needed to resolve the thermal structure. Moore and Weiss [1973] suggest that at least three mesh points spanning the thermal boundary layers are needed for calculations accurate to within one percent. For the new calculations presented in this paper there were at least three mesh points across a thermal boundary layer, except in a few cases which will be pointed out in the text, and

Nusselt numbers and other quantities have errors of five percent or less; this was determined by running the code with the same parameters, but different grid sizes.

4.4.2 Tracers and Chemical Density

The tracers are advected by the background velocity, **u**, by

$$\mathbf{x}^k = \mathbf{x}_o^k + \int \mathbf{u}(\mathbf{x}^k)\, dt \qquad (4.44)$$

where $\mathbf{x}^k$ are the coordinates of the k^{th} tracer and $\mathbf{x}_o{}^k$ are the initial positions. Moreover, the fraction of anomalous material, Γ, is a function of the tracer positions

$$\Gamma = \Gamma(x^k) \qquad (4.45)$$

Advection and material lines. The positions (x,y) of the tracers are integrated forward using the velocity field calculated from the momentum equation. A predictor-corrector scheme was employed with two steps for each coordinate

$$x^c_{k,\ell} = x_{k,\ell-1} + \frac{\Delta t}{2}\, u(x_{k,\ell-1}, y_{k,\ell-1}, t_{\ell-1}) \qquad (4.46)$$

$$x_{k,\ell} = x_{k,\ell-1} + \Delta t[\zeta u(x^c_{k,\ell}, y^c_{k,\ell}, t_{\ell-1}) + (\zeta-1)u(x^c_{k,\ell}, y^c_{k,\ell}, t_\ell)] \quad (4.47)$$

and a similar set for the y coordinate. In (4.46) and (4.47) $x^c{}_{k,\ell}$ is the temporary centered position for tracer k at time step ℓ, Δt is the time step, $t_{\ell-1}$ is the time at step ℓ-1, and ζ is the predictor-corrector parameter and was always set to 0.5.

In the case of the analytic flows the velocity is known exactly everywhere, while for the dynamic models the velocity must be interpolated from ψ values at the grid points to the tracer positions; 2nd order polynomials were used for the interpolations. The advection algorithm was tested by advecting tracers around closed convection cells. A tracer accumulated an error O(10^{-6}) for analytic flows and O(10^{-3}) for the dynamic convection flows (with 16 mesh points). The accuracy with which tracers could be advected in the dynamic flows was limited by the accuracy of the stream function; the accuracy of the stream function was limited by the number of mesh points [Lux, 1978] and the computer word size (32 bits) [Roache, 1982].

The tracers can also define a material line, a line always consisting of the same fluid particles

$$\ell = \oint |d\boldsymbol{\ell}| \qquad (4.48)$$

where $d\boldsymbol{\ell}_i = \mathbf{x}_{i+1} - \mathbf{x}_i$, is a small segment of the material line. Material lines can also be defined by a set of tracers. As the material lines are advected, the distance between tracers can increase and in order to maintain accuracy, when the distance between two adjacent tracers exceeds a set distance an additional tracer is placed between them. For the advection of material lines in the analytic flows a minimum distance of 0.02D was employed; this value was determined empirically such that if this distance was halved there was no significant change in the material line. This method was also employed by Hoffman and McKenzie [1985].

Chemical density. If A of (4.20) was ≠ 0, then the tracers have intrinsic buoyancy. For the numerical calculations presented here, the thermal convective flows were defined in terms of a constant heat flux, Q, instead of a constant temperature difference between top and bottom. With such a parameterization, the density anomaly ratio, A, can be redefined as the Rayleigh number already has, cf. (4.32). Substituting (4.30) (e.g. $\Delta T = QD/K$) into (4.20)

$$A_Q = \frac{\Delta\rho \; K}{\rho_o \alpha \; Q \; D} \qquad (4.49)$$

where the subscript Q is used to distinguish it from A defined in terms of ΔT; (4.20) is hereafter denoted as A_T.

The intrinsic chemical density, Γ, is cast into a mesh with uniform spacing and is treated in the same way as the T array when the momentum equation is solved. After all the tracers are advected, the value of Γ at a mesh point is re-calculated from the tracers within a cell of size $\Delta x \; \Delta y$ around a mesh point. Γ at mesh i,j is

$$\Gamma_{ij} = \frac{N_{ij}}{N_m} \qquad (4.50)$$

where N_{ij} is the number of tracers in cell ij, and N_m is a normalizing factor (Figure 4.3)

$$N_m = \frac{S_c}{s_{tr}} = \frac{S_c}{\dot{s}\ \Delta t} = \frac{\Delta x\ \Delta y}{\delta w\ u_b\ \Delta t} \qquad (4.51)$$

where S_c is the area of one cell, S_{tr} is the "equivalent" area of a single tracer, $\dot{s}$ is the non-dimensional flux, $\delta w u_b$, δw is the normalized thickness of anomalous material, u_b is defined in (4.40), and Δt is the time between tracer introductions which is also the time step.

The use of an implicit thickness of the anomalous material, δw, smaller than the mesh spacing does not introduce spurious mixing, as long as a single "tracer" has a negligible Stokes velocity. This restriction is satisfied for the cases investigated in Chapter 7. Moreover, the Stokes velocity in the two-dimensional models is independent of the radius, for a constant anomalous mass: it can be shown [cf. Batchelor, 1967] that the two-dimensional Stokes velocity has the form

$$U_c \propto \frac{g\ \delta\sigma\ a^2}{\eta} \qquad (4.52)$$

where $\delta\sigma$ is the two-dimensional density. If the two-dimensional mass is $\delta\theta$ (= $\delta\sigma\ \pi\ a^2$), where a is the radius of the area the mass is averaged over), then the Stokes velocity is

$$U_c \propto \frac{g\ \delta\theta}{\eta} \qquad (4.53)$$

If $\delta\theta$ is the mass of a tracer (or a clump of them), then the two-dimensional Stokes velocity is independent of the mesh spacing they are averaged over. The rather coarse mesh used for most of the cases with chemical density, 16x64, should not introduced spurious effects; this was confirmed when some of the cases originally computed using a 16x64 mesh were recomputed using a 32x128 mesh.

Tracer introduction and sampling. Tracers were introduced into the flows in two ways: either below the implicit trench (or margin of cells in the analytic flows, X(t)) or as a uniform layer at the base of the convecting layer. When a tracer is introduced below the margin it is placed a distance of 0.02 from the top.

In the dynamic flows, the tracers could also be sampled. When a tracer passes through a square with sides d_s directly under the sampling point (see Figure 4.1), it is removed from the flow. The sampling zone was placed midway between the diverging and converging margin. The zone was not placed directly under the margin because the velocity boundary condition, $U^u(x,t)$, was smoothed over five grid points; consequently, the horizontal and vertical velocities directly under the margins were reduced in comparison to a margin with a step-function type velocity distribution. The tracers would be artificially slowed when traversing this area and the rate of sampling would be reduced. The top surface velocity, boundary condition was smoothed to reduce numerical inaccuracy in calculating the flow [Davies, 1986a]. This is a simplification from the mantle, where sampling occurs directly beneath the ridge, R (Figure 4.1), in the zone of partial melting, but is valid since it is the cycling of material through the lithosphere we wish to measure.

Because tracer sampling was intended to simulate the sampling of the mantle by sub-ridge magmatism, the sampling size, d_s, should be on the order of the length-scale of magmatism which is of the order of 100 km, see Chapter 10; for whole-mantle convection, $d_s=0.05$, and for convection confined to the upper mantle, $d_s=0.15$.

4.4.3 Model Times

The times with which the model results are referred to have been scaled to transit times, which is the time to traverse the fluid depth with a characteristic surface (plate) velocity, e.g.

$$t_t = \frac{D}{U_b} \tag{4.54}$$

which is dimensional. For the dynamic flows the non-dimensional transit time using (4.40) becomes

$$t_t = \frac{Ra}{Pe} = \frac{1}{u_b} \tag{4.55}$$

For the kinematic flows a surface velocity, $\langle U_x(y=1)\rangle$, can be found by averaging the sinusoidal surface velocity. It can be shown that the average of the horizontal velocity derived from equation (4.33) is

$$\begin{aligned} \langle U_x(y=1)\rangle &= -2CX(t) & 0 < x < X(t) \\ \langle U_x(y=1)\rangle &= 2C[w-X(t)] & X(t) < x < w \end{aligned} \qquad (4.56)$$

and for the entire surface

$$\langle U_x\rangle = Cw\ (1 + E^2/2) \qquad (4.57)$$

The transit time is thus

$$t_t = \frac{D}{\langle U_x\rangle} = \frac{1}{Cw(1+E^2/2)} \qquad (4.58)$$

when D=1.

4.5 Boundary Conditions and Choice of Parameters

4.5.1 Force Scaling and Choice of Rayleigh Number.

The Rayleigh number, Ra, for the mantle, especially for whole-mantle convection, is large (see below) and would require very fine grid spacings to resolve the thermal boundary layers. Low values of Ra (about 10^5 to 10^6) were employed, on the one hand, to avoid excessive computation times and, on the other, to suppress small-scale instabilities of the thermal boundary layers. Because the viscosity is uniform for most cases studied, realistic Ra's lead to the artificial instability of the top boundary layer; in the mantle this instability is strongly suppressed because of the high viscosity of the lithosphere [Yuen et al., 1981]. Because the calculations presented here were intended to study the effect of only the large scale flow associated with plates, these small-scale instabilities, which start to form at Ra > 10^6 in a constant viscosity fluid [McKenzie et al., 1974], must be inhibited. Therefore a Ra of 10^5 was used for most calculations with constant viscosity. For cases with depth-dependent viscosity, Ra's of up to 5×10^6 were used.

Because of the reduction of Ra, the Peclet number, Pe, must be scaled to maintain the same ratio of boundary driven to buoyancy driven forces in the model as they are in the mantle. They scale as [Turcotte and Oxburgh, 1967; Davies, 1986a]

$$Pe = \chi' R_T^{2/3} = \chi R_Q^{1/2} \qquad (4.59)$$

where χ' and χ are constants. Shown in Figure 4.4 is the R_Q-Pe domain for whole-mantle convection. Shown in the upper right is the preferred whole mantle value found by evaluating the primary parameters listed in Table 4.1. A wider range of values is permissible if the uncertainty in the lower mantle viscosity is accounted for. If the mantle $R_Q = 1.7 \times 10^9$ and Pe = 4800 and if a scaled model R_Q of 10^5 is used, then the model Pe=40; in order to account for the uncertainty Pe is varied between 20 and 100 in the models presented in Chapter 5 (open circles Figure 4.4). In chapter 6 a wider range of the Pe-R_Q domain is considered when the effect of depth-dependent viscosity is explored. Upper mantle convection parameters are also presented in Table 4.1.

4.5.2 Plate Models

In order to account for the uncertainty in long term plate evolution, as discussed in Chapter 2, two types of models, cf. $U^u(x,t)$ of (4.37), are employed: periodic plate models and pseudo-random models. Two of the plate models are shown schematically in Figure 4.5. The plate model "a", Figure 4.5a is used most often and is discussed in detail. In this figure, distance across the box is represented horizontally, and the progression of time (in transit times) vertically. The sketches to the right of the box are intended to clarify the plate tectonic configuration at two instants. Solid lines are drawn between plate margins; a stationary margin plots vertically (for example the trench labeled "T"), but the ridge (labeled "R") migrates to the right. During the first stage, a symmetrically spreading ridge starts at x = 1, migrates to the right, and reaches the trench at time 6. A new trench forms at the collision point, migrates to the left until it coalesces with the ridge. The orientation of the arrows shows the speed and direction of plate motion. The dashed line indicates plate rearrangement with a new sequence below the line. When time 10 is reached, the plate sequence repeats, starting again at time zero. This model is idealized but simulates the uniform velocity across plates, the symmetric flow at ridges, the asymmetric flow at trenches, and the migration of ridges and trenches. An additional periodic plate model "b" was also used, Figure 4.5b.

A third model, referred to as "pseudorandom" in the sense that no repetitions or periodicities were incorporated a priori was also employed. This model has 27 distinct stages of plate motion that were between 1 and 9 transit times in length during the first 100 transit times. The number of plates during each stage was between two and five. Plate evolution included trench migrations and ridge migrations, both singly and in combination. However, there was only one source and one sink of tracers during each stage.

TABLE 4.1. Primary Quantities

Quantity	Description	Value	Reference
g	Gravitational acceleration	$10\ \mathrm{m\ s^{-2}}$	
α	Coefficient of thermal expansion	$2 \times 10^{-5}\ \mathrm{K^{-1}}$	Turcotte and Schubert [1982]
K	Thermal conductivity	$3\ \mathrm{W\ K^{-1}\ m^{-1}}$	Turcotte and Schubert [1982]
κ	Thermal diffusivity	$10^{-6}\ \mathrm{m^2\ s^{-1}}$	Turcotte and Schubert [1982]
ρ_o	Ambient density		
	Whole mantle	$4000\ \mathrm{kg\ m^{-3}}$	Turcotte and Schubert [1982]
	Upper mantle	$3500\ \mathrm{kg\ m^{-3}}$	Turcotte and Schubert [1982]
D	Depth of convection		
	Whole mantle	$3 \times 10^{6}\ \mathrm{m}$	
	Upper mantle	$7 \times 10^{5}\ \mathrm{m}$	
η	Average viscosity	$10^{21}\ \mathrm{Pa\ s}$	Peltier [1983]
q	Surface heat flux	$0.080\ \mathrm{W\ m^{-2}}$	Davies [1980a]
ΔT	Temperature across lithosphere	$1400\ \mathrm{K}$	Cazenave [1984] and Parsons and Sclater [1977]
U	Average horizontal velocity	$5\ \mathrm{cm\ yr^{-1}}$	Chase [1972]

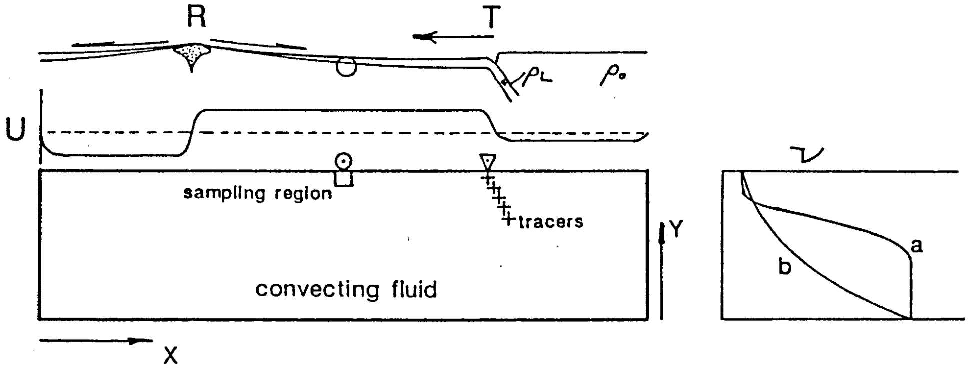

Fig. 4.1. Schematic of the thermal convection model used to study mixing. Shown is the relation between the top imposed velocity, U, and the plate tectonic configuration. "R" is the implicit ridge and "T" is the implicit trench. The tracers are introduced below the triangle and sampled below the circle, sampling region of depth d_s. Off to the right are two viscosity distributions used.

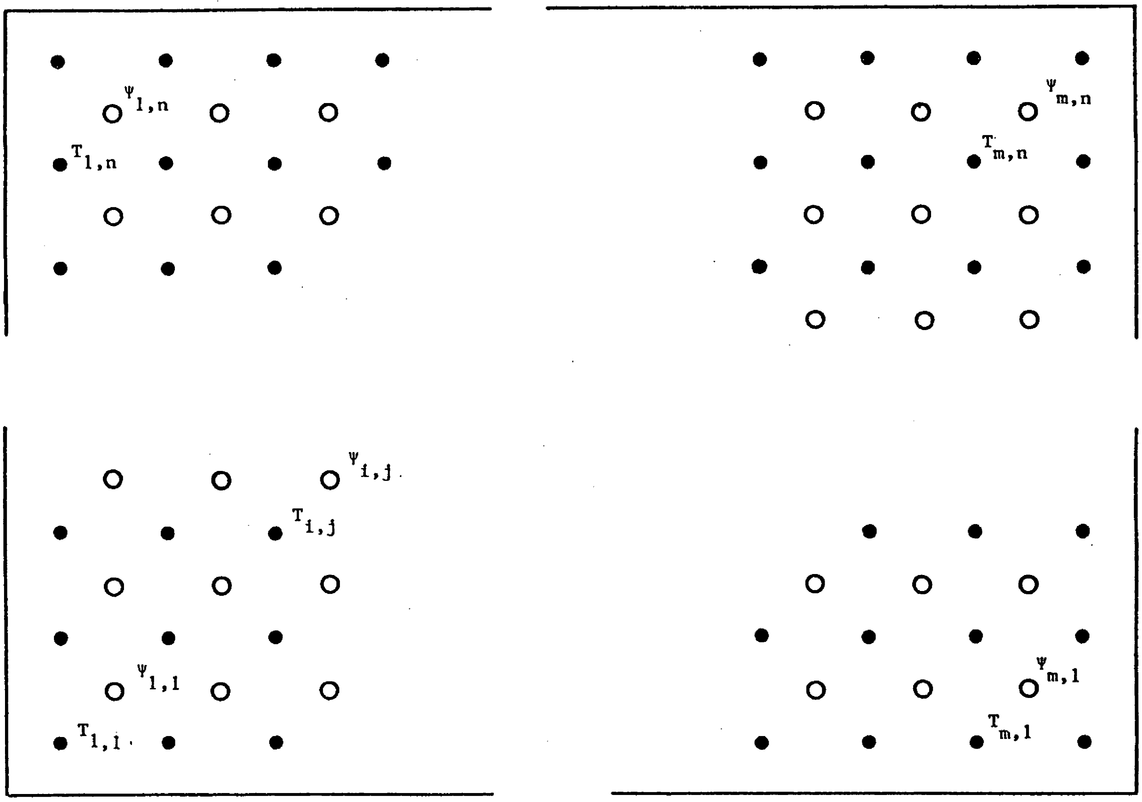

Fig. 4.2. Schematic of the finite difference grid. T is the temperature grid and ψ the stream function grid. The mesh spacing $\Delta x = 1/(m+1)$. There are m x n internal ψ nodes and (m+1) x (n+1) internal T nodes.

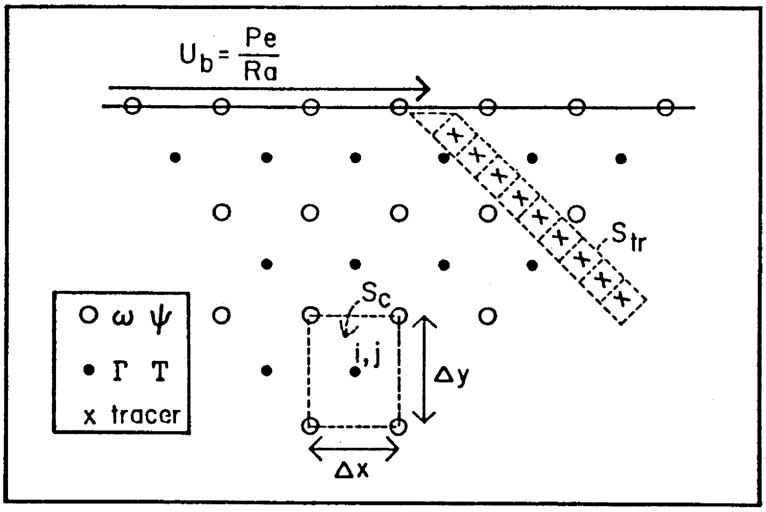

Fig. 4.3. Schematic of part of the mesh in the region of tracer introduction. u_b is the characteristic top plate velocity. Immediately after the tracers are introduced, they have an approximate spacing of $u_b \cdot \Delta t$, where Δt is the time step. An implicit area, S_{tr}, is assigned to each tracer. S_c is the area of a cell. The value of Γ at a node is proportional to the number of tracers falling within the cell.

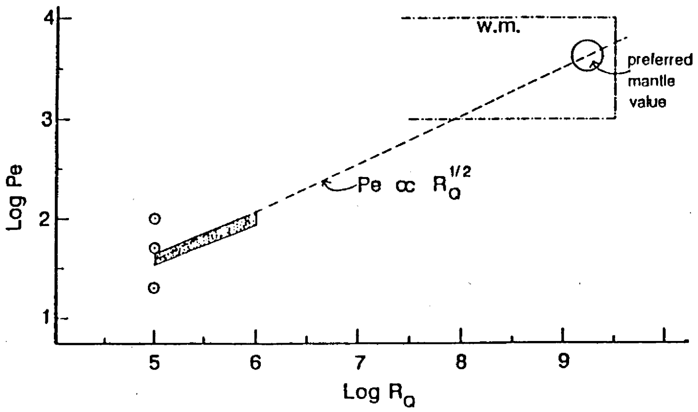

Fig. 4.4. The R_Q-Pe domain for whole-mantle convection and models intended to represent the whole-mantle convection scenario. The stippled area are the results of constant viscosity convection with internal heating and with free-slip sides from McKenzie et al. [1974] and Gurnis and Davies [1986]. Other parameters described in text.

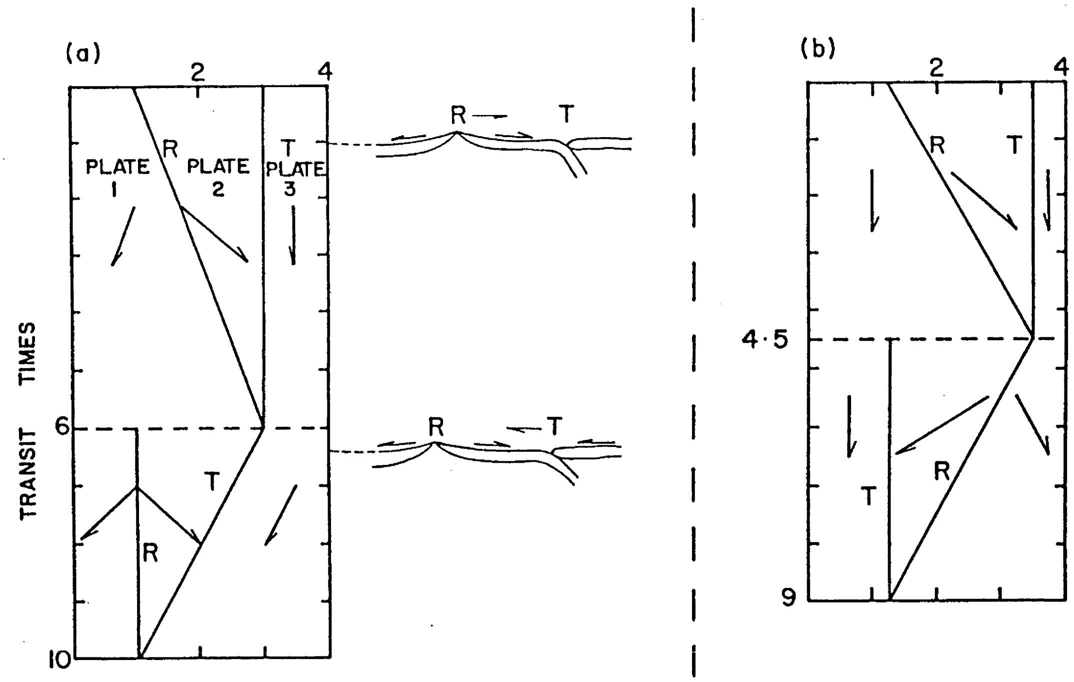

Fig. 4.5. Schematics of idealized plate evolutionary models used as velocity top boundary conditions for convection calculations. The plots are described in detail in the text. Distance across the top of the convection box is denoted horizontally and the time (scaled by the transit time) vertically. Ridges are labelled "R" and trenches "T"; the arrows denote the direction and speed of plate motion. For (a) the plate tectonic configuration is clarified by two sketches off to the right.

CHAPTER 5

STIRRING OF PASSIVE HETEROGENEITIES

In this chapter some simple computations are presented in which the fluid viscosity is constant and the heterogeneities are completely passive. As indicated in the previous chapters there are fundamental gaps in our understanding of how heterogeneities are stirred by plate-scale flow. When a thin sheet is introduced at the margin of an unsteady convection cell how is it stirred? When an heterogeneity is smaller than the scale of the flow how is it stirred? Does such a small heterogeneity follow a laminar mixing law or a turbulent mixing law? In this chapter, the stirring of a small circular heterogeneity is investigated using a material line formulation and a comparison is made to simple mixing laws. Using the same flow, the mixing of thin sheets introduced at the margins of cells is investigated using both the material line and the tracer formulations. The generality of the mixing results is explored, using progressively more sophisticated flows derived from dynamic thermal convection calculations. Finally, a comparison is made to other studies of the stirring of passive heterogeneities.

5.1 The Stirring of Small Heterogeneities in Unsteady Flow

The material line, perimeter, of a small, initially circular, patch of fluid is followed in the unsteady, periodic flow defined by (4.33). The flow has two counter rotating cells in a 2x1 box with an oscillating margin between the cells. All the controlling parameters were set, e.g. $E=1$, $\Omega=1$, and $C=1$ in (4.33), so that the average margin velocity is on the order of the flow velocities of the cells (i.e. $\Omega E/C = 1$). Circular heterogeneities, bound by material lines, were placed at mid-depth in the box and stirred by the flow. Six initial positions, six cases, were studied to ascertain the amount of variation obtained within just one flow pattern. In all cases, the initial size of the heterogeneities was $\theta_o/D = 0.1$, where θ_o is the initial diameter and D is the depth of the flow.

One case is shown at four instants in Figure 5.1. The circular element becomes progressively sheared out and after a number of transit times of stirring is made up of "tendrils" of small width. The average width across the heterogeneity, $\langle\theta\rangle/\theta_o$, can be found from the material line length, ℓ (4.48) via (1.3) and this quantity is plotted against transit time in Figure 5.2. Up to about 10 transit times $\langle\theta\rangle/\theta_o$ decreases slightly faster than $t^{-1/3}$ but significantly slower than the t^{-1} predicted by laminar mixing. Moreover, $\langle\theta\rangle/\theta_o$ also shows oscillations of about one transit time period superimposed on the $t^{-1/3}$ trend. This oscillatory behavior was previously noted by Hoffman and McKenzie [1985] and is caused by position dependent variations in shear and normal strains; the ellipsoidal heterogeneity is sheared out and then partially unmixed as it circulates around a convection cell. After 10 transit times tendrils have developed (Figure 5.1) and the tendrils often advect into stagnation points because they are larger than the scale of flow; such behavior causes the material line length, ℓ, to exponentially increase and $\langle\theta\rangle/\theta_o$ to exponentially decay.

The behavior illustrated by Figure 5.2 suggests that during a certain initial period, the heterogeneity is sheared out by laminar flow, but then makes a transition to turbulent-like mixing. However, inspection of Figure 5.1 reveals that characterizing heterogeneity with such a single, average parameter may be misleading because there is always a region of heterogeneity with width ~ θ_o. The inset (Figure 5.1) shows the maximum sized heterogeneity at transit time 22.5, with indicated width of $\theta_{max}/\theta_o = 0.26$. However, the average width at this time is only $\langle\theta\rangle/\theta_o = 0.0022$ which is more than two orders of magnitude smaller than the maximum width. For all times and for all initial placements of heterogeneities, there was always a maximum sized blob as shown in Figure 5.1. The size of these heterogeneities were measured, as indicated in Figure 5.1 (inset), and are plotted in Figure 5.3 as open circles. Also plotted in Figure 5.3, as solid circles, are $\langle\theta\rangle/\theta_o$ and again averaged for the six cases investigated. The oscillatory behavior noted in Figure 5.2 is averaged out. The error bars are one standard deviation between heterogeneities with different initial positions.

The θ_{max}/θ_o values start deviating from the $\langle\theta\rangle/\theta_o$ curve at approximately six transit times, the average $\langle\theta\rangle/\theta_o$ transition between laminar and turbulent mixing. This behavior is easily understood. A small heterogeneity is sheared within a cell and becomes thinner at a rate proportional to t^{-1} (c.f. equation 1.3). The flow is unsteady and the heterogeneity is eventually transferred to an adjacent cell; the sense of the shear is almost always reversed in an adjacent cell and the heterogeneity is partially unmixed [Heller, 1960]. Thus, as blobs are occasionally transferred to adjacent cells, and partially unmixed, their width must obviously decay less rapidly than t^{-1} predicted by steady laminar shearing. In Figure 5.3, θ_{max}/θ_o is shown to decay less rapidly than t^{-1}. Unmixing is nothing special, it is merely a product of laminar flow; laminar flow can both increase and decrease concentration gradients, as has been long known [Eckart, 1948]. Moreover, unmixing also causes the oscillatory behavior occurring prior to ~ 10 transit times, as noted above.

While the blobs are stirred in this way, tendrils are stirred quite differently. Tendrils are larger than the length-scale of unsteady flow and are frequently advected into stagnation points and pulled apart. Tendrils exponentially stretch with time. Apparently, because long tendrils approximately satisfy the conditions of the turbulent mixing law (as discussed in section 1.1), they behave accordingly. In time, because the surface area of tendrils become so large, in fact much larger than the surface area of blobs, the mere existence of blobs is obscured in measured quantities related to material lines.

Since blobs are sheared primarily by laminar flow, with partial unmixing, the size of blobs should decay less rapidly than t^{-1}. A good fit is found to the averages of blob widths with

$$\frac{\theta_{max}}{\theta_o} = \left[1 + \frac{3}{2} \left(\frac{t}{t_t} \right)^{1/3} \right]^{-1} \qquad (5.1)$$

The time for θ_{max}/θ_o to be reduced to 0.1 is 220 transit times.

The corresponding time for $\langle\theta\rangle/\theta_0$ to be likewise reduced is 9 transit times, or 24 times more quickly compared to the maximum width.

In Summary, large fractions of anomalous fluid are stirred by laminar flow, despite the fact that there is complete rearrangement of flow. The decay of θ_{max}/θ_0 is less rapid than the t^{-1} fall off because of unmixing. However, tendrils are mixed in a turbulent fashion because they are longer than the scale of flow.

5.2 Stirring of Sheets in Simple Analytic Flows

Crust and lithosphere are located at the margins of convection cells and initially parallel to stream lines. An obvious question to ask is, Does the behavior found for the initially circular heterogeneities also hold in this case? In order to address this question, heterogeneities where introduced at the margin between the two growing and shrinking cells of the periodic flow. Single tracers were introduced as a single stream for a wide range of unsteady flows. One case is also studied using the material line formulation.

One example is shown in Figure 5.4, and each frame is labeled by the transit time. In this case, 150 tracers are introduced over 2.4 transit times. The flow is the same as that used in the previous section to study the stirring of small circular blobs. As the margin moves to the right, as shown at times 1.2 and 2.4, the tracers are placed on streamlines progressively further from the center of the left cell. Because the angular velocities decrease from the center of the cell, this string of tracers will be progressively sheared. After time 4.8, the margin starts to move back toward the left, and at time 7.2 the margin passes over the string of tracers. Initially, the tracers passing over the margin seem to be more densely concentrated; however, this "hook" is quickly sheared out, as illustrated by following the group from 8.4 to 9.6. At time 8.4 the margin passes over a second string of tracers, and another fold forms. From time 9.6 to 13.2 this fold makes a complete circuit of the right cell; notice that during this time the clump of tracers seems to maintain its "intensity." In other words, the number of tracers in the "clump" seems to remain constant. Calculations have been made with margin amplitudes as small as 0.5 and with frequencies between 0.04 and 8. The formation of persistent folds exists throughout this parameter range and is clearly a general phenomenon.

These results can be made more explicit using the material line formulation. The case just studied (Figure 5.4) is recalculated by introducing two material lines at X(t) $\pm$ 0.025 and the material lines are closed at 2.4 transit times. The anomalous fluid is defined as the area within the material line and is blackened in Figure 5.5. The heterogeneity behaves as discussed above for the initially circular ones in that after a period of stirring (longer than the overturn time) the heterogeneity is defined by sizable blobs connected to long but thin tendrils (Figure 5.5). Comparison of Figure 5.5 with Figure 5.4 reveals that the clumps of tracers correspond with the sizable heterogeneities. At transit time 14.4 in Figure 5.5, the heterogeneity is defined by more than 2×10^4 tracers, but almost as much information was gained by following only 150 tracers as shown in Figure 5.4. However, the material line formulation explicitly reveals the size of the heterogeneity which is $\approx 0.5\theta_0$ (Figure 5.5). Limited computational resources only allowed the tracer formulation to be employed to study mixing in the thermal convection calculations.

The existence of folds caused by unmixing reveals that a large fraction of the heterogeneities, initially as sheets introduced on the margin of cells, are mixed by laminar shear. Such a result should not be surprising because of the unsteady nature of the flow: heterogeneities almost immediately migrate off of the zero streamline. The width of sheets is less than the scale of flow and the bulk of the heterogeneity resides within convection cells, such that sheets are primarily mixed by laminar flow. The use of periodic flows and analytic stream functions may be partly responsible for this behavior. This poses the question as to whether the blobs, caused by laminar shear and unmixing, will occur in thermal convective flows. This questions is now addressed.

5.3 Mixing in Thermal Convective Flows

For the first fully dynamic convection calculations presented, an important simplification has been adopted: the plate evolution models (i.e., velocity boundary conditions: $U^u(x,t)$ equation (4.37)) are cyclic in time; this simplification was only employed, as we shall see, to reduce the numerical computations. Nevertheless, both the kinematics of plate motion and the introduction of tracers below the implicit trench are still basic features of the calculation. In the following section, however, we will demonstrate that the major conclusions to be drawn are, in fact, independent of this simplification. The first six calculations, which employed cyclic boundary conditions (Table 1.1), display many common features and are best understood by considering the results of just one case (case P1) in detail. Moreover, the tracers were also sampled near the ridges in order to calculate the residence times; discussion of residence times is deferred to Chapter 9.

5.3.1 Plate Model and Fluid Flow

Case P1 has $R_Q = 10^5$, Pe=10^2, and internal heating. Plate model "a" (Figure 4.5a) forms the boundary condition. To provide a reproducible starting state, the margins were initially held stationary until the convecting region thermally reached an approximate steady state. In Figure 5.6 the details of this initial state are shown; on top, Q is the heat flux emerging from the top of the box and shows a maximum over the region of upwelling. In the box labeled T are the isotherms and show the thick thermal boundary layer on the top of the fluid and the isothermal interior of the upwelling region. The box labeled VEL is the imposed horizontal surface velocity (positive to the right), and STR are contours of the stream function. Next, the plate model (Figure 4.5a) was imposed on the convecting region. The calculation was cycled through the plate model three times. The temperature and velocity fields then no longer changed significantly from cycle to cycle. Convergence to a cyclic velocity field resulted in a large decrease in computation time because the same sequence of stream function arrays could be used successively to advect the tracers.

5.3.2 Qualitative Mixing Behavior

In Figure 5.7, eight instants in the mixing model are shown with the tracers plotted on the streamline fields. The values labeling each frame to the right are the total time and, in parentheses, the phase of the plate model of Figure 4.5a, both normalized by the transit time. The tracers are introduced below the triangles (see Figure 4.1), which locates the implicit trench. Initially, the tracers are positioned on the outer edge of the center cell, as shown at time 3. This pattern extends out to about time 5, whereupon, because the center plate is being consumed between a ridge and a trench, the center cell shrinks, while the right cell grows. This causes the tracers to be swept over to the right cell, as shown at time 6, when the ridge and trench have just coalesced. Notice at time 6 how the tracers are pinched between the right cell and the bottom of the box. At time 6 the plates rearrange, as shown in Figure 4.5a, and a new stationary ridge forms on the left and a new trench on the right. The situation at time 8 is shown after the new trench has migrated to the left; the tracers are progressively left behind as the trench migrates rapidly to the left as shown at times 8 and 10. The fold or clump of tracers forming on the bottom at time 6 can be followed as it swings around the right cell at times 8 and 10. This fold seems to maintain its intensity. Notice the formation of the broad fold interior to the first fold at time 8 and how it seems to diminish in intensity, at least from times 8 to 10, as it is sheared out. After time 10 (one cycle), no more tracers were introduced. The strings get torn apart as the flow goes through another cycle of plate evolution as shown at times 15 and 18. Nonetheless, there is a strong tendency for clumps of tracers to persist, as clearly seen at time 18, and there are even clumps at time 38. By time 58, however, no dense clumps can be recognized, although there is still considerable nonrandom heterogeneity evident in the distribution of tracers.

By focusing in on a group of tracers, we can determine the cause for the persistence of clumps. Shown in Figure 5.8 is a group of tracers that formed the kink at the bottom of the cell at time 6 (Figure 5.7). This group is followed from time 6 to 10, and the streamlines are the same as those in Figure 5.7. One tracer on the interior of the fold limb is marked with a circle; notice how this marker tracer passes from the interior fold limb (time 6) to the fold apex (time 8) and finally to the exterior limb (time 10) as the group of tracers moves around the convection cell. The fold apex seems to maintain its intensity as new tracers flux through it. The cause of this is simple: the angular velocity is greater toward the center of the convection cell, and this causes a particular tracer, interior to a second tracer, to approach the first tracer and then pass it. In other words, the heterogeneity is unmixed by the laminar flow within the interior of convection cells. The regions of unmixing occur about as frequently as they did in the analytically defined periodic flows studied above.

5.3.3 Other Periodic Plate Models

Four other cases were carried out with periodic plate evolution, like case P1 just described: cases P2 to P5, Table 1.1. Using both plate model "a" and also an additional model "b" of Figure 4.5b, the Pe was varied between 20 and 100, while $R_Q = 10^5$ in three cases (cases P2 - P4), while also employing internal heating. There were no significant differences in the way the tracers mixed, including the existence of folds, which persisted out to about 40 transit times, on average.

One of the model runs, case P5, had parameters more appropriate to the upper mantle convection scenario: $R_T = 2 \times 10^4$, Pe = 200, and bottom heating. Qualitatively, the mixing phenomena were essentially the same as the other model runs. This case may not be a very good analogue to upper mantle convection, because any "plate" in this model was never greater than 2 times the box depth, whereas the aspect ratio for upper mantle cells could be as large as 10, and this might limit the applicability of the model to the mantle.

5.3.4 Nonperiodic Plate Evolution Model

The flows just studied have a high degree of order, whereas from our understanding of plate kinematics, we may expect that the associated large-scale flow to have less regularity. The purpose of this section is to test this assumption by using pseudorandom velocity boundary conditions.

Case P6 has $R_Q = 10^5$ and Pe = 100; 650 tracers were introduced over the first three plate stages (13 transit times). We found that clumps of tracers persisted out to 40 transit times. This plate model was also employed for case P7 ($R_Q = 10^5$ and Pe = 50). The tracers were introduced over the entire 100 transit times. In Figure 5.9a, one instant is shown at time 43 when a ridge is migrating to the left toward a stationary trench, denoted by the triangle. For clarity, only the tracers introduced during the previous 11 transit times have been plotted. Notice two well-developed folds in the tracer strings: one in the center cell moving toward the region of upwelling under the ridge and the other in the downwelling limb of the right cell. The rightmost fold is shown in detail in Figures 5.9b-5.9d. Figure 5.9b is also at time 43 and is just an enlargement of a segment of Figure 5.9a. One tracer on the interior limb of the fold is marked with a circle. This group of tracers is followed through the unsteady flow from time 43 to 44 (Figure 5.9c) to 45 (Figure 5.9d). During this time, the marked tracer moves from the interior limb to the apex at time 44 and then moves out onto the outer limb of the fold; this clearly demonstrates that dynamic folds exist even in flows that are constrained by pseudo-random plate evolution.

5.4 Further Comparison with Other Studies

The conclusions reached here concerning the time scale over which spatial (or chemical) heterogeneity persists is contrary to the conclusions reached by Richter [1984] and Hoffman and McKenzie [1985]. As best I can judge, these different conclusions result not only from differences in interpretation and perspective, but also from differences in the form of the flows (especially in their degree of unsteadiness) and in the initial form of the chemical anomaly.

Richter [1984] and Hoffman and McKenzie [1985] emphasize the dispersion of anomalies and the mean properties of the stirring, with little regard to the details of spatial variations. Consider, for example, the last frames of Hoffman and McKenzie's Figures 12, 14, and 15. The authors emphasize how the initial square has become extremely contorted and that a large fraction of it has been drawn out into extremely fine streaks. Their figures clearly show this behavior. However, the authors fail to mention that much of the anomalous material is still in a few large blobs: a number of large chemical anomalies persist to 200-400 m.y. (the times they quote from upper mantle parameters). As shown quantitatively in section 5.1, measures of the "average" thickness of partially stirred heterogeneity clearly fails to bring out all the relevant information.

The models also differ in their degree of unsteadiness. To appreciate this difference, consider the isotherms of the flow shown in Figure 4 of Richter [1984]. Within the interior of this 8x1 box there are an average of four descending limbs for the instants shown. Using the parameter values he gives and his equation (2) relating the velocity scale to the Rayleigh number, the time interval between the instants shown is about two transit times. As best we can judge, there is complete (or nearly complete) rearrangement of descending flow in these two transit times. Richter et al. [1982] and Hoffman and McKenzie [1985] employed the same flow. In the flows studied here, however, a comparable amount of rearrangement would occur in about five transit times. Now consider the mixing resulting from this flow. The second frame in Figure 6 of Richter [1984] is rescaled to four to six transit times. The tracers in this figure are plotted in a similar way to our Figure 5.6; in terms of the clumping of tracers, we qualitatively judge this to be mixed as much as case P1 at 18 transit times. In terms of transit times, the flow Richter has used has a greater degree of unsteadiness and tends to mix anomalies more rapidly. The greater unsteadiness in those flows results from the relatively high Rayleigh number used in combination with constant viscosity and free-slip boundaries.

Finally, the apparent differences in persistence of heterogeneities depend upon the initial distribution of tracers. In steady flows, elements at the center of cells, for example, experience only minimal deformation. In the situation investigated by Olson et al. [1984a], where the flow is steady and the tracer distribution uniform, the stirring rate may be considerably smaller than the stirring rate for the unsteady flow investigated here, for example, because of the large proportion of tracers near the center of a cell. The placement of tracers either uniformly over cells or within the center of cells has no obvious relevance to known geological processes. Anomalies to be mixed by mantle convection enter at margins either from subduction or from entrainment of material from a boundary or adjacent layer.

Despite its lack of geological motivation, we have, for comparison, followed Richter et al. [1982], Richter [1984], and Hoffman and McKenzie [1985] and placed a uniform unit square of tracers in the center of the box at time zero for the flow of case P1 (shown in Figure 5.7). As shown in Figure 5.10a, the anomaly is efficiently stirred and dispersed by the flow and the longest surviving dense (small-scale) accumulation of tracers seems to persist, at most, to time 26. We now compare this with the case of tracer entry from the margin of a cell (case P1), except now all tracers are left in the flow. Because in the margin entry case the tracers were introduced over the first 10 transit times, we must use this case at time 31 so that the tracers have been in the flow for an average of 26 transit times. This instant is shown in Figure 5.10b. For both cases the tracers have been plotted in the same way. The margin entry case clearly shows much more intense spatial heterogeneity, especially on a small scale. When the tracers are introduced at the margins of convection cells, as opposed to instantly over a large patch, much more heterogeneity is observed to persist.

In summary, there are several reasons for the differences between the conclusions based on calculations presented here and those based on other calculations. The differences are mainly due to my emphasis of spatial heterogeneity as opposed to a mean mixing property, to the use of flows with less unsteadiness relative to average flow velocities, and to the use of chemical anomalies with different initial geometries.

Table 5.1

Summary of Mixing of Passive Tracers

Case	Plate model	Ra	Pe	μ	Number tracers
P1	a	10^5	100	1	250
P2	a	10^5	50	1	250
P3	b	10^5	100	1	200
P4	b	10^5	20	1	300
P5	a	$2x10^4$	200	0	200
P6	c	10^5	100	1	650
P7	c	10^5	50	1	400

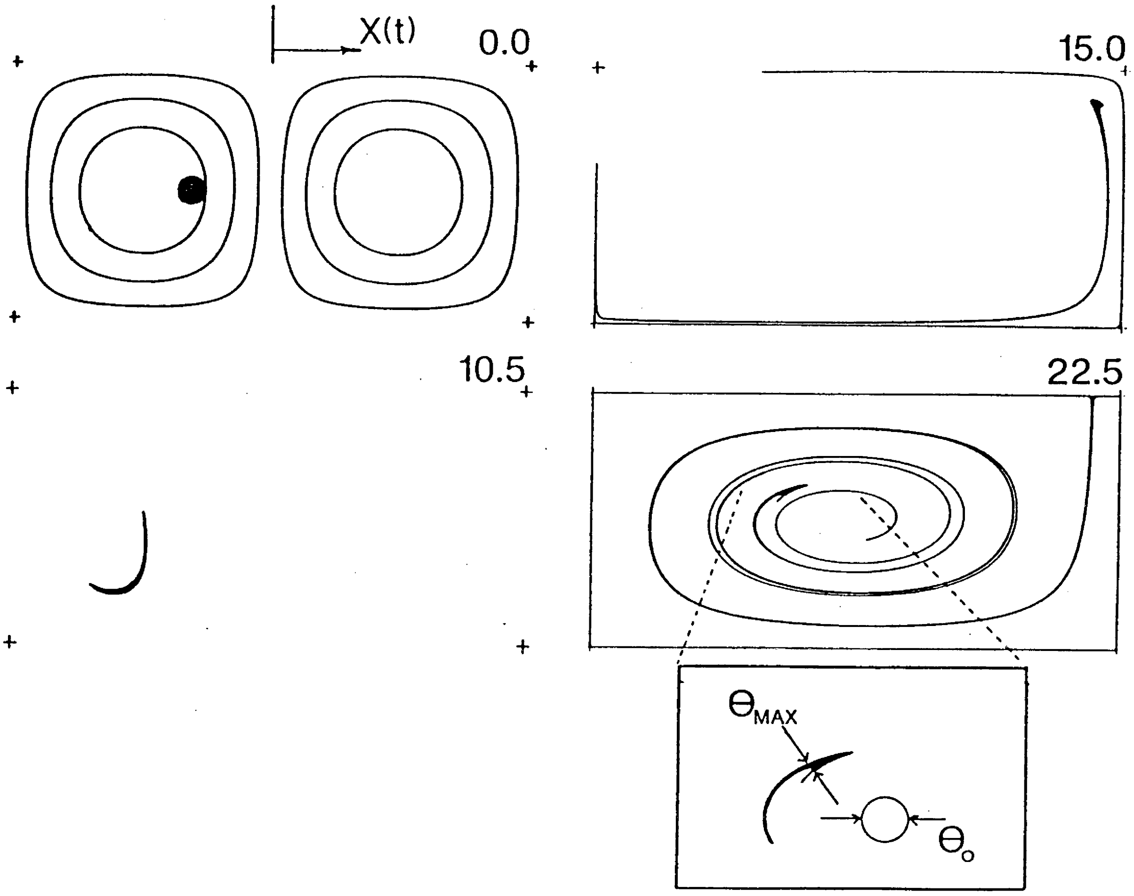

Fig. 5.1. Example of the stirring of an initially circular heterogeneity, black patch, in a periodic flow. The streamlines at time 0 are shown; the margin between the two cells oscillates as shown in Figure 5.4. Each frame is labelled with transit times. The inset highlights a large and persistent heterogeneity connected to very long, but thin tendrils. The maximum width, θ_{max}, is on the order of the initial size of the heterogeneity, θ_o.

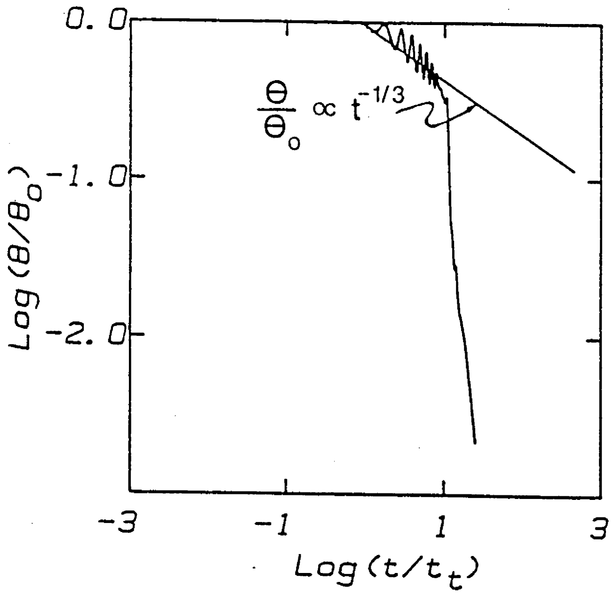

Fig. 5.2. Average width across the heterogeneity for the case shown in Figure 5.1 derived from the material line length, ℓ.

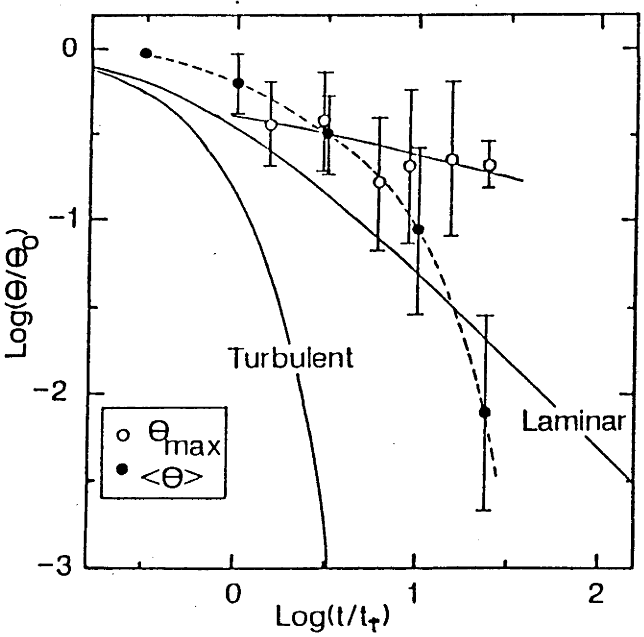

Fig. 5.3. Results of mixing calculations: the solid lines are the average width of the heterogeneity predicted by the simple laminar and turbulent mixing laws. The solid points are $\langle\theta\rangle/\theta_0$ derived from the total lengths of material lines. The open points are for θ_{max}/θ_0 and were derived as shown in Figure 5.1, inset; the curve passing through these points is defined in (5.1). The maximum sized heterogeneities mix slowly because they are laminarly mixed and occasionally unmixed within the interior of cells.

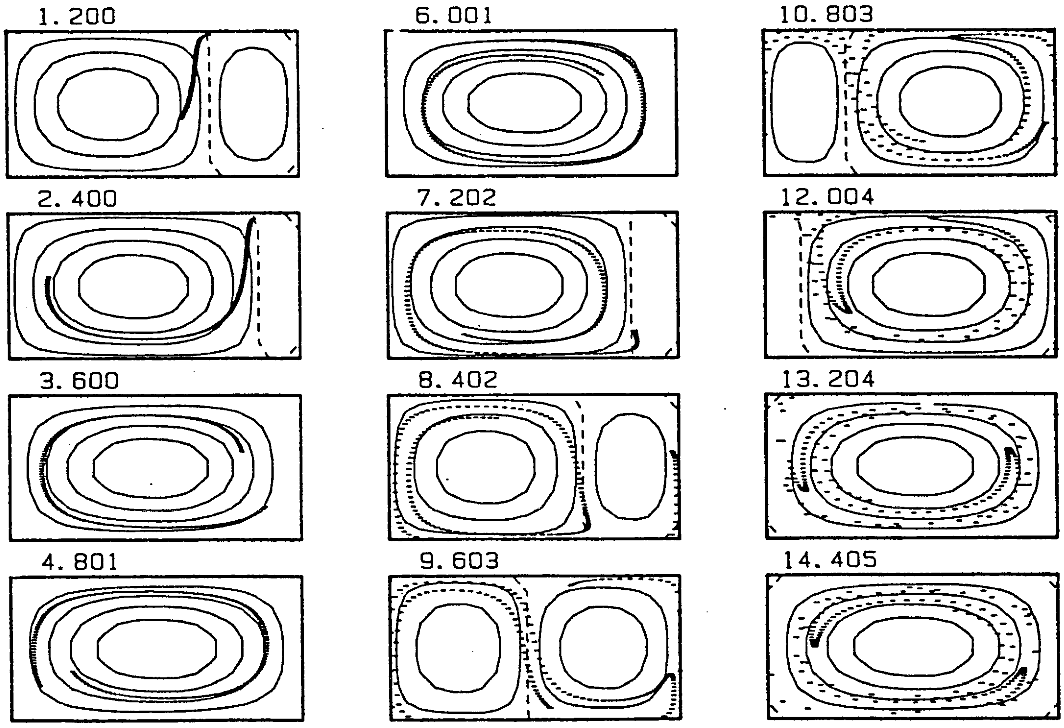

Fig. 5.4. Streamlines of the sinusoidal flows defined by (4.33) and tracers introduced on the margin between the two convection cells. E=1, Ω=1, and C=1. The values labeling each frame are the transit time.

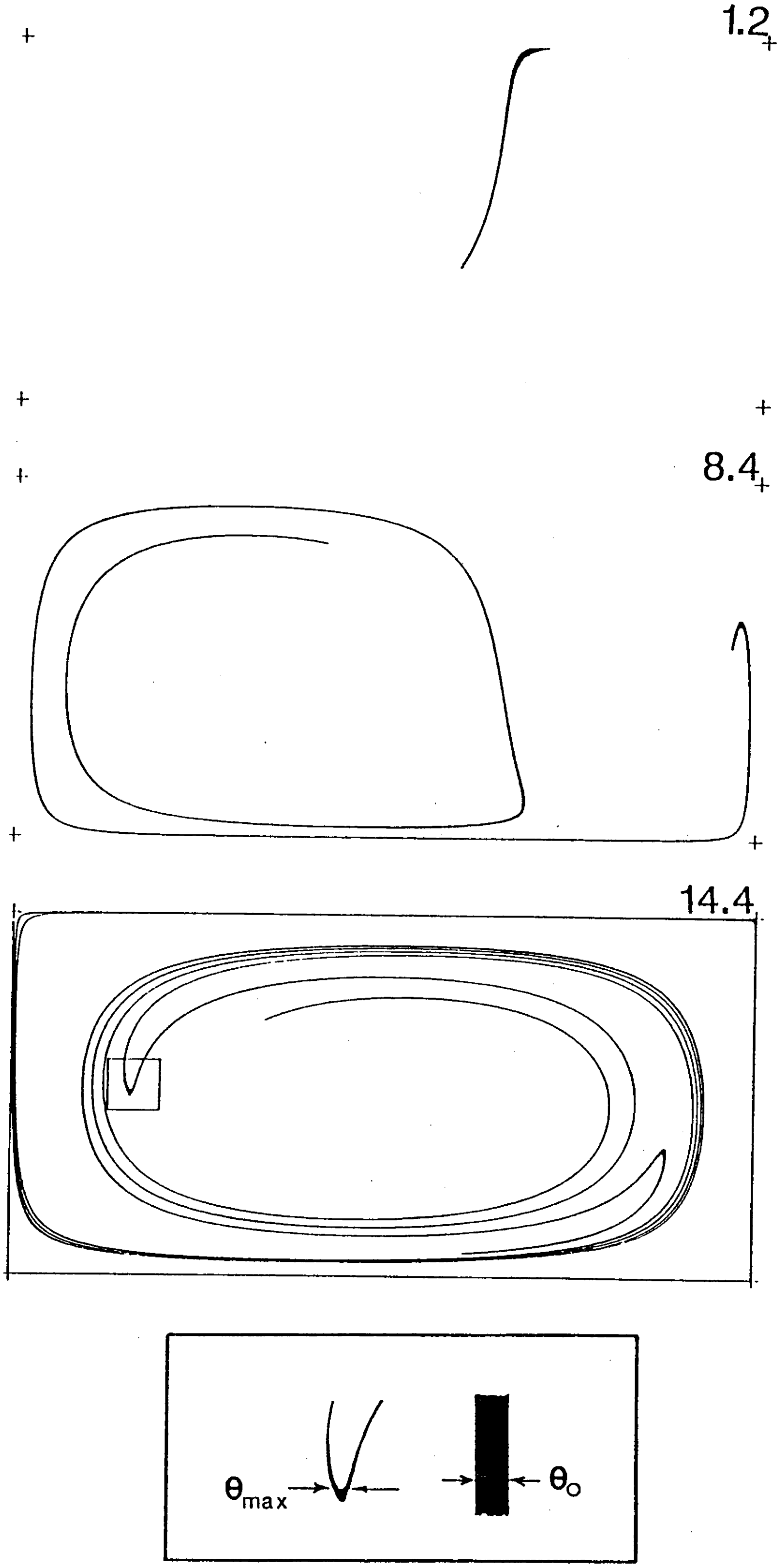

Fig. 5.5. Heterogeneity colored black using material line formulation for the case shown in Fig. 5.4 derived using tracer formulation.

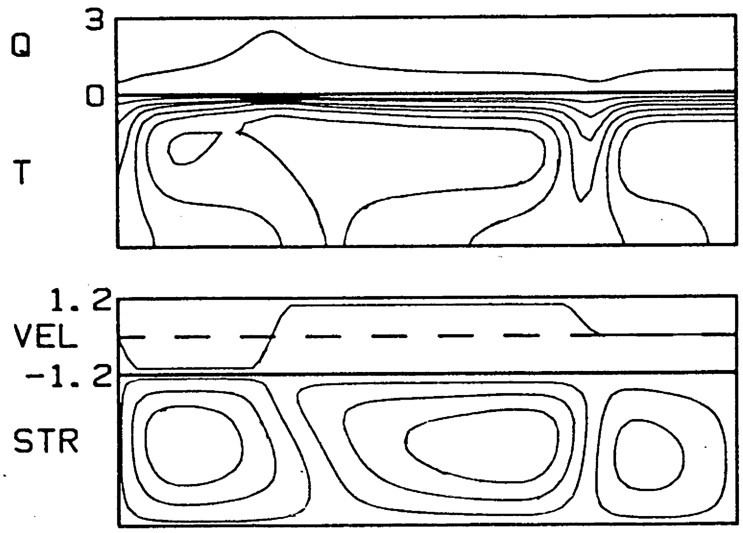

Fig. 5.6. Details of initial state of case P1 with $R_Q = 10^5$, Pe = 100 and internal heating. Quantities are the top heat flux (Q), temperature (T), top horizontal velocity (VEL, positive to the right), and stream function (STR).

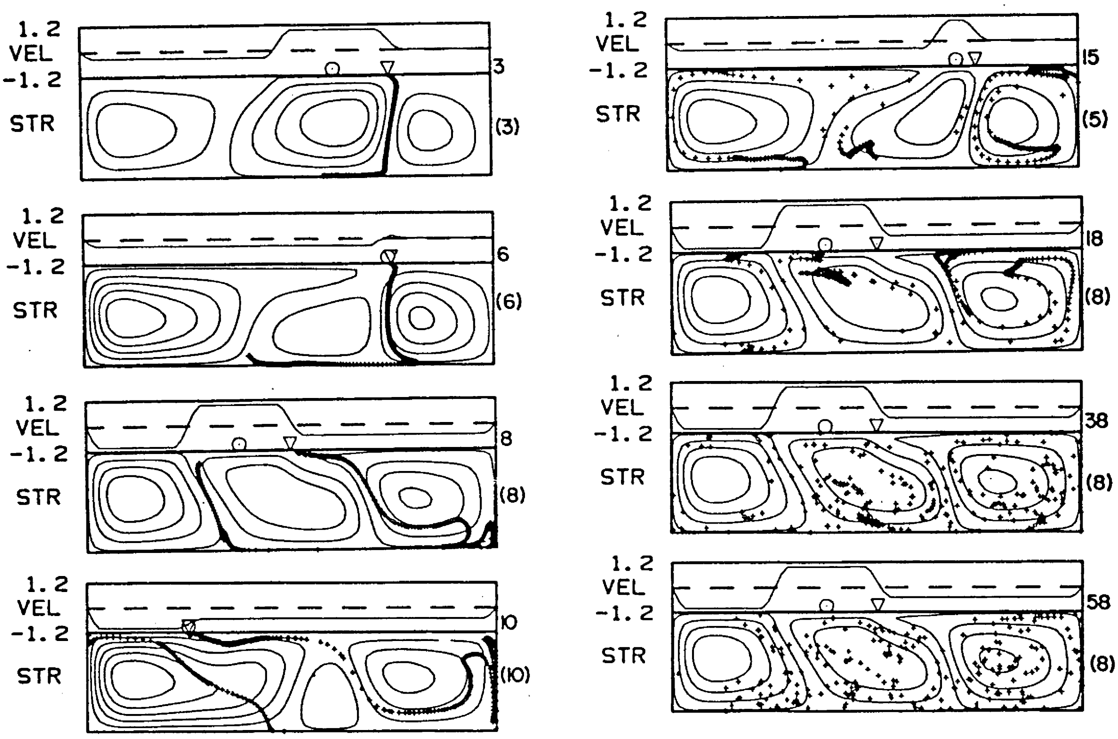

Fig. 5.7. Streamlines and tracer positions for case P1 at eight instants. On top of each box is the schematic of the velocity boundary condition. The circles, midway between the trench and ridge, denote the location of tracer sampling. The triangles denote the location of the implicit trench, where the tracers are injected into the flow. The values to the right of each frame are the total time, and in parentheses the phase in the plate evolution model (Figure 4.5a), both normalized by the transit time.

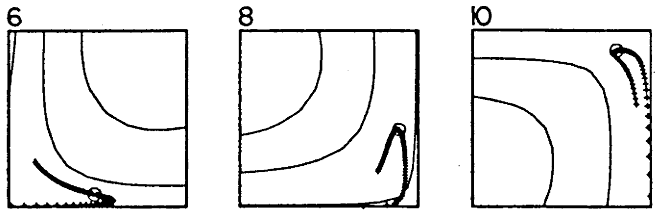

Fig. 5.8. Detail of a string of tracers making a circuit of the right convection cell in Figure 5.7. The times labeling each frame are the same as those in Figure 5.7 and so are the streamlines. One tracer has been marked with a circle, and this clearly demonstrates how tracers flux through the fold apex. This shearing of the string results in a persistent high-density concentration of passive tracers.

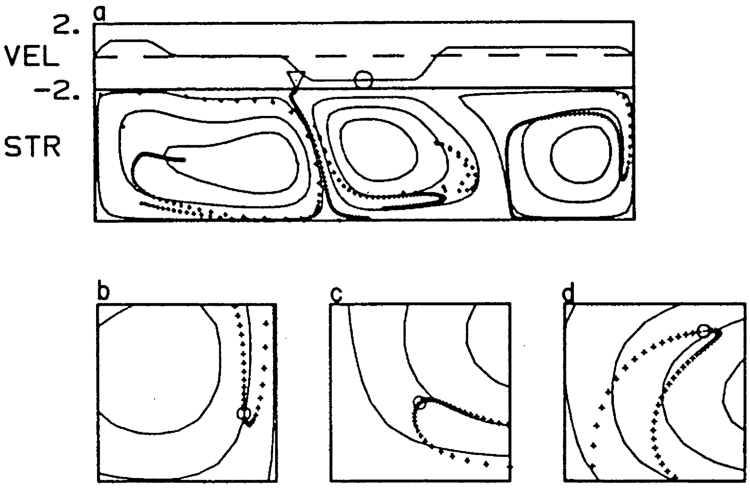

Fig. 5.9. Case P7 at transit time 43. The velocity boundary condition shows the location of a trench (triangle), which is stationary, and a ridge, which is migrating toward the left. The plate evolution model is pseudorandom in time. Only those tracers introduced during the previous 11 transit times have been plotted. The fold descending near the right side of the box is shown in detail in Figures 5.9b-d. One tracer is marked. This calculation clearly demonstrates that laminar unmixing of blobs is a robust feature of even models with pseudorandom plate evolution.

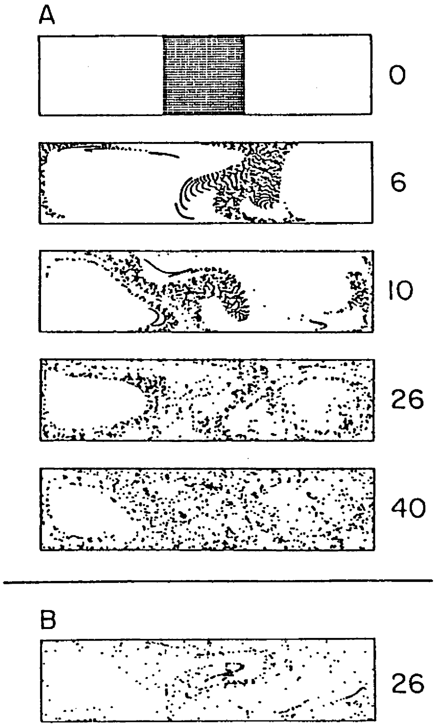

Fig. 5.10. Comparison of mixing when the mode of tracer introduction is varied. (a) Tracers introduced instantly in a unit square at t=0. (b) Tracers introduced at the margin of a cell. Values labeling each frame are the average time tracers have been in the flow (in transit times).

CHAPTER 6

CONVECTION AND MIXING IN FLUIDS WITH DEPTH-DEPENDENT VISCOSITY

6.1 Introduction

There is good evidence that the viscosity of the lower mantle is between 10 and 300 times greater than the viscosity of the upper mantle. Such an inference comes from many lines of evidence, as discussed in Chapter 2. A viscosity increase with depth through the mantle prolongs the survival and residence times of chemical heterogeneities [Davies, 1984]. In this chapter, the consequences of a high viscosity lower mantle are considered by investigating the stirring of passive heterogeneities in fluids with depth-dependent viscosity. Although, the results are given in non-dimensional transit times, they can be crudely scaled to whole-mantle convection by multiplying by 60 m.y. A range of scalings is made in Chapter 8.

As discussed by Richards and Hager [1986] the increase in mantle viscosity with depth is not uniquely constrained by geophysical observations. Neither is the average viscosity, weighted equally for all depths, uniquely known [cf. Nakada and Lambeck, 1986]. Consequently, since constraints on mantle viscosity from post-glacial rebound modeling are most likely somewhat biased toward upper mantle viscosity, the parameter in the models which is held constant is the viscosity at the very top, η_0, while the depth-dependence is varied. Other approaches are also valid, for example, the average viscosity could be held constant, while the form of depth-dependence is varied.

Moreover, in order to span the range of plausible viscosity distributions, two rather simple forms are used here (see also Chapter 4)

$$\eta(y) = 10^{\beta(1-y)} \qquad (6.1)$$

$$\eta(y) = \begin{cases} \eta_U & 1 \geq y \geq d/D \\ \eta_L & d/D > y \geq 0 \end{cases} \qquad (6.2)$$

Form (6.1) is motivated by the fact that the effective viscosity of silicates exponentially increases with hydrostatic pressure and hence exponentially with depth in a planet [eg. Weertman, 1970]. On the other hand, because substantial increases in viscosity could also occur across phase-transitions [Sammis et al., 1977] and phase transitions are concentrated in the depth range 400-670 km, the mantle could have a step-function viscosity distribution. Thus the layered form, (6.2), is also used for the simple cases presented here.

To set the stage for the mixing calculations presented in this chapter, the basic fluid dynamics of thermal convection in a fluid with an exponential increase in viscosity with depth is presented; this discussion is drawn from the more extensive work of Gurnis and Davies [1986]. This is followed by a discussion of the mixing of passive heterogeneities in unsteady flow, with a comparison of the effects which the two types of viscosity distributions have on flow structure.

6.2 Thermal Convection in a Free-Slip, Square Cavity

The effect which depth-dependent viscosity has on a convecting, internally heated fluid is explored. A square cavity is used and all the surfaces are stress free; the bottom heat flux is held constant. For comparison, the constant viscosity case with $R_Q = 5 \times 10^6$ is shown in Figure 6.1a. As is well known [cf. McKenzie et al., 1974], the fluid moves upward over a broad area and slowly warms; as it moves near to the surface heat is lost uniformly by conduction. The cold fluid rapidly descends on the right and the streamlines are centered toward this descending limb. The horizontal velocity, horizontally averaged at each level of the box (dashed line, bottom frame of Figure 6.1a), linearly varies with depth, but becomes approximately uniform with an $\langle U\rangle/\langle U_{TOP}\rangle \approx 0.5$ through the bottom third. The horizontally averaged temperature profile (solid line) shows the steep conductive gradient through the top and an approximately isothermal interior.

When a vertical viscosity gradient is introduced (Figure 6.1 b & c) the velocities in the lower section decrease. The center of the streamlines shifts upward and the stream lines become more horizontally centered. In the constant viscosity case the streamlines were approximately symmetrical about a line passing through at mid-depth. When $\beta = 1$ (Figure 6.1b), for example, the counter velocity is reduced and the horizontal velocity is approximately uniform over a larger depth range. There is still a steep velocity gradient (essentially linear) in the top half. When β is increased still further to 3 (Figure 6.1c), the largest counter velocities occur at mid-depth and the velocities become very small at the bottom, $\langle U_{BOT}\rangle/\langle U_{TOP}\rangle = 0.05$.

As the viscosity gradient increases the width of the thermal limb increases and the center of the streamlines and vorticity shifts away from where the descending limb originally was located. When β is increased the thermal structure becomes distorted, and the surface heat flux, which was constant across the top for constant viscosity, now decreases from ascending limb to descending limb. For a large β (β=3, Figure 6.1c), the largest horizontally averaged temperatures occur at the lower surface and a conductive thermal gradient is nearly approached as the bottom region approaches conductive stability. The thermal structure starts to resemble the top half of bottom heated convection: the top thermal boundary layer thickens with distance across the top and ascending and descending limbs become more equivalent in velocity and velocity gradients. The fluid slowly moves through the lower 2/3 of the box and warms, but now hot fluid emerges into the lower viscosity upper region and a narrower, faster moving upwelling region results.

6.3 Layered vs Exponential Viscosity Distributions

The decrease in velocity and strain rate depends on the form of the viscosity depth-dependence. In order to make comparisons between the exponential form (6.1) and the layered form (6.2), a consistent characterization of the increase in viscosity must be applied to these forms. Two types of characterizations are appropriate: (i) the average viscosity of the entire layer, normalized by the value at the upper surface ($\bar{\eta}/\eta_O$), and (ii) the ratio of the average viscosity of the lower "layer", $\bar{\eta}_L$, and the average viscosity of the upper "layer", $\bar{\eta}_U$ (e.g. $\bar{\eta}_L/\bar{\eta}_U$). The second characterization is motivated by recent estimates of mantle viscosity which have been made in terms of $\bar{\eta}_L/\bar{\eta}_U$ [Hager, 1984; Richards and Hager, 1986]. For the present discussion, the means are given in terms of the geometrical mean,

$$\ln \bar{\eta} = \frac{1}{D} \int_0^D \ln \eta(y)\, dy \qquad (6.3)$$

for the average of the entire layer. In order to determine $\bar{\eta}_L/\bar{\eta}_U$ for the exponential distribution (6.1), an imaginary boundary is placed at a depth d/D and the average is taken over each layer separated by this boundary.

The two forms of the viscosity depth-dependence lead to important differences in flow structure and hence in the way the flows mix heterogeneities. Comparisons have been made between exponential and layered cases with the same R_Q and Pe (Table 6.1). For illustration, two cases are discussed in detail here. The exponential case, D9, has an average viscosity, $\bar{\eta}/\eta_O$, twice as large as the layered case, D10, but the viscosity ratio, $\bar{\eta}_L/\bar{\eta}_U$, of the exponential case is only half as large (56 compared to 100). The initial steady states for these two cases are shown in Figure 6.2. The most important difference between the two of them is the much stronger confinement of flow near the upper-parts for the exponential case (D9, Figure 6.2a) compared to the layered case (D10, Figure 6.2b), despite the fact that $\bar{\eta}_L/\bar{\eta}_U$ is twice as large in the layered case. The layered case shows a sudden decrease in velocity at a depth d/D (as indicated by the sharp kinks in the stream lines, Figure 6.2b).

In Figure 6.3 vertical profiles of horizontally averaged quantities are plotted along with the constant viscosity case with the same R_Q and Pe. The most relevant difference for mixing, shows up in the quantity $\langle\dot{\varepsilon}\rangle$, the rms of the second invariant of the strain rate at each horizontal layer: the layered case has an approximately uniform shear through the lower layer while the exponential case shows a continuous reduction in shear, with about an order of magnitude lower shear through the bottom 1/4 of the box. The smaller shear at the base occurs for the case with the smaller $\bar{\eta}_L/\bar{\eta}_U$. These differences in the shear strain rate indicate that important differences will be found between the layered and exponential viscosity cases.

6.4 Mixing in Unsteady Flows

In order to understand how passive heterogeneities are mixed by these flows, mixing calculations have been carried out. Flow unsteadiness is constrained by unsteady velocity boundary conditions and tracers are introduced at converging margins. The stirring of passive tracers introduced below "trenches" (converging plate margins) shows both some similarities as well as some differences in comparison with the constant viscosity cases.

The stirring of tracers introduced below the trench for two exponential cases is shown in Figure 6.4: case D4 with $\beta = 2$ (a) and case D9 with $\beta = 3.5$ (b). In all cases (Table 6.1), the unsteady, pseudo-random plate model "c", described in section 4.5.2 was imposed on the top of the cavity as a velocity boundary condition. The constant viscosity case using this same plate model was considered in section 5.3.4. The tracers, introduced at a margin, initially form strings which are locally parallel to the stream lines, but later, because the flow is unsteady some strings remain parallel while others are at odd angles to the stream lines (Figure 6.4a, transit time 13). This leads to both the ripping apart of some tracer strings and to partial unmixing of other strings, as found for the constant viscosity flows. The most important difference with the constant viscosity flows, however, is that tracers are only slowly advected into the lower parts of the box; for example, not until about transit time 29 (Figure 6.4a) are the recycled tracers stirred into the basal regions. By contrast, it only takes a few transit times for tracers to reach the base in constant viscosity flows (c.f. Figure 5.7). Moreover, clumps of tracers persist for as long as 100 transit times when $\beta = 2$ compared to about 40 transit times for the constant viscosity flows (Chapter 5).

Case D4 shows the added feature of "storage": recycled tracers are subducted and advected to the base. In particular, notice the strings of tracers on the left and along the base at transit time 29; these tracers remain near this position for about 20 transit times (time 56, Figure 6.4a), but because of flow unsteadiness (caused by plate rearrangement) these stored tracers are then rapidly entrained into the upper parts of the flow, as shown at time 62. This feature obviously has relevance to geochemical models of oceanic crust which later appears as OIB.

Case D4 (β = 2) contrasts with case D9 (β = 3.5, shown in Figure 6.4b), primarily because tracers take about twice as long to be entrained into the lower parts of the flow for the higher viscosity case. However, by the time tracers are entrained into the basal regions (time 116, Figure 6.4b) clumps of tracers no longer survive. In addition, by the time of basal entrainment, the total number of tracers has been reduced considerably because of ridge sampling (see Chapter 9). Despite the fact that $\bar{\eta}/\eta_0$ increases from 10 to 56 between cases D4 and D9, the survival time for spatial heterogeneity apparently has not significantly increased; this may be caused by the shearing of recycled material in the upper parts of the flow by plate rearrangement before the tracers have time to be advected into the lower parts of the flow.

An important question to pose is how long the deeper portions of the fluid can remain isolated from the surface and thus from ridge sampling. This question is addressed by introducing a layer of uniformly spaced tracers of depth 0.2 at the base of the cavity. Some instants in the evolution of tracer positions are shown for three cases in Figure 6.5; labelling each frame is the transit time. In the constant viscosity case, D1 (Figure 6.5a), the basal tracers are stirred about the box in about 10 transit times, with most spatial heterogeneity persisting; by 20 transit times the tracers have been dispersed considerably and only some of the initial heterogeneity persists. When a viscosity gradient is introduced, for example β = 2.5 (D5, Figure 6.5b), the basal tracers take about 30 transit times to be entrained into the upper parts of the flow, compared to only about two transit times for β = 0. In the β = 3.5 case (D9; Figure 6.5c) tracers were entrained into the top parts of the flow by 50 transit times. Large, relatively unstrained regions of basal tracers can remain at the base of the convecting region for about one transit time when $\beta = 0$, but for $\beta = 2.5$ such regions persist for as long as 100 transit times and for $\beta = 3.5$ for 150 transit times.

These long survival times for basal tracers are dependent on the form of viscosity depth-dependence. In Figure 6.6 basal tracers (in red) and recycled tracers (in green) are shown for case D10 with a layered viscosity distribution, $\bar{\eta}_L/\bar{\eta}_U = 100$. The basal tracers are completely swept off of the base after about 40 transit times. However, for an exponential distribution with an $\bar{\eta}_L/\bar{\eta}_U$ of only 56 (D9) basal tracers persist three times longer (up to 150 transit times). Figure 6.6 also shows that the recycled tracers are stirred into the deeper regions in about 40 transit times.

For both basal and recycled tracers spatial heterogeneity qualitatively persists for twice as long for exponential case D9 ($\bar{\eta}/\eta_o = 56.2$) compared to layered case D10 ($\bar{\eta}/\eta_o = 20.9$), while $\bar{\eta}_L/\bar{\eta}_U$ is twice as large for the layered case compared to the exponential case.

Table 6.1

Summary of Mixing Calculations with Depth-Dependent Viscosity

Case	R_Q	Pe	Type[#]	β	$\bar{\eta}/\eta_0$	$\bar{\eta}_L/\bar{\eta}_U$
D1*	10^5	10^2	C	0	1	1
D2	10^5	10^2	L	-	4.6	10
D3	10^5	10^2	E	1	3.2	3.2
D4	10^5	10^2	E	2	10	10
D5	10^5	10^2	E	2.5	17.8	17.8
D6	5×10^6	350	C	0	1	1
D7	5×10^6	350	L	-	20.9	100
D8	5×10^6	700	C	0	1	1
D9	5×10^6	700	E	3.5	56.2	56.2
D10	5×10^6	700	L	-	20.9	100

* Same as case P6.

[#] Type of viscosity distribution: C=Constant; E=Exponential; L=Layered

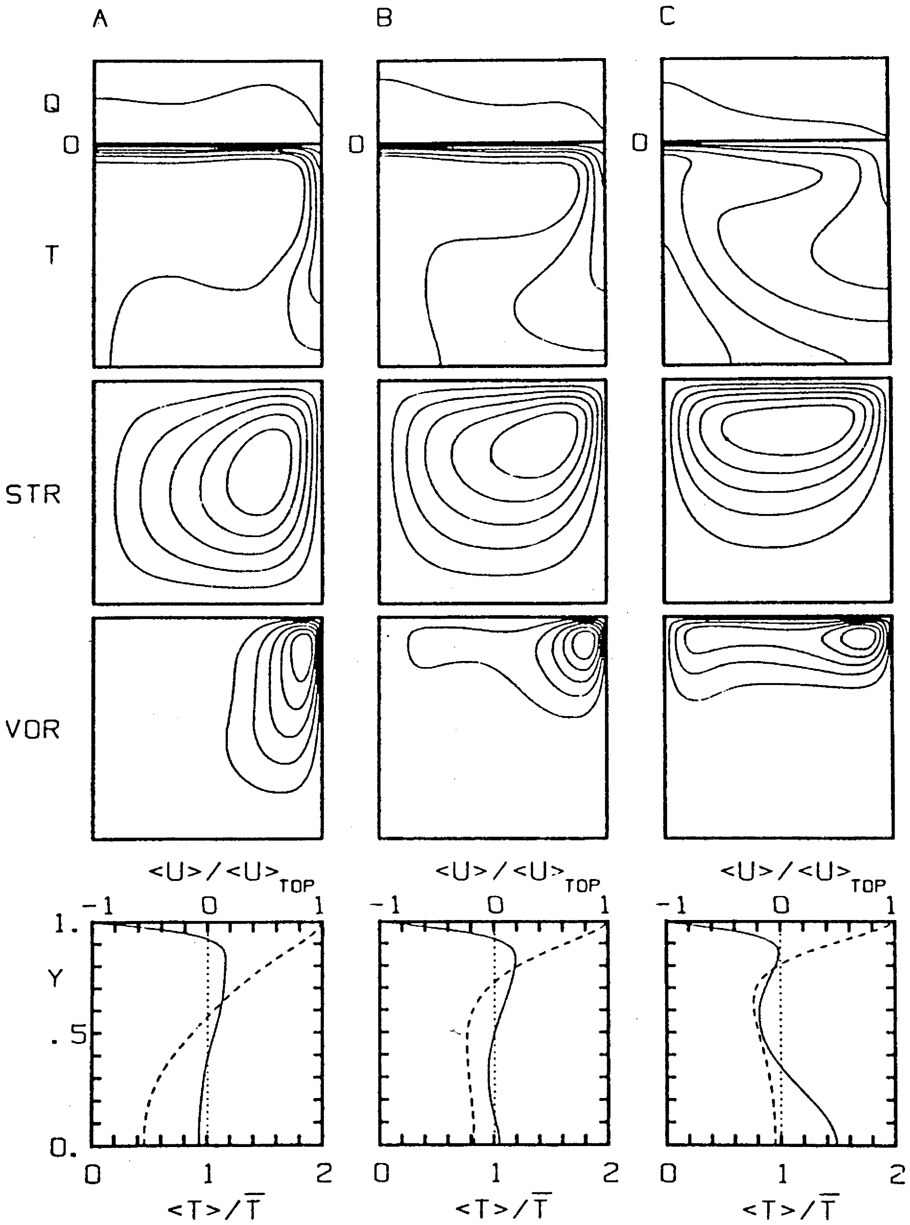

Fig. 6.1. Thermal convection in a square cavity with all sides free slip. The flows are driven by internally generated heat. For each case, 63x63 internal mesh points were used. T is temperature, STR is the stream function, VOR is the vorticity and in the lower box the solid lines are temperature and the dashed lines are horizontal velocity. A. Constant viscosity, B. exponential depth-dependent viscosity with $\beta = 2$, and C. $\beta = 3.5$. A more complete discussion of these models can be found in Gurnis and Davies [1986].

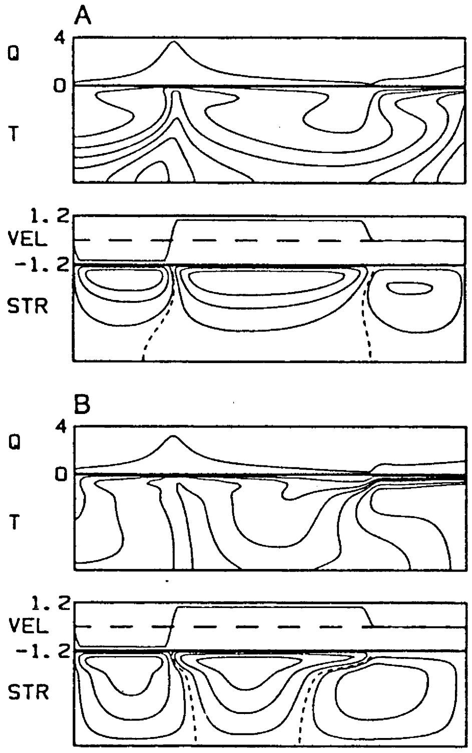

Fig. 6.2. Steady-state thermal convection in a 4x1 box with an imposed, steady velocity boundary condition. A. Exponential increase in viscosity with $\beta=3.5$ (case D9). B. Layered viscosity distribution with η_L/η_U = 100 (case D10). For both cases, 31x127 internal mesh points were used. The viscosity profiles are shown in Figure 6.3.

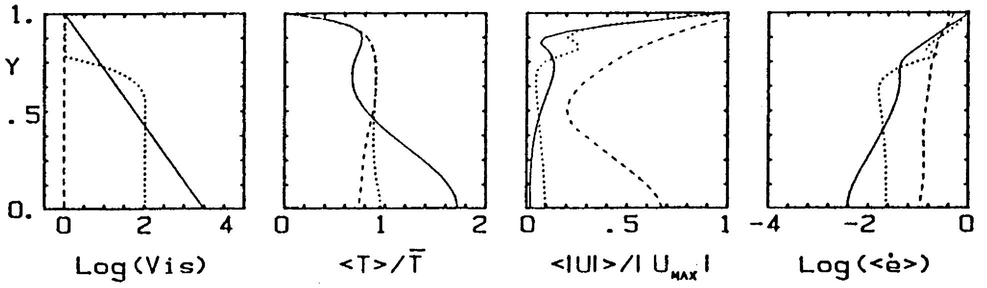

Fig. 6.3. Depth profiles of viscosity, temperature, velocity, and strain rate for three cases: dashed line, constant viscosity case D8; solid line, exponential viscosity case D9; and dotted line layered viscosity case D10.

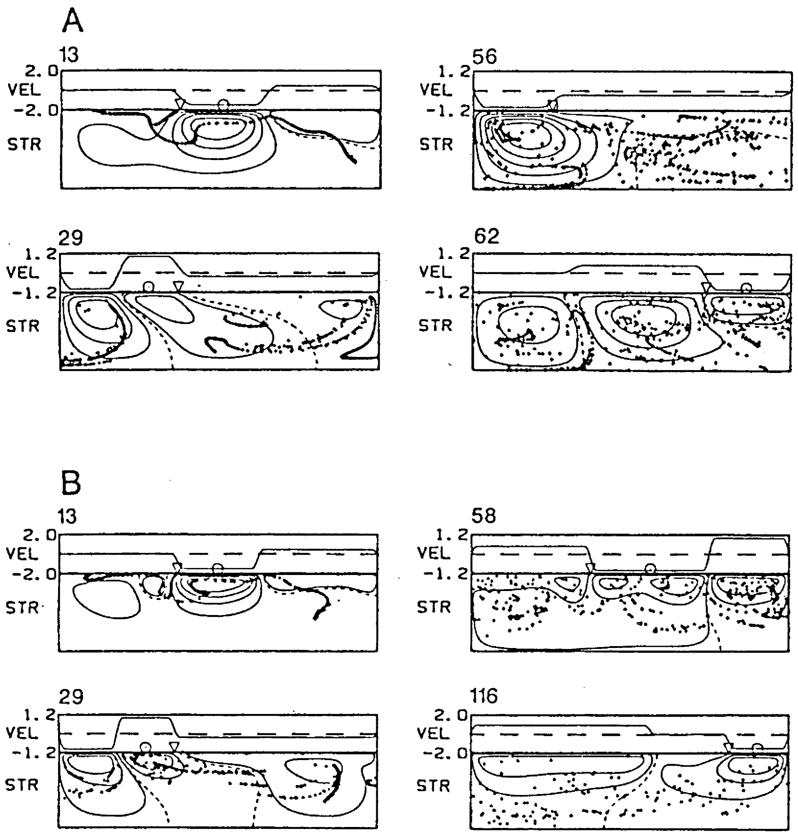

Fig. 6.4. Stirring of Passive, recycled tracers in convection models with exponential depth-dependent viscosity distributions. The time labelling each frame is in transit times. A. case D4 with $\beta = 2$, and B. case D9 with $\beta = 3.5$.

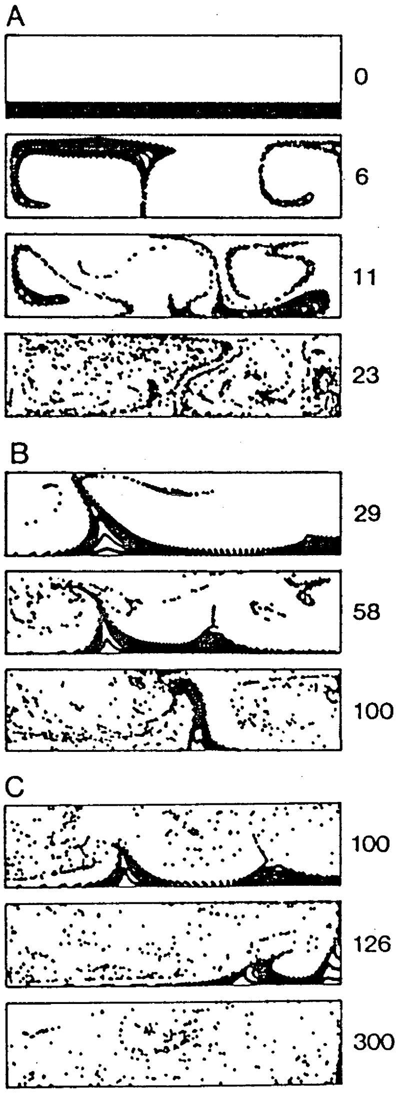

Fig. 6.5. Position of basal tracers for three cases: (a) Case D1 (β=0), (b) case D5 (β=2.5), and (c) case D9 (β=3.5). The values off to the right are transit times since the tracers were introduced into the flow.

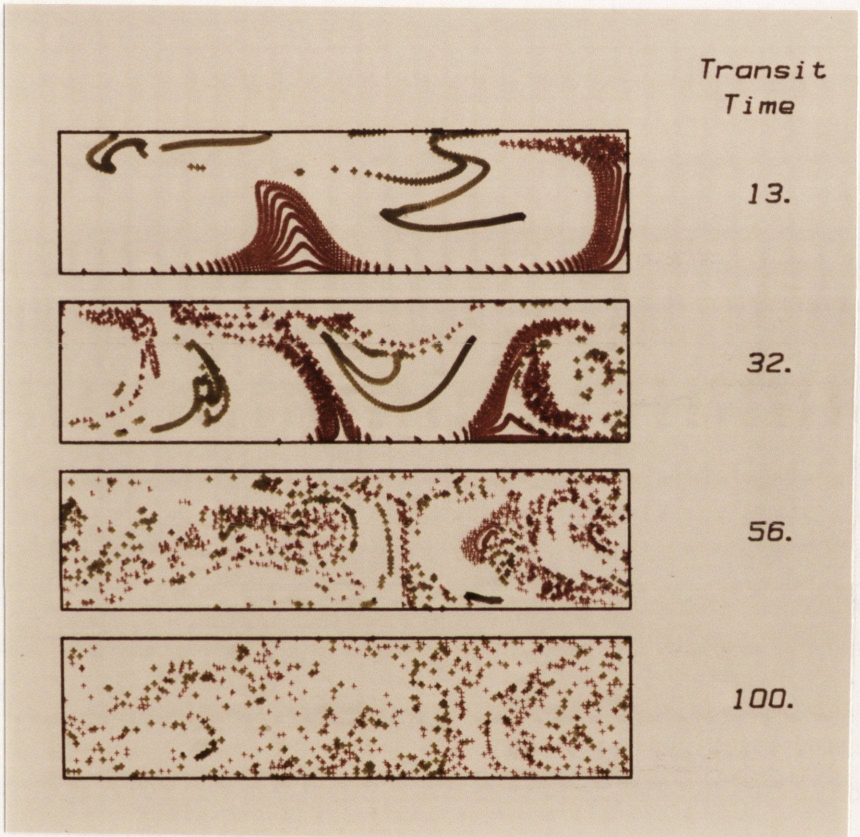

Fig. 6.6. Stirring of recycled tracers (in green) and basal tracers (in red) for case D10 with a layered viscosity distribution (η_L/η_U = 100).

CHAPTER 7

MIXING OF INTRINSICALLY DENSE MATERIAL IN CONVECTIVE FLOWS

Some investigators have hypothesized that because subducting lithosphere is chemically distinct from ambient mantle, and hence may have different intrinsic density, it preferentially segregates to particular zones or layers within the mantle and that this process maintains chemical heterogeneity within the mantle for billions of years [Anderson, 1982; Hofmann and White, 1982; Ringwood, 1982]. For example, Hofmann and White [1982] hypothesize that because subducting oceanic crust transforms to eclogite, which is intrinsically more dense than ambient mantle, it separates from the lower lithosphere, sinks to the core-mantle boundary (CMB) and forms a layer on a time scale of hundreds of millions to billions of years. The purpose of this chapter is to evaluate the general physical processes envisaged in such hypotheses with simplified computations; it is hoped that the calculations will shed light onto the viability of some models and eliminated those models incapable of segregating in the ways assumed.

The hypotheses advanced by Anderson [1982], Hofmann and White [1982], and Ringwood [1982] fail to consider the likely effects of large-scale mantle flow. This should not so much be seen as a criticism of these modeling efforts, but rather as indicating a gap in our understanding of how chemical and thermal buoyancy interact. The problem addressed can be expressed simply as: are the buoyancy forces caused by intrinsic density large enough to offset locally the thermal buoyancy forces which drive the large-scale flow and therefore have an appreciable effect on mantle dynamics and evolution?

7.1 Simple Stokes Velocity Calculations

The purpose of this section is to outline, with simple calculations, the sizes and intrinsic densities needed to achieve velocities comparable with lithospheric velocities. In this section, a spherical heterogeneity of radius, a, density, ρ_s, and dynamic viscosity, η_s, is considered. The terminal velocity, with Reynolds number much less than unity, is [Batchelor 1967]

$$U_s = \frac{1}{3}\ \frac{a^2\, g\, f_m}{\nu_o}\ \frac{\rho_s - \rho_o}{\rho_o}\ \Upsilon(\eta) \qquad (7.1)$$

$$\Upsilon(\eta) = \frac{\eta_o + \eta_s}{\eta_o + \frac{3}{2}\eta_s} \qquad (7.1)$$

where ρ_o and η_o are the density and dynamic viscosity of the ambient mantle ($\nu_o = \eta_o/\rho_o$ is the kinematic viscosity). f_m is the mixing fraction and denotes the fraction of chemically anomalous material (with ρ_s) mixed through the volume of radius a. For the case of a heterogeneity within the mantle, we would expect $\eta_o \approx \eta_s$ and thus $\Upsilon(\eta) = 4/5$.

The first point which will be demonstrated is that the velocities of small (~ 10 km) sized heterogeneities are much smaller than average plate velocities (~ 5 cm/yr) unless unrealistically large intrinsic densities are assumed. The high pressure mineral assemblage with the largest $\Delta\rho$ (through the upper mantle) is eclogite and, at most, has a value of 200 kg m^{-3} [Anderson, 1979; Ringwood, 1975, 1982]. It seems unlikely that $\Delta\rho$ could be much larger than this anywhere in the mantle. As will become clear, the ambient mantle viscosity is a principal quantity affecting the velocities. There seemed to have been consensus that the effective (newtonian) viscosity was approximately uniform throughout the mantle and with a value of about 10^{21} Pa-s [Cathles, 1975; Peltier, 1983]. However, within the last few years, new evidence suggests that the viscosity may be even larger in the lower mantle (perhaps by a factor of 10 or more, see Chapter 2).

In Figure 7.1, the $\Delta\rho$ required for a sphere of radius a to achieve a velocity of 5 cm/yr is plotted. For example, a sphere of radius 75 km would need an excess density of at least 100 kg m^{-3} throughout, for it to achieve a velocity of 5 cm/yr. This clearly demonstrates that small heterogeneities cannot move at plate velocities through a fluid of $\eta_o = 10^{21}$ Pa-s without assuming unrealistically large intrinsic densities. Small heterogeneities could move at plate velocities if η_o was low enough, as is shown by the curve for $\eta_o = 10^{19}$ Pa-s, (the value assumed by Anderson [1982]), but from the references cited, this viscosity must be considered as unrealistically low.

In Figure 7.2, Stokes velocities are plotted as a function of radius, a, and mixing fraction, f_m, when $\Delta\rho = 200$ kg m^{-3}. This plot clearly shows that large-scale regions with reasonable volumes of ambient mantle and with "anomalously" dense material mixed through, could reach velocities approaching lithospheric plates. For example, a volume of 500 km radius and with 1 percent eclogite coarsely mixed through it can move at 4 cm/yr. This volume of eclogite is produced in less than 1/2 m.y. (million years), globally, assuming an areal rate of plate subduction of 3 km^2/yr [Chase, 1972] and an oceanic crustal depth of 6 km.

In certain parts of the flow convective velocities may be less than the average velocity used for these calculations and more segregation could take place than is indicated here. For example, near the lower boundary, vertical convective velocities could be smaller than the Stokes velocities of small chemical blobs.

These simple calculations suggest how the more intensive numerical models should be set up, on the one hand, and the type of phenomena which could be expected, on the other. Intrinsic density (with realistic ρ_s) can only give rise to appreciable velocities if the anomaly exists over a fairly large length scale (hundreds of kilometers). In terms of the numerical calculations, this means we can use a fairly coarse grid without loss of resolution of important mixing phenomena. We need only look for mixing phenomena which tend to concentrate the tracers over a fairly large volume.

7.2 Steady Plate Kinematics

In the first cases considered the plates are maintained in a steady configuration; although this has only marginal geological relevance, it illustrates basic mixing phenomena well. For simplicity the tracers are introduced only over the first 10 transit times of the model run. In Figure 7.3 the case with passive (A_Q=0) tracers after 10 transit times is shown. The cases have been summarized in Table 7.1, where plate model "s" denotes the steady-plate evolution model.

When the tracers are passive (A_Q = 0, Figure 7.3) they are simply advected by the flow. The tracers are placed beneath the trench and are on the edge of the center cell where they remain; all are sampled near the ridge. When the tracers become negatively buoyant, however, they effect the flow as shown in Figure 7.4a (A_Q = 2). The tracers are again successively introduced at the edge of the center cell during the first ten transit times, but when the tracers emerge from the bottom and start their ascent into the warm upwelling region, they slow and form a region of high spatial density; the heavy tracers neutralize the warm buoyant fluid. The streamlines are deflected from this neutralized region and indicate that the flow velocities are reduced considerably there. By time 20, in Figure 7.4b, the chemically anomalous region has settled into a quasi steady structure; tracers are being swept back into the flow, but only at a small rate.

This behavior is dependent on the heating mode which is varied from internal heating (μ=1, Figure 7.4a & 7.4b) to entirely bottom heating (μ =0, Figure 7.4c & 7.4d). With bottom heating, the tracers fail to disrupt the flow significantly, even when the density anomaly ratio, A_Q, = 2. There is a moderate amount of clumping at the base of the rising limb on the right; but the tracer clumping is of less significance than in the internally heated case. The tracers cannot easily neutralize the strongly buoyant (hot) thermal boundary layer along the bottom and remain closely positioned around the margins of the cells. The tracers are easily swept along by the "thermal" convection.

7.3 Unsteady Plate Kinematics

In order to elucidate the effects of unsteady large-scale flow, case H6, with A_Q = 2, will be considered in detail. The plate model, a, in Table 7.1, is shown in Figure 4.5 and was discussed in section 4.5.2. In Figure 7.5 the first frame (transit time 3) is before the ridge and trench coalesce. Because the trench remains approximately stationary with respect to the margin of the cells, the tracers are consecutively positioned around the margin of the center cell up to about t=5. Frame b at time 8 shows tracers being placed below the "trench" as it migrates toward the left. Near the bottom of the warm upwelling region the tracers form a high density patch, similar to the one which formed with the steady plates (Figure 7.4a); this region tends to persist to about 50 transit times. A similar phenomenon occurs under the upwelling region on the right and the clumped tracers tend to persist there for more than 100 transit times (frame f of Figure 7.5 is at t=98). The position of the clumps of tracers is due to the neutralization of the thermal buoyancy by the negatively buoyant tracers. Only a small fraction of the tracers is actually resting on the bottom and many are actually "floating" a small distance from the bottom. However, the continued rearrangement of the surface plates, which causes the large scale convection cells to grow and shrink, tends to continuously erode tracers off the sides of the chemically anomalous regions. The neutrally buoyant regions dissipate. The right anomaly persists longer than the central anomaly and is due to the spatial persistence of the warm upwelling region on the right.

The effect of heating mode is explored with Case H13 where the flow is driven by heat entering through the bottom, but A_Q = 2 as was case H6, just described. The most striking difference between case H6 and this one is the lack of large diffuse regions of tracers near the bottom. Tracers did tend to preferentially clump near the base of the uprising limbs, as in the steady case. This case confirms the results from the steady plate cases described above: neutralization of buoyancy occurs at a higher A_Q for bottom heating as opposed to internal heating when the total heat remains constant.

The use of periodic plate models is potentially a significant approximation. When the tracers are passive, periodic plate evolution produced no spurious effects on mixing, Chapter 5. To test the effect of the periodic plate model, the same pseudo-random model described in section 4.5.2 has been employed. Qualitatively, the fluid phenomena displayed by Case H17 are essentially the same as in Case H6 (Figure 7.5), but now the warm regions of upwelling are more mobile (because of the greater degree of plate rearrangement) and the diffuse regions of heavy tracers tend to waft back and forth across the bottom.

7.4 Continuous Introduction of Tracers

In the final set of calculations, the tracers are introduced throughout the model run instead of the first 10 transit times. This was done to explore the interaction between newly introduced tracers and "older" tracers, on the one hand, and to approximately determine the value of A_Q for which layering sets in, on the other.

The tracers are introduced throughout the model run when the plates are steady in cases C1 and C2, Table 7.2. For the internally heated case (C1) there is no change from case H2 when the tracers were introduced over the first 10 transit times. But for the bottom heated case (C2) tracers accumulate and neutralize the buoyancy near the bottom of the hot limbs. However, the neutralized regions apparently become hotter more rapidly than tracers are added, and the stagnant regions eventually become thermally unstable and break up. This time-dependent phenomenon did not occur when $\mu = 1$. Furthermore, this behavior is unique to the steady-state plate cases and did not occur when there was plate rearrangement (case C7). In Figure 7.6, two cases with internal heating after 61 transit times are shown; case C5 has $A_Q = 2$ and C6 has $A_Q = 6$. The transition from regions of neutralized buoyancy beneath warm upwelling regions to clearly defined chemical layering is rather indistinct. In the case of $A_Q = 2$ there is a higher proportion of tracers through the bottom 1/4 of the box, but the distribution is not smooth, as there is a lack of tracers at the base of the downwelling regions. Increasing A_Q to 6, the bottom half starts to developing convection cells distinct from the cells defining the top surface motions. There is a distinct lack of tracers in the top two-thirds, but there is still no sharp boundary between convecting layers as defined by the tracers. True two layer convection will not form until even higher A_Q.

7.5 Scaling Density Anomaly Ratios to Mantle Conditions

7.5.1 Mathematical Details of Scaling Relationships

In this chapter, various types of segregation phenomena have been documented, but will such phenomena occur in the mantle? This cannot be easily addressed with the results presented so far because the calculations were done at $R_Q = 10^5$ and the whole-mantle has a $R_Q \sim 10^9$; the A_Q must be scaled to higher values of R_Q.

The dependence of A_T on R_T can be deduced, heuristically, from boundary layer theory scalings between the heat flux, temperature, and velocity and the Rayleigh number (c.f. Turcotte and Oxburgh [1967] or Turcotte and Schubert [1982]). The relation between A_T and R_T can then be converted to a dependence of A_Q on R_Q. These scaling relations are then tested by observing the A_Q when tracers first fall out of the flow (or neutralize the thermal buoyancy) as a function of R_Q. The transition values will be denoted in this section as A'_Q and A'_T. In this section the definitions and notation of Davies [1986a] are followed where appropriate.

A'_T is defined as

$$A'_T = \frac{\Delta\rho}{\rho_o \alpha \Delta T} \tag{7.3}$$

and is the density anomaly ratio at which some specific phenomenon occurs, like the lowest density anomaly ratio at which tracers first fall to the base of the convecting system. At what A_T will this same phenomenon occur at a different R_T? At a new R_T the magnitude of the thermal buoyancy and the viscous stress are different. Since viscous stresses are proportional to velocity, which is proportional to $R_T^{2/3}$, c.f. equation (4.59), $\Delta\rho$ must increase as $R_T^{2/3}$ to resist this change. Moreover, while the viscous stresses are increasing as $R_T^{2/3}$, ΔT linearly increases in proportion to R_T. Thus

$$A'_T = \frac{\Delta\rho}{\rho_o \alpha \, \Delta T} \propto \frac{R_T^{2/3}}{R_T} \qquad (7.4)$$

$$A'_T = c_1 R_T^{-1/3} \qquad (7.5)$$

where c_1 is a constant. This relation will be tested below.

In order to find the relation between R_Q and A_Q, we must first find the relation between A_T and A_Q. The density anomaly ratio, in terms of a constant heat flux has been defined as (4.49)

$$A_Q = \frac{K \, \Delta\rho}{\rho_o \, \alpha \, D \, Q} \qquad (7.6)$$

The Nusselt number is defined in general as

$$Nu = Q/q_c \qquad (7.7)$$

where q_c is the heat which would be conducted in the absence of convection. In the numerical models used here, the basal heat flux was held constant, and the average temperature can be found across the bottom, $\bar{T}_b$; an approximate conductive heat flux can be defined as

$$\bar{q}_c = K(\bar{T}_b - T_t)/D \qquad (7.8)$$

A Nusselt number can then be defined as

$$N_{\bar{T}} = Q/\bar{q}_c \qquad (7.9)$$

Substituting (7.9) into (7.6)

$$A_Q = \frac{\Delta\rho}{\rho_o \alpha \, (\bar{T}_b - T_t)} N_{\bar{T}}^{-1} = A_{\bar{T}}/N_{\bar{T}} \qquad (7.10)$$

So

$$A_{\bar{T}} = N_{\bar{T}} \, A_Q \qquad (7.11)$$

The Nusselt number, N_T, is a function of R_T or R_Q:

$$N_T \propto R_T^{1/3} \propto R_Q^{1/4} \tag{7.12}$$

Substituting (7.11) and (7.12) into (7.5)

$$A'_Q = c_2 R_Q^{-1/2} \tag{7.13}$$

Scaling relations (7.5) and (7.13) were tested in the following way. An approximate thermal steady-state was calculated with $R_Q = 10^5$, Pe = 100 and steady plate model, s. A_Q was increased through a sequence of cases while the plates were held in the steady position; the value of A_Q when tracers first started to drop out of the flow was found ($A_Q = 0.5$). Then a similar set of cases were run (with the same flux of tracers) with $R_Q = 10^4$ and 10^6 and Pe's scaled using (4.59). The A_Q showing the most similar (qualitatively) type of behavior that the $R_Q{=}10^5$ case showed were found. These latter A_Q values were judged to be within about 10 % of the true transition value. The three cases are summarized in Table 7.3. The transition cases are shown in Figure 7.7 after 10 transit times of stirring.

In Figure 7.8a R_Q versus A_Q is shown. The solid line is the best fit and the dashed curve is the predicted power-law (7.13), forced to pass through the $R_Q{=}10^5$ datum. Considering the fact that the boundary layer theory scaling relations are only approximate and that the A_Q were only qualitatively judged, a good fit was found. Equation 7.11 has been used to convert A_Q into A_T and (7.12) to convert R_Q into R_T; these converted values are plotted in Figure 7.8b. Scaling relation (7.5) provides a good fit to the model cases. Thus, in order to scale some transition A'_Q to the mantle, we can use

$$A'_{Q_{\text{mantle}}} = A'_{Q_{\text{model}}} \left(\frac{R_{Q_{\text{model}}}}{R_{Q_{\text{mantle}}}} \right)^{1/2} \tag{7.14}$$

which follows from (7.13)

7.5.2 Preliminary Scalings to the Mantle.

Using (7.14) the model values can be scaled to the mantle. Moreover, since all of the non-dimensional models had a volume flux appropriate to the flux of oceanic crust into the mantle, a flux scaling must be made to consider the subduction of the entire lithosphere, as shown in section 4.4.2. Scalings will be made using both upper mantle and whole-mantle Rayleigh numbers and for two geological scenarios: oceanic crust and lithosphere remain layered after subduction and crust efficiently separates from the lower, depleted lithosphere after subduction.

At $R_Q = 10^5$, the lowest value of A_Q at which tracers start to segregate to the base (or neutralize the thermal buoyancy) was ≈ 2 for unsteady, bottom heated convection and ≈ 1 for unsteady, internally heated convection. Both values are for a crustal flux and have to be reduced by a factor of 5 to be appropriate to the subduction of the entire chemical lithosphere. Mantle A_Q were calculated using (7.6) and are listed in Table 7.4. A density of 200 kg/m^3 was assumed for subducted oceanic crust and 10 kg/m^3 was assumed as an upper limit on the integrated density of the entire chemical lithosphere. Other primary parameters are listed in Table 4.1. For upper mantle convection, it is marginally possible for subducted crust to start segregating out of the flow if the flow is primarily internally heated. Since upper mantle convection would be principally bottom heated, it is unlikely crust could segregate. For both heating modes, the scaled minimum A_Q is at least a factor of 10 larger than the upper limit on the mantle A_Q for the entire lithosphere ($\Delta\rho$ < 10 kg/m^3). Thus, if crust and lithosphere remain layered, there will be no segregation.

For whole-mantle convection, it is possible for crust, efficiently separated from the lithosphere, to segregate to the base of the convecting system, for either bottom or internally heated convection. If the integrated lithosphere has an integrated density difference of 10 kg/m^3 and there is no thermal boundary layer at the core mantle boundary, then it is marginally possible for some segregation of lithosphere to occur.

The results of this section can be applied to the model of Hofmann and White [1982], who hypothesized that subducted oceanic crust would separate from rest of the lithosphere and segregate to the core mantle boundary. The results of this section show that such segregation to the core mantle boundary could work; the only remaining question is, Could the crust indeed separate from the lithosphere? It would seem premature to reach any detailed conclusions until the feasibility of this mechanism is clarified; this is beyond the scope of the present work.

Table 7.1. Summary of mixing computations with intrinsic density
All cases: (i) tracers introduced over 10 transit times; (ii) $R_Q=10^5$;
$\dot{s} = (2x10^{-8})Pe$

Case	plate model	n	μ	Pe	Λ_Q	N_m	Γ_{peak}	run time
H1	s	15	1	100	0	-	-	30
H2	s	15	1	100	2	100	0.51	30
H3	s	15	0	100	2	100	0.73	40
H4	a	15	1	100	0	-	-	400
H5	a	15	1	100	1	100	0.35	90
H6	a	15	1	100	2	100	0.34	100
H7	a	31	1	100	2	25	0.76	20
H8	a	15	1	100	3	100	0.25	90
H9	a	15	1	50	0	-	-	300
H10	a	15	1	50	2	100	0.20	70
H11	a	15	0	100	0	-	-	60
H12	a	15	0	100	1	100	0.29	60
H13	a	15	0	100	2	100	0.63	80
H14	a	31	0	100	2	25	0.96	20@
H15	a	15	0	100	3	100	0.48	50
H16	c	15	1	100	0	-	-	100
H17	c	15	1	100	2	100	0.40	100

Notes:
@ Used to test cases with n=15

Table 7.2. Summary of mixing computations with intrinsic density
All cases: (i) continuous introduction of tracers (ii) $R_Q=10^5$,
(iii) Pe=100, (iv) $\dot{s}=2x10^{-6}$.

Case	plate model	n	μ	A_Q	N_m	Γ_{peak}	run time
C1	s	15	1	2.0	100	0.68	60
C2	s	15	0	2.0	100	0.25	60
C3	a	15	1	0.5	50	0.36	70
C4	a	15	1	2.0	50	0.66	120
C5	a	31	1	2.0	12	1.00	60
C6	a	31	1	6.0	12	0.58	60
C7	a	15	0	2.0	50	0.20	70
C8	a	15	0	6.0	25	0.48	60
C9	a	15	0	10.0	25	0.40	50

TABLE 7.3
Cases used to document A_Q-R_Q Scalings

R_Q	Pe	A_Q	$N_{\bar{T}}$	$A_{\bar{T}}$	$R_{\bar{T}}$
10^4	31.6	1.6	5.95	9.52	1.7×10^3
10^5	100	0.50	10.73	5.37	9.3×10^3
10^6	316	0.18	17.59	3.17	5.7×10^4

TABLE 7.4
Comparison of Mantle Values with Scaled Model Values

Parameter	Upper Mantle Convection $R_Q=4.5\times10^6$		Whole-Mantle Convection $R_Q=1.7\times10^9$	
	Complete Separation of Oceanic Crust	Lithosphere Remains Layered	Complete Separation of Oceanic Crust	Lithosphere Remains Layered
$\Delta\rho$ (kg/m^3)	200	<10	200	<10
mantle A_Q	0.15	<0.008	0.03	<0.0016
Minimum A_Q for Neutralization of Thermal buoyancy @ Mantle R_Q				
Bottom Heated	0.30	0.06	0.015	0.003
Internal Heating	0.15	0.03	0.008	0.0016

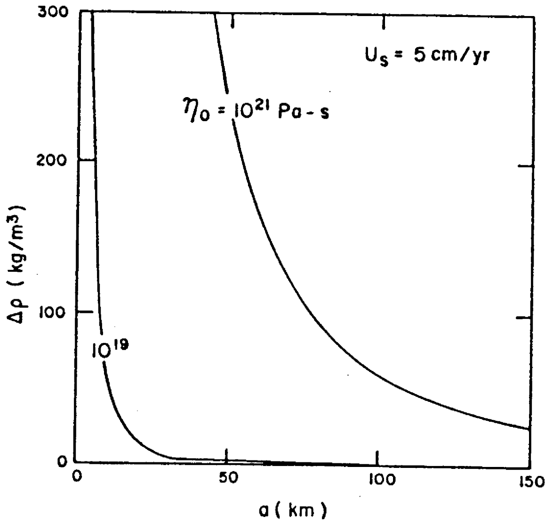

Fig. 7.1. Radii a and density differences Δρ necessary for a fluid sphere to achieve a velocity of 5 cm/yr. The average viscosity for the whole mantle is approximately 10^{21} Pa s; η_o = 10^{19} Pa s should be considered implausibly small. These calculations demonstrate that small-scale (~ 10 km) anomalies cannot achieve velocities comparable to velocities of mantle convection.

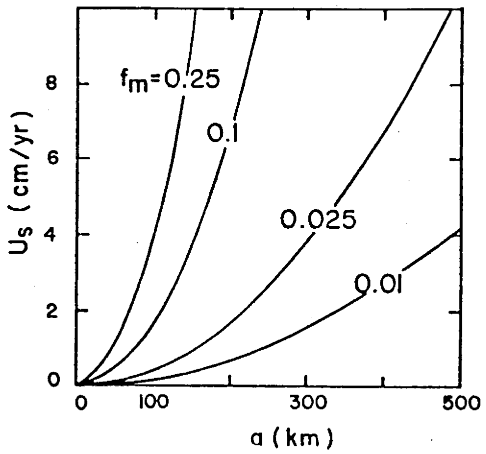

Fig. 7.2. Stokes velocities U_s as a function of sphere radius a. Each curve is for a density difference of $f_m\Delta\rho$, where $\Delta\rho$ = 200 kg m^{-3}. The viscosity is 10^{21} Pa s in all cases; f_m is the mixing fraction. These calculations demonstrate that very large anomalies (> 200 km across) can achieve significant velocities if material with an excess density of 200 kg m^{-3} is mixed with f_m > 0.01 through the region.

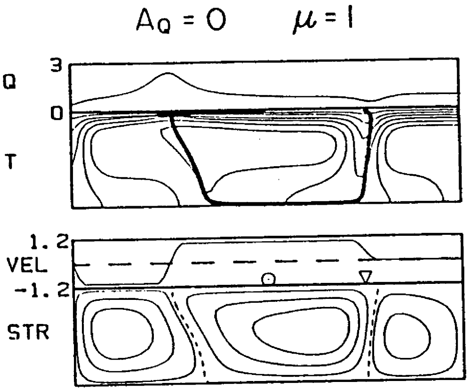

Fig. 7.3. Entry of passive tracers into a steady convective flow from a point source below the "trench" (triangle); this is case H1 in Table 7.1. The tracers are advected simply around the margin of the center cell, and all are sampled beneath the circle.

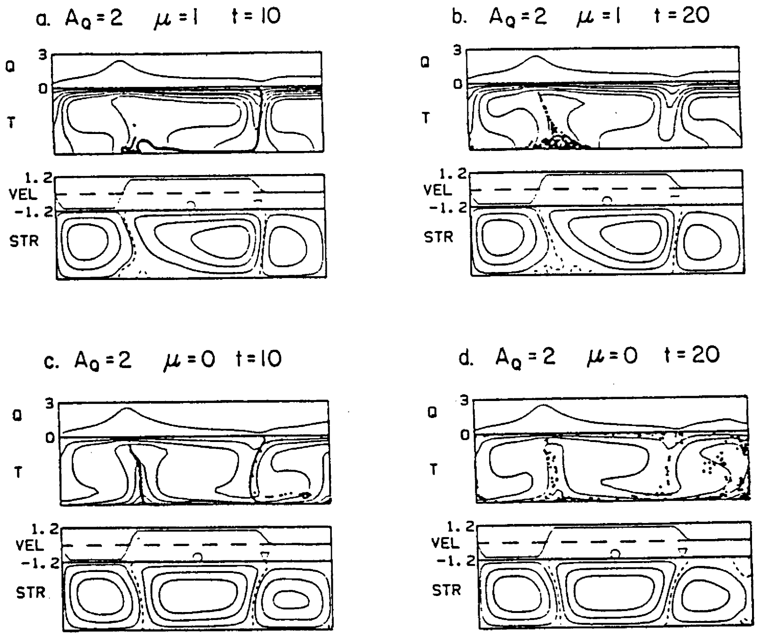

Fig. 7.4. Negatively buoyant tracers introduced into convective flows where the top boundary velocity has been held in a constant configuration. The density anomaly ratio (A_Q = 2) is constant for all cases. In internally heated flows (μ=1, in Figures 7.4a and 7.4b; case H2) the tracers segregate near the bottom of the warm upwelling region. However, in the bottom heated flows (μ=0, Figures 7.4c and 7.4d; case H3), the tracers can easily be swept by the flow and do not segregate to a significant extent. The times are in transit times.

Fig. 7.5. (overleaf) Introduction of heavy tracers in an internally heated flow with unsteady velocity boundary conditions; in all cases, $R_Q = 10^5$ and $A_Q = 2$. The tracers were introduced during the first 10 transit times. The tracers segregate to the base of the warm upwelling regions, but these regions of neutralized buoyancy are eventually dissipated by the unsteady flow. The times are in transit times.

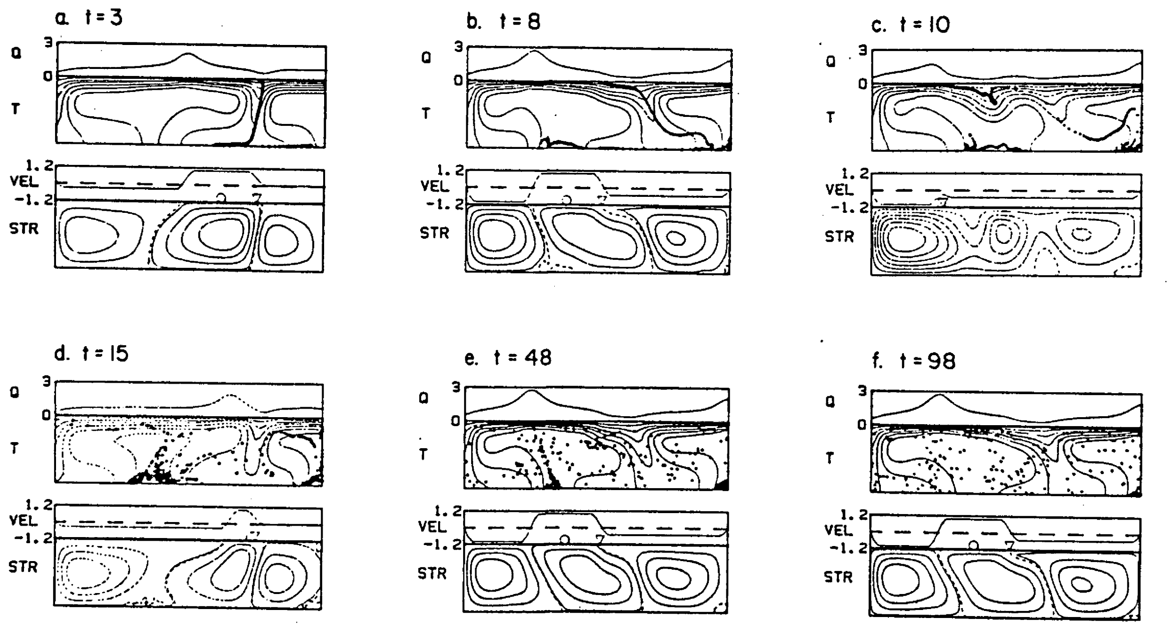

FIGURE 7.5

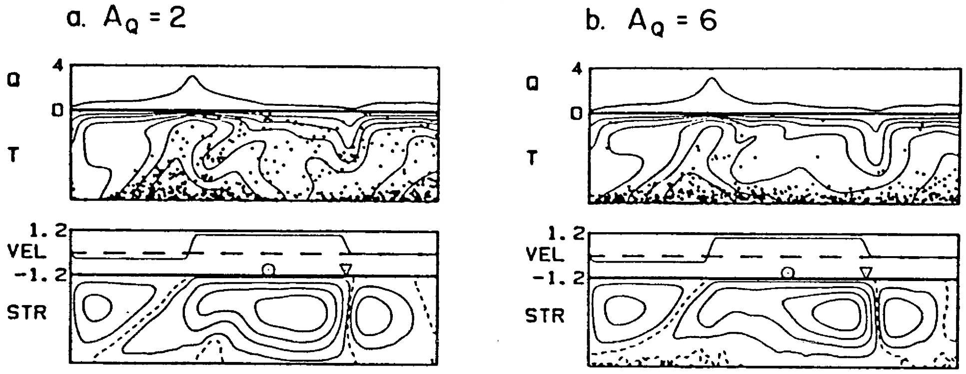

Fig. 7.6. Continuous introduction of heavy tracers into an internally heated flow after 61 transit times for (a) $A_Q = 2$ and (b) $A_Q = 6$. The transition to clear layering is rather indistinct but probably occurs somewhat above 6.

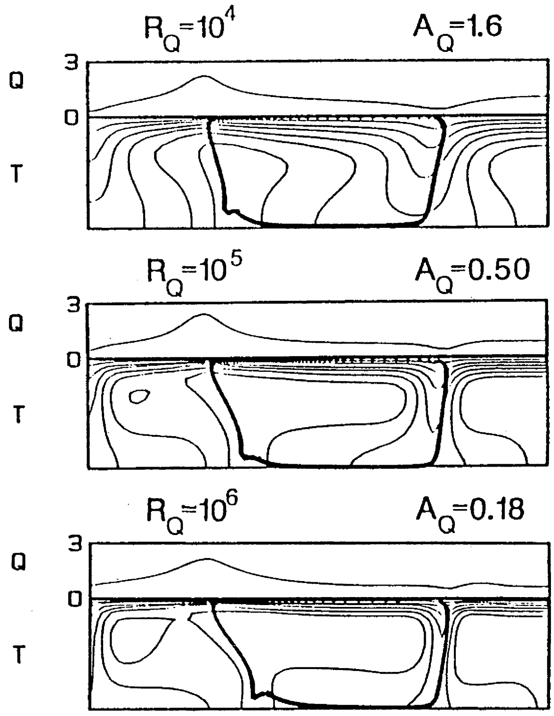

Fig. 7.7. Three cases at different R_Q; the A_Q's were chosen so that the tracers would just be starting to segregate. Steady plate model, s, used in all cases and the flux of tracers was also the same.

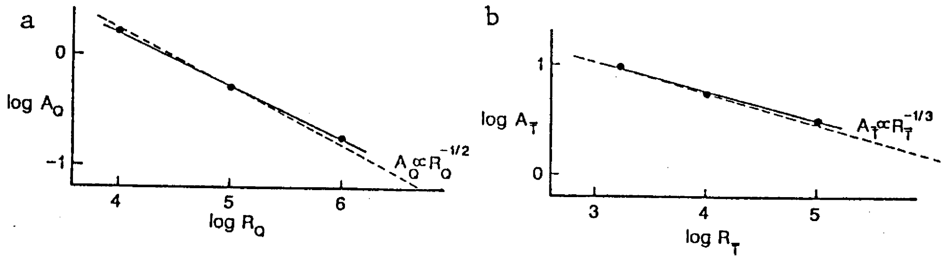

Fig. 7.8. a. A_Q versus R_Q for cases shown in Figure 7.7; solid line best fit and dashed line predicted by (7.13). (b) A_T versus R_T for cases shown in Figure 7.7; solid line best fit and dashed line predicted by (7.5).

CHAPTER 8

SCALING SURVIVAL TIMES TO MANTLE CONDITIONS

In the previous three chapters, no mention was made of dimensional model times; the computations were presented as simple fluid dynamical experiments used to explore basic mixing phenomena. Now, in this chapter, some of the theoretical results are scaled to the mantle. Both upper mantle and whole-mantle convection are considered when making the scalings. In this chapter, only the time-scale over which spatial heterogeneity persists, the survival time, is considered. Although the analysis is applied to some rather specific phenomena (for example, the persistence of blobs caused by laminar flow and unmixing), the analysis is general, and could be applied to other models, for example the steady flow models presented by Olson et al. [1984a] or the unsteady ones of Hoffman and McKenzie [1985]. The survival times, as will be seen, scale to a billion years or more. Since the rate of convection has declined appreciably over this time [McKenzie and Weiss, 1975; Burke et al., 1976], the decay of convection velocity with geologic time must be taken into account.

8.1 Linear Scalings

Heterogeneities are sheared out by the background flow; consequently, the survival time for a heterogeneity depends on the accumulated (or time-integrated) shear and will be a function of velocity. As derived in Chapter 1 for laminar mixing, e.g. (1.4):

$$\tau_s = \frac{\theta_o}{\dot{\varepsilon}_s \, \theta_{min}} = \frac{\theta_o}{2\,\theta_{min}} \frac{D}{U_b} \qquad (8.1)$$

where τ_s is the survival time, $\dot{\varepsilon}_s$ is the shear strain rate, D is the depth of the layer, U_b is the boundary convection velocity (plate velocity), θ_o is the initial dimension of the heterogeneity, and θ_{min} is the minimum resolvable dimension of heterogeneity. Since the transit time, t_t, is D/U_b, (8.1) can be rewritten as

$$\frac{\tau_s}{t_t} = \frac{\theta_o}{2\,\theta_{min}} = N_t \qquad (8.2)$$

where N_t is the number of transit times for the last (or average) heterogeneity to either survive or be resolvable at a scale θ_{min}. Thus, the scaling for the survival time is

$$\tau_s = N_t t_t \qquad (8.3)$$

Two quantities will be scaled using (8.3): (i) the time for a clump of tracers to persist in some convective flow and (ii) the time for the quantity θ_{max}/θ_o to be reduced to 10 %. Survival times will first be scaled assuming constant velocity and hence constant transit time.

Using an average velocity, U_b, of 5 cm/yr the transit time for convection confined to the outer 700 km of the mantle is 14 m.y. and for convection extending throughout the whole-mantle is 60 m.y. Shown in Table 8.1 are some scalings made using (8.3), assuming whole-mantle convection. For flows in constant viscosity fluids, the most persistent clumps of tracers survived for about 40 transit times, which scales to 2.4 b.y. For upper mantle convection, 40 transit times scale to 560 m.y. (Table 8.2). Moreover, the maximum width of a passive heterogeneity to be reduced to 10 % (e.g. $\theta_{max}/\theta_o = 0.1$) is 220 transit times which scales to 13 b.y., for whole-mantle convection.

Also displayed in Table 8.1 are two cases with depth-dependent viscosity, both of which are acceptable with current constraints on the mantle viscosity distribution. The survival times for the case with the exponential viscosity distribution in Table 8.1 was discussed in Chapter 6. For this case, clumps of tracers persisted for about 110 transit times which scales to 7 b.y.

These scaled survival times, especially for the cases with depth-dependent viscosity, are so long in comparison with the 4.5

billion year age of the earth that the assumption of a constant convection velocity with geologic age must be critically evaluated.

8.2 Effects of Thermal History on Survival Time

Constant plate velocity over billions of years is a poor assumption. The plate velocity history, really the convective velocity history, depends upon uncertain features of the mantle, most importrant being its thermal history. The thermal history of the earth has been the subject of a number of theoretical studies using parameterized convection models which account for such features as: heat generation and heat loss, average temperature, and average viscosity [e.g. Davies, 1980b; Schubert *et al*., 1980; Turcotte, 1980]. The treatment of the thermal history is based on two fundamental features of the mantle: (i) that heat transport is dominated by convection, and (ii) that the viscosity of the mantle is controlled largely by its temperature. Probably the most important conclusion which bears on the present study is that heat loss approximately tracks heat generation, at least after an initial period of rapid cooling during the first billion years when most (but not all) primordial heat was lost. This means that the thermal history of the mantle can be approximated as a simple exponential over at least the last 2.5 b.y. The approach which will be taken is to use simple thermal models of the mantle to investigate their effect on mixing timescales; a definitive scaling is not expected.

The likely effects of increased convection velocities in the past on survival time scalings can be considered by relating convective velocities to the heat flux. Two equations (both presented already) are required: one relating heat flux to Rayleigh number and the other relating velocity (Peclet number) to Rayleigh number. The normalized heat flux is a function of the Rayleigh number:

$$Nu = q/q_c = a(R_Q/R_c)^p \qquad (8.4)$$

which is essentially (7.12) previously defined, and Nu is the Nusselt number, q is the total heat transported, q_c the heat which would be conducted in the absence of convection, and R_c is the critical Rayleigh number. The exponent p (≈ 1/4) does not strongly depend on the mode of heating (either bottom or internal) or the type of fluid rheology (either strain-rate dependent, [Parmentier *et al*., 1976] or temperature-dependent [Booker, 1976]. Critical to some of the scalings made here, p does not depend on the depth-dependence of viscosity [Gurnis and Davies, 1986]. The second equation necessary relates velocities to Rayleigh number, from (4.59)

$$U_b = b\, R_Q^{\,r} \qquad (8.5)$$

where r is a constant of about 1/2. Gurnis and Davies [1986] show that r is independent of the depth-dependence of the viscosity. Combining equations (8.4) and (8.5)

$$U_b \approx c\, q^2 \qquad (8.6)$$

where c is a constant. Equation (8.6) is only an approximation because the dependence on q_c (the equivalent conductive heat flux) has been dropped because it is directly proportional to the temperature difference. Gurnis and Davies [1985] have shown that $q_c \approx q^{1/10}$ which justifies (8.6) as an approximation. Equation (8.6) can also be derived from the cooling of a plate, which is the basis of the boundary layer theory [Turcotte and Oxburgh, 1967].

As a first approximation the thermal history is assumed to vary as

$$q = q_i\, e^{-\gamma t} \qquad (8.7)$$

where q_i is the initial heat flux and γ is the thermal history decay constant. As previously discussed, the value of γ depends mainly on the internal heat generation rate [Davies, 1980b; Schubert et al., 1980; Turcotte, 1980], such that γ is primarily controlled by the K/U ratio of mantle rocks. The K/U ratio for the mantle probably lies between 10^4 and 2×10^4, with an upper (chondritic) limit of 8×10^4 [e.g. Stacey, 1977]. These K/U values bracket thermal half-lives of 2.25 to 1.5 b.y., respectively. Low values of K/U are suggested from the generally low ratios of all terrestrial rocks. This suggests that the half-life of internal heat production is close to 2 b.y.

The increased velocities will progressively decrease the transit time for progressively greater ages. Substituting (8.7) into (8.6) and setting U_b = dx/dt

$$\frac{dx}{dt} = U_b e^{2\gamma t'} \qquad (8.8)$$

where t' is geologic age (4.5 b.y. - t). Integrating (8.8), and solving for the time

$$t_{nD} = \frac{1}{2\gamma} \ln\left[\frac{2nD\gamma}{U_b} + 1 \right] \qquad (8.9)$$

where the time, t_{nD}, to make n transits of the mantle of depth ,D, (i.e. time to traverse a distance nD). In Figure 8.1, (8.9) is plotted for the two convection scenarios; a thermal half-life of 2 b.y. and a present plate velocity of 5 cm/yr was assumed for both cases. The scaled times are reduced from those obtained assuming a constant rate of convection.

This simple exponential model with a 2 b.y. thermal half-life is used to rescale the values already presented in Table 8.1. As shown, all survival times are reduced and those survival times originally greater than 3 b.y. have been reduced considerably. Most importantly, however, the scaled survival times (Tables 8.1 and 8.2) are still on the order of billions of years and for whole-mantle convection always greater than one billion years.

Some of the cases have significant heterogeneity surviving from before 4 b.y. ago. As alluded to above, the exponential form of the thermal history does not hold for about the first billion years of earth history (because of planetary accretion and core formation). In order to assess the effect of different initial conditions (different initial temperatures) a parameterized convection model is used. The model used is derived in Gurnis and Davies [1985] and is similar to a number of others, including Davies [1980b] and Schubert *et al*. [1982]. Shown in Figure 8.2a are three parameterized thermal histories (solid lines); the histories have a heat production with a 2 b.y. half-life and were initiated at: 500, 1500, and 2300 K. Also shown for comparison in Figure 8.2 is a simple exponential thermal history with a 2 b.y. half-life (dashed curve) and a constant thermal history (dot-dashed curve). Using the geological constraints (such as, oldest surviving crustal rocks, existence of komatiite lavas, and the oldest recorded geomagnetic field) cited by Davies [1980b], the model thermal history with an initial temperature of 500 K (Figure 8.2a) is extreme because of the low heat flux predicted prior to 2.7 Ga; the other models are acceptable. The number of transit times was found by numerically integrating these thermal histories in conjunction with (8.6), as displayed for each history in Figure 8.2b.

The results in Figure 8.2b show that the exponential thermal history (dashed curve) adequately estimates, in fact under-estimates, scaled survival times for all transit times and initial temperatures, except for transit times greater than 500 and initial temperatures greater than 2300 K. Thus all of the survival times scaled using the exponential thermal histories (Table 8.1) give about the same age as would a more realistic thermal history. The conclusion of chemical heterogeneity surviving from the earliest phases of earth history remain unchanged with the use of a hot-start thermal history.

8.3 Conclusions

In terms of the whole-mantle convection scenario, the persistence of chemical anomalies in these mixing calculations (as presented in Chapters 5 to 7) is in accord with the persistence of mantle chemical reservoirs for billions of years, even assuming the mantle was convecting much more vigorously in the past. Furthermore, the scaled results lend strong plausibility to the hypothesis that much of the isotopic and chemical heterogeneity of the mantle is in blobs that are entrained in convective flow [Davies, 1984; Zindler et al., 1984], a hypothesis hitherto thought kinematically unsound [McKenzie, 1979; Hoffman and McKenzie, 1985].

Moreover, for the cases with depth-dependent viscosity, chemical heterogeneity can survive from earlier than 4 billion years ago assuming both whole-mantle convection and a hot start thermal history. This result is completely at odds with conventional wisdom which maintains that primitive mantle could not survive in whole-mantle flow [Allègre et al., 1983; O'Nions and Oxburgh, 1983]. This result suggests that such observations as the continuing degassing of ^{3}He from the mantle does not demand a layered mantle and, on the contrary, whole-mantle convection seems consistent with such an observation. This point will be discussed further in Chapter 10 when the residence times are scaled to mantle conditions.

TABLE 8.1

Survival Times
Whole-Mantle Convection

	constant viscosity	depth-dependent viscosity	
		layered $\eta_L/\eta_U=100$	exponential $\beta=3.5$
$\bar{\eta}/\eta_0$	1	20	60
clump survival time			
N_t (transit time)	40	65	110
τ_s, constant velocity	2.4 by	3.9 by	6.6 by
τ_s, exponential thermal history	1.4 by	1.9 by	2.5 by
time for $\theta_{max}/\theta_0=0.1$			
N_t (transit time)	220		
τ_s, constant velocity	13 by		
τ_s, exponential thermal history	3.3 by		

TABLE 8.2

Survival Times
Whole mantle versus upper mantle scalings for constant viscosity

quantity	whole-mantle convection	upper mantle convection
t_t, transit time (my)	60	14
N_t, clump survival time	40	40
τ_s, clump survival time		
constant velocity	2.4 by	0.6 by
exponential thermal history	1.4 by	0.5 by
N_t for $\theta_{max}/\theta_o=0.1$	220	220
τ_s for $\theta_{max}/\theta_o=0.1$		
constant velocity	13 by	3 by
exponential thermal history	3.3 by	1.6 by

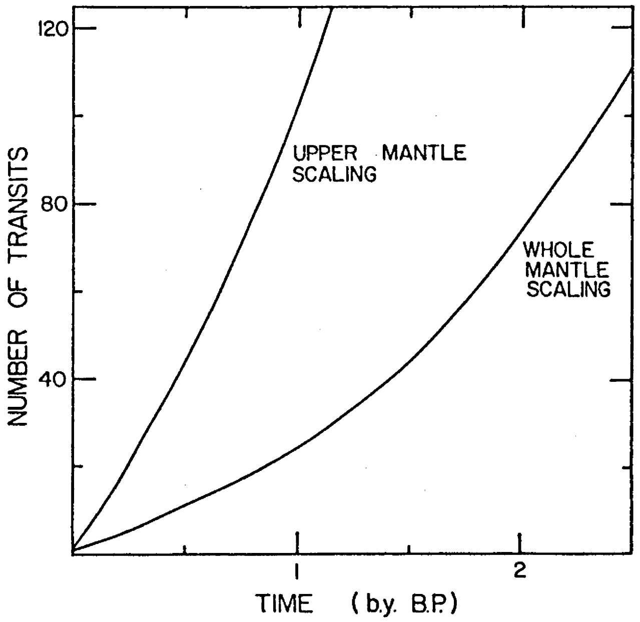

Fig. 8.1. Cumulative number of transits of the mantle for progressively greater ages before the present, assuming that the heat flux half-life is 2 b.y. and the present plate velocity is 5 cm/yr. These curves allow the survival times of clumps of tracers to be scaled to the mantle.

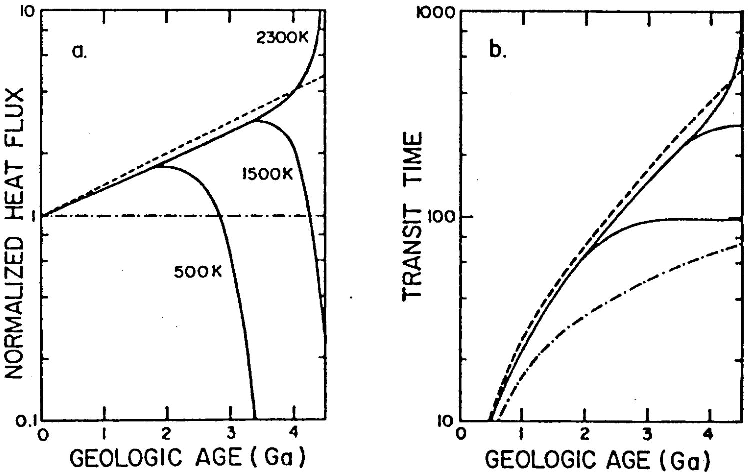

Fig. 8.2. a. Thermal history models for the earth normalized by the present heat flux out of the mantle. Solid lines for the parameterized convection models, dashed line for the exponential model, and dot-dashed line for the constant heat flux model. b. The cumulative transit times for these thermal histories. Same lines as in a.

CHAPTER 9

RESIDENCE TIMES

As discussed in Chapter 3, isotopic and other geochemical observations of oceanic basalts are consistent with the hypothesis that much the isotopic heterogeneity of the mantle is caused by the reprocessing of the mantle; in particular, that the mantle is continuously fractionated beneath ridges, that the products of this fractionation, oceanic crust, are subducted back into the mantle, and that this subducted material, after stirring through the mantle, is sampled through MORB and OIB volcanism [Chase, 1981; Hofmann and White, 1982; Davies, 1984]. If this hypothesis is true, then the linear arrays on Sr and Pb isotope plots (e.g. Figures 3.1 and 3.2) have a simple interpretation: the arrays are "average" isochrons with an age primarily controlled by the time subducted MORB resides in the mantle. For the standard mixing calculations presented in Chapters 5 to 7, the tracers were introduced into the flow in a way that simulates subduction of lithosphere and removed in a way that simulates incorporation into the oceanic lithosphere (e.g. magmatic sampling beneath ridges). Thus the mixing calculations explore an important consequence of the physical process envisaged: average age and pattern of sampling; the results of these calculations can be compared to isotopic observations. In this chapter, the residence times are presented in non-dimensional terms and in the next chapter are scaled to the mantle.

The mean residence time, t_r, is defined as the average time tracers remain in the box. Only in some cases was t_r directly calculated by sampling all of the tracers in the box. In many cases, because tracer sampling was sluggish, the time to sample all of the tracers would have required an exorbitant amount of computer time. However, it is shown that the residence time can be adequately inferred from the rate of tracer sampling; the assumption upon which this is based, random sampling, is tested. Once the general procedures have been established, the effect different features of the mantle (like depth-dependent viscosity) have on residence times, are explored.

9.1 Random Sampling Model

The residence times and the rate at which the tracers are sampled are conveniently interpreted by first introducing some rather elementary concepts. In particular, the residence time expected in the special case of the random sampling of tracers is derived. Another relevant quantity is the flux time, t_f, which is the time for an area equivalent to the box area to flux through the sample region of depth, d_s:

$$t_f = \frac{S}{d_s u_b} = \frac{S\ Ra}{d_s Pe} \tag{9.1}$$

where S is the dimensionless area of the box, $d_s u_b$ is the dimensionless flux through the sample region, and u_b is the imposed boundary velocity. If the flux time, t_f, is scaled by the transit time (4.54), then

$$\frac{t_f}{t_t} = \frac{S}{d_s} \tag{9.2}$$

where t_t is the transit time defined in terms of the boundary velocity (4.55).

In random sampling it is assumed that each tracer has an equal probability of being sampled, which implies that the rate of sampling or the rate at which the total number of tracers remaining in the box, N(t), decreases is proportional to the total number in the box. Furthermore, random sampling implies that the rate of sampling should be proportional to the flux rate of fluid through the sampling region times the number of tracers per unit area:

$$\frac{\partial\ N(t)}{\partial\ t} = -\lambda N(t) = -[\frac{u_b d_s}{S}]N(t) \tag{9.3}$$

where λ is the tracer sampling decay constant. From (9.1), (9.3) implies $\lambda = 1/t_f$, under the assumption that the average velocity of fluid moving through the sampling region is about the same as the boundary velocity (plate velocity). The solution to (9.3) is

$$N(t) = N_o e^{-\lambda t} \tag{9.4}$$

where N_o is the number of tracers at time 0. It can be shown from (9.4) that the mean age is $1/\lambda$.

A sufficient condition to demonstrate random sampling is that the number remaining in the box decays exponentially, which can be tested by plotting $\ln(N/N_o)$ versus transit time. If the measured values form a linear trend (i.e., exponential decay), then we have shown that the tracers are sampled randomly, and we calculate a slope, λ_m, and compare $1/\lambda_m$ with t_f and t_r. It may be the case, however, that $t_f \neq 1/\lambda_m$, because the imposed boundary velocity may not be exactly the same as the velocity of the tracers through the sample region, although it should be a good first approximation.

9.2 Measured Residence Times

9.2.1 Passive Tracers in Constant Viscosity Fluids.

These tests of random sampling have been carried out for the mixing calculations described in Chapter 5 where the tracers were passive and the viscosity constant through the fluid (Table 5.1). The dimensionless area of the cavity, S, is 4. The d_s were calculated for a dimensional sub-ridge sampling depth (depth of melting) of 100 km, so that for whole-mantle convection $d_s = 100\text{km}/3000\text{km} \approx 0.05$ and $d_s = 0.15$ for upper mantle convection. Therefore, the flux time is 80 transit times for whole-mantle values and 27 for upper mantle values.

Reproduced in Table 9.1 are the calculated residence time parameters for the cases originally presented in Table 5.1; tabulated are the flux time normalized by the transit time (t_f/t_t), the residence time normalized by the transit time (t_r/t_t), the inverse of the slope of the tracer versus time relation normalized by the transit time (λ_m^{-1}/t_t), the number of tracers introduced into the flow, and the number of tracers sampled.

In Chapter 5 case P1 was discussed in detail as a model exhibiting general phenomena; for case P1, a periodic plate evolution model was used and $R_Q = 10^5$ and $Pe = 10^2$. Features of this calculation were shown in Figures 5.6, 5.7, and 5.8. In Figure 9.1 the number of tracers remaining in the box is plotted against transit time. For long time scales the random sampling model described by (9.3) holds, as shown in Figure 9.1. In Figure 9.1, the open squares are the number of tracers in the box at the end of each period and are only plotted if tracers were sampled during the time interval. The dashed line is predicted from the flux time by (9.3) and has a slope $1/t_f$. The solid line is a linear regression of the points shown; it has a slope of λ_m ($1/\lambda_m$ = 75 transit times) and a correlation coefficient, r, of -0.994. Both lines give equally good fits to the numerical model results. The random sampling model even holds for transit times < 50 (Figure 9.1) despite the spatial heterogeneity of the source region (Figure 5.7). In summary, for case P1, we find $t_f/t_t = 80$, $\lambda_m^{-1}/t_t = 75$, and $t_r/t_t = 70$, which is an internally consistent set of results: the tracers are sampled approximately randomly, and we can predict the residence time and the rate of sampling from the flux time.

When linear trends were fit to the other cases, we found r < -0.99 (except for one, case P5, which had an r = -0.976). In addition the residence time can be predicted by the flux time to within about 20%. This quantitatively demonstrates the good fit provided by the random sampling model. Although there is an added complication because of the introduction of the tracers into the flow over a finite period of time, rather than at one instant, the effect is ignored to a good approximation, because the time to sample all the tracers is hundreds of transit times.

9.2.2 Passive Tracers in Fluids with Depth-Dependent Viscosity

As discussed by Davies [1984], if the lower mantle has a relatively high viscosity then the residence time of mantle material would be prolonged. In order to explore this hypothesis, tracers were also sampled in some of the mixing calculations incorporating depth-dependent viscosity. In addition to the continuous introduction of tracers beneath the trench (recycled tracers), the tracers were also introduced into the flow as an initial layer of tracers at the base (basal tracers), as discussed in Chapter 6.

Some interesting features were noted in the way recycled tracers were stirred by the flows with depth-dependent viscosity, in comparison with constant viscosity fluids (Chapter 6). In particular, it was noted that when $\beta = 2$ (e.g. $\eta = 10^{\beta(1-y)}$), that tracers could be stirred into the basal regions within about 30 transit times (c.f. Figure 6.4a). However, if the viscosity increase was made even larger ($\beta = 3.5$) that tracers take about 100 transit times to be stirred into the basal regions. As shown in Figure 6.4b for $\beta = 3.5$ after 100 transit times the number of tracers remaining in the box has been reduced significantly. This difference in the way recycled tracers are stirred strongly shows up in the residence times inferred from the rate of sampling (Table 9.2). For Case D4 with $\beta = 2$, $\lambda^{-1}{}_m/t_f = 2.0$ (twice the expected time for a constant viscosity fluid), while for Case D9 with $\beta = 3.5$, the residence times is only $\lambda^{-1}{}_m/t_f = 1.1$ (to 1.4 depending upon how the sampling time is measured, see Figure 9.2). Apparently, because plate rearrangement (and consequently ridge migration) is so rapid with respect to the time for recycled tracers to be stirred into the deeper parts, recycled tracers are "rapidly" sampled. The details of the dependence of residence time on either $\bar{\eta}/\eta_0$ is unclear, as only a few residence times were calculated.

One thing seems certain, however, that the residence times of recycled tracers cannot indefinitely increase with increasing viscosity contrast: as the viscosity increases the recycled material "senses" a thinner convecting region. The residence times for recycled material may be maximized in the range $\bar{\eta}_L/\bar{\eta}_U = 10$ to 50, which perhaps fortuitously is within the range of permissible values [Hager, 1984; Richards and Hager, 1986].

In addition to the recycled tracers, tracers were also introduced as a uniform layer along the base at the start of the model run; this form of tracer introduction was chosen to see how long a deep layer of material could remain isolated from the surface. For the basal tracers, the number of tracers remaining in the box versus transit time is plotted for those cases with exponential viscosity distributions. In contrast to the sampling of recycled tracers, basal tracer sampling time can be indefinitely increased. As shown in Figure 9.3, tracer decay is not so well represented by a single exponential, except for the $\beta = 0$ case, because of irregularities in sampling due to large scale heterogeneity. Instead of extracting an exponential decay time, the time to sample 75 percent of the tracers is used as a measure of the persistence of the tracers.

This sampling time smoothly increases with β (Figure 9.4). To a good approximation, the sampling time should be inversely proportional to the sampling depth, e.g. (9.1). This dependence allows the sampling time versus β (viscosity contrast) relationship to be scaled to different d_s and the dashed line in Figure 9.4 is the predicted effect of halving d_s.

9.2.3 Heavy Tracers in Constant Viscosity Fluids.

In Chapter 7, it was found that if tracers had intrinsic density, that they tended to segregate to the base of hot upwelling regions. This effect causes the recycled tracers to persist longer in the convecting region. The dependence of residence time on intrinsic density is explored in this section.

In section 7.3 case H6 was studied in detail; this case is analogous to case P1 studied in section 9.2.1 (above) with the same R_Q ($=10^5$) and Pe ($=100$), and plate model, the only difference is that now the tracers have an intrinsic negative density ($A_Q = 2$, for a flux of tracers appropriate to the flux of oceanic crust into the mantle). The stirring of the tracers is shown in Figure 7.5 and in Figure 9.5 the fraction of tracers remaining in the box (N/N_O) as a function of transit time is shown. The dashed curve is an expected exponential decay for $t_f = 80$ transit times and the solid line is a regression through the actual values: $\lambda^{-1}{}_m/t_f$ has been increased by a factor of 1.8 when A_Q was increased from 0 to 2. For this case the tracers were introduced into the flow during the first 10 transit times (first period of the periodic plate model). Moreover, there was a further increase in λ^{-1}_m/t_f (Case C4) of 5-10 percent when the tracers were introduced for the entire model run; this further increase was not judged to be significant in the present context.

The dependence of the residence time on the intrinsic density is presented in Figure 9.6. When the tracers have excess negative buoyancy, sampling becomes sluggish and $\lambda^{-1}{}_m/t_f$ increases from unity. In the figure only those cases with periodic plate evolution, $R_Q = 10^5$, $Pe = 10^2$ and with tracers introduced over 10 transit times have been plotted; the heating mode and density anomaly ratio vary. The calculated results were previously listed in Table 7.1. The open circles are for bottom heating ($\mu=0$) and the solid circles for internal heating (μ=1). The residence times appear to be independent of heating mode. The dashed line in Figure 9.6 has the form:

$$\frac{\lambda_m^{-1}}{t_f} = 1.0 + \left(\frac{\delta w}{6\ \mathrm{km}}\right)\cdot 0.58 A_Q \qquad (9.5)$$

where δw is the dimensional width of a subducting sheet of dense fluid with A_Q. The numerical calculations were carried out for an injected flux of tracers appropriate to δw = 6km (crustal flux). The calculations can be linearly scaled to a lithospheric flux (δw = 30 km), as described in section 4.4.2.

In order to use (9.5) to estimate the increase in λ_m^{-1}/t_f for different geological scenarios, mantle A_Q's must be scaled to $R_Q = 10^5$. In Table 9.3 the scaled parameters necessary to find the increase in λ_m^{-1}/t_f are shown for both upper mantle and whole-mantle convection. For upper mantle convection, for example, the A_Q calculated from mantle parameters via (7.6), previously listed in Table 7.4, are shown; these are the A_Q at $R_Q = 4.5 \times 10^6$. These values are scaled to $R_Q = 10^5$ using (7.14): A_Q increases from 0.15 to 1.0 in going from the mantle R_Q to $R_Q = 10^5$. Using (9.5) with this A_Q and a δw = 6 km, λ_m^{-1}/t_f is increased to 1.58 (i.e. a 58 % increase in residence time compared to the passive case). The other cases in Table 9.3 were scaled in the same way.

A particularly large increase in residence time was found for the fluxing of pure crustal material into whole-mantle convection: λ_m^{-1}/t_f is increased by a factor of ≈ 3 from the passive case. Physically, such a large increase would occur because much of the heavy material has segregated to the base and formed discontinous patches under warm uprising areas. The increase in residence time for the other cases was not so extreme, although significant, because there was only a slight amount of segregation of recycled material to the warm basal regions.

TABLE 9.1
Summary of Residence and Sampling Times
Constant Viscosity Cases

Case*	d_s	t_f/t_t	t_r/t_t	λ_m^{-1}/t_t	t_r/t_f	Number	Number Sampled
P1	0.05	80	70	75	0.9	250	250
P2	0.05	80	67	80	0.8	250	250
P3	0.05	80	127	164	1.6	200	198
P4	0.05	80	79	85	1.0	300	300
P5	0.15	27	33	34	1.2	200	200
P6	0.05	80		97		650	416

*Other parameters for these cases given in Table 5.1

TABLE 9.2
Summary of Sampling Times
Depth-Dependent Viscosity

Case*	Type	β	$\bar{\eta}/\eta_o$	recycled λ^{-1}_m/t_f	basal time to sample 75% of tracers
D1	C	0	1	1.2	128
D3	E	1	3.2		172
D4	E	2	10	2.0	
D5	E	2.5	17.8		255
D9	E	3.5	56.2	1.1-1.4	276
D10	L	-	20.9	1.3	123

* Other parameters for these cases are given in Table 6.1
All cases; $d_s = 0.05$.

TABLE 9.3
Effect of Intrinsic Density on Residence Times

Upper Mantle Convection

	δw	A_Q ($R_Q=4.5\times10^6$)	A_Q ($R_Q=10^5$)	$\frac{\lambda_m^{-1}}{t_f}$
Crustal Flux	6km	0.15	1.0	1.6
Lithospheric Flux	30km	<0.008	<0.05	<1.15

Whole-Mantle Convection

	δw	A_Q ($R_Q=1.7\times10^9$)	A_Q ($R_Q=10^5$)	$\frac{\lambda_m^{-1}}{t_f}$
Crustal Flux	6km	0.03	3.9	3.3
Lithospheric Flux	30km	<0.0016	<0.21	<1.6

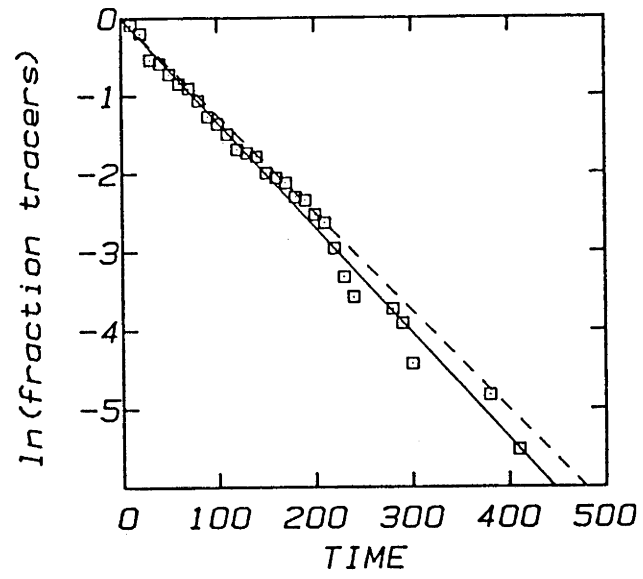

Fig. 9.1. Log of fraction of tracers remaining in the box as a function of transit time for case P1. The solid line is a least squares fit to the points, and the dashed line is the model predicted by the flux time. This clearly demonstrates that the number of tracers remaining in the box decays exponentially, and hence that tracer sampling is random.

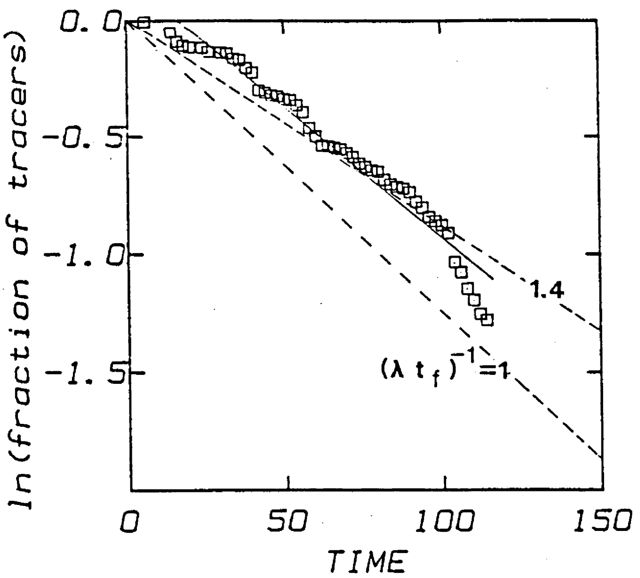

Fig. 9.2. Number of recycled tracers remaining in the box as a function of transit time for case D9 with $\beta = 3.5$. Two exponentials (dashed curves) are shown with decay constants of 1 and 1.4 t_f. The solid line is a regression through the points plotted. The residence time appears to be in the range 1.1 to 1.4 t_f.

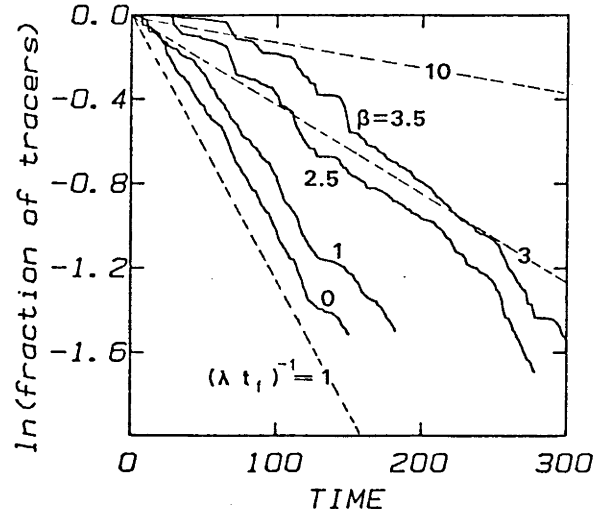

Fig. 9.3. Number of basal tracers remaining in the box versus transit time for four cases with exponential depth-dependent viscosities. The dashed lines are exponentials with decay constants of 1, 3, and $10t_f$.

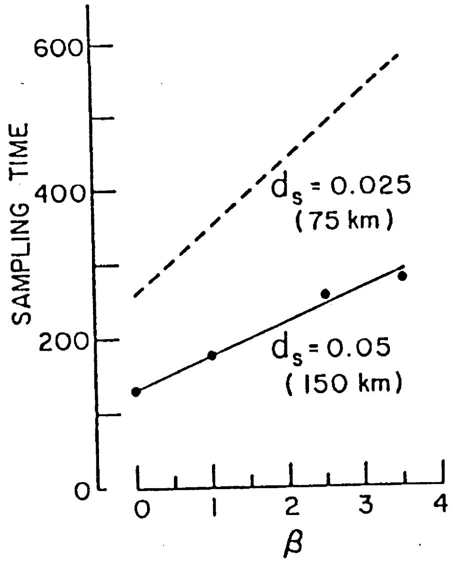

Fig. 9.4. The number of transit times to sample 75 % of the basal tracers as a function of β (viscosity contrast). The dashed curve is the expected sample time for d_s=0.025. The dimensional values of d_s are for whole-mantle convection.

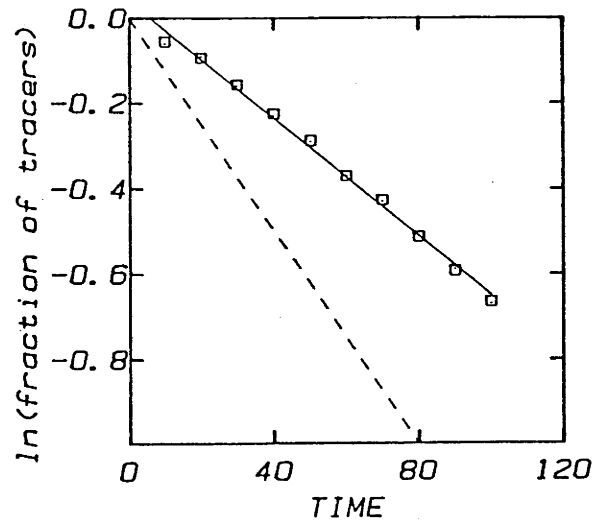

Fig. 9.5. Fraction of tracers in the box for case H6 (squares), which is shown in Figure 7.5. The dashed line is expected for passive tracers; the solid line is a linear regression of the data values. The time constant for the rate of sampling has increased by a factor of 1.8 when A_Q is increased from 0 to 2.

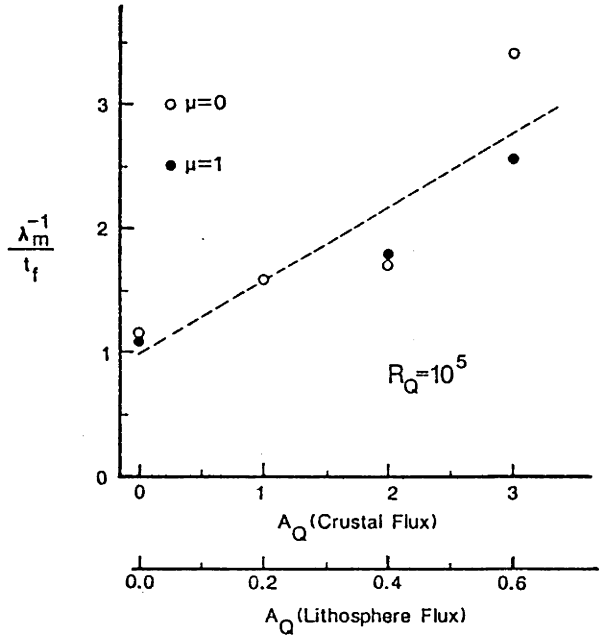

Fig. 9.6. Increase of the sampling time constant λ_m^{-1}/t_f and hence residence time, as a function of density anomaly ratio A_Q The relation is not strongly dependent on heating mode (e.g. μ=0 for bottom heating or μ=1, internal heating). The dashed line is a linear regression, as given in (9.5).

CHAPTER 10

SCALING RESIDENCE TIMES TO MANTLE CONDITIONS

The mean residence times of tracers are scaled in this chapter to dimensional model times. Both upper mantle and whole-mantle convection are considered when making the scalings. Scaling the residence time depends on both convection velocity and the size of the sampling region(s). In the numerical model, the sampling region reduces to a single sampling depth; when scaling to the mantle, however, the total length of ridges and the depth of sampling by magmatism must be considered. The residence times will scale to a billion years or more, and as shown in Chapter 8, the decay in the rate of convection must be considered over such time scales.

10.1 Random Sampling and the Age Distribution

Both plate velocities and total sampling volume must be considered in the scalings of residence times. In the scalings, we approximate the sampling of heterogeneities by a simple random sampling model. It was shown in the previous chapter that such random sampling held for constant viscosity flows; however, such a simple model did not hold so well for the sampling of fluids with depth-dependent viscosities, as will be discussed later.

The volumetric rate of mantle recycling (i.e., the fluxing of fractionated mantle through the oceanic crust and depleted lithosphere) is approximated as the product of the areal rate of plate generation, $\dot{A}$, and the depth over which partial melt is extracted, d_m; this depth is at least of the order of the depth of oceanic crust, d_{oc}, divided by the degree of partial melting, F,

$$\dot{V}_r \approx d_m \dot{A} \sim \frac{1}{F} d_{oc} \dot{A} \qquad (10.1)$$

and may be even larger.

The reprocessing of mantle rocks over time leads to an age distribution, which is the fraction of mantle volume versus the age since last fractionation. In other words, at time t, the mantle is grouped into small volumes, $v(\tau,t)d\tau$, with ages between τ and $\tau+d\tau$; the volumes need not be continuous but may be dispersed throughout the mantle; the volumes must be large enough so that their isotopic identity is retained. Applying the result of the numerical calculations, the parcels of the mantle are assumed to be sampled randomly below ridges. This means that the rate at which a mantle parcel of age τ is reprocessed is proportional to the total volume of that age:

$$\frac{\partial\ v(\tau,t)}{\partial\ t} = -\ \sigma\ v(\tau,t) \qquad (10.2)$$

where σ is a positive quantity. A simple limiting case is obtained if σ is constant. In this limit and with the boundary condition $v(0,t) = \dot{V}_r$ (i.e., the rate of reprocessing of zero-age material at any time t is $\dot{V}_r$) the solution to (10.2) is

$$v(\tau,t) = \dot{V}_r\ e^{-\sigma\tau} \qquad (10.3)$$

If the mantle volume, V_m, remains constant in time, then

$$\int_0^t v(\tau,t)\ d\tau = V_m \qquad (10.4)$$

From (10.4), we find $\sigma = \dot{V}_r/V_m$, so that constant σ implies constant $\dot{V}_r$.

The mean age of mantle reprocessing is defined as

$$\langle\tau\rangle = \frac{1}{V_m} \int_0^t \tau\ v(\tau,t)\ d\tau \qquad (10.5)$$

It follows from (10.3) and (10.5) in the limit as t goes to infinity that

$$\langle\tau\rangle = \frac{1}{\sigma} = \frac{V_m}{\dot{V}_r} \qquad (10.6)$$

Thus the mean age of mantle reprocessing, when the reprocessing rate is constant, is the mantle flux time, i.e., the time for the entire mantle volume, V_m, to flux through the melting region. We also found in the numerical calculations that the mean residence time, t_r, was approximated by the flux time t_f.

10.2 Scalings Assuming Constant Rate of Convection

At present, with a plate generation rate of 3 km^2/yr [Chase, 1972] and a degree of partial melting of 20% [Gast, 1968], the mean age from (10.1) and (10.6) is 10 b.y. if the whole mantle is being sampled and 3.5 b.y. if only the upper mantle is being sampled. These ages are quite large in comparison with the 1-2 b.y. age of the mantle estimated from isotope systematics [Brooks et al.,1976; Chase, 1981]. Alternatively, if we assume that d_m = 100 km, then the mean ages are 1 b.y. and 3 b.y. for upper and whole-mantle convection. The age distributions for these two cases are shown in Figure 10.1.

10.3 Mantle Residence Times on a Cooling Earth

Two time dependent quantities arise in the scaling of the residence times: the melting depth d_m and the areal plate velocity $\dot{A}$. The variation in plate or convective velocities was studied in Chapter 8. The depth of the mantle reprocessing region and how it varies with an evolving mantle geotherm are fairly uncertain. The time dependent melting depth will be parameterized in this section to explore how the factors which control melting under mid-ocean ridges also control the age distribution and the mean age of the mantle; a definitive scaled mean age cannot be realized with current constraints.

The temporal variation of d_m can be constrained if the mantle solidus and the temporal variation of the geotherm can be estimated. The solidi of candidate mantle rocks have a slope greater than the adiabat, so that as the mantle temperature increases, the depth at which the geotherm crosses the solidus increases [Sleep, 1979]. In Figure 10.2, average mantle geotherms for progressively higher average mantle temperatures are shown. Two solidi are also displayed and were estimated from the high pressure experiments on dry peridotite and pyrolite with 0.1% H_2O as summarized by Wyllie [1971] and Ringwood [1975] and extrapolated to depth with the theoretical solidus of Kennedy and Higgins [1972]. The large spread between the two solidi in Figure 10.2 is due to the effect of the water content of the mantle, which is uncertain. A very simple characterization of the increase of melting depth on internal temperature is

$$d_m = \phi(T - T_p) + d_p \tag{10.7}$$

where T_p and T are the temperatures at which the solidus and geotherm intersect (subscript p denoting the present) and ϕ and d_p are free parameters. The linear characterization is only an approximation. Three combinations of ϕ and d_p have been chosen. If the current degree of partial melting needed to make MORB is about 20% [Gast, 1968] and the thickness of oceanic crust is 6 km, then the present depth is $d_p \sim d_{oc}/F = 30$ km. To account for the uncertainty, the present depth is varied between 20 and 100 km. The depth-temperature slopes, ϕ, can be estimated from Figure 10.2 where the geotherms shown are 10% and 20% higher than the present. Depth-temperature slopes, ϕ, of melting of 0.2 to 0.6 km/K are reasonable.

A mean mantle temperature can be calculated from the average mantle heat flux. Because of the strong temperature dependence of silicate rheology [Carter, 1976], the time variation of temperature can be calculated approximately from a thermal history of the earth via [Davies, 1979]

$$\frac{T}{T_p} = \left(\frac{q}{q_p}\right)^{1/m} \tag{10.8}$$

where q is the mantle heat flux and m is a constant of about 10 [Davies, 1979]. Equation (10.8) concisely illustrates that temperature changes are strongly buffered against changes in heat flux.

The areal rate of plate generation must also be calculated from the heat flux of the mantle. As with the analysis of blob survival time, we assume an exponential thermal history; combining

(8.6) and (8.7), we find

$$\dot{A}(t) = \dot{A}_o \, e^{-2\gamma t} \qquad (10.9)$$

where $\dot{A}_o$ is the initial areal rate of plate generation. Substituting (10.7), (10.8), and (10.9) into (10.1), we find

$$\dot{V}_r = \dot{A}_p e^{-2\gamma(t-\tau_e)} [\phi T_p (e^{-\gamma(t-\tau_e)/m} - 1) + d_p] \qquad (10.10)$$

where τ_e is the age of the earth (taken here to be 4.5 b.y.).

Before using (10.2) and (10.10) to solve for the age distribution, we can integrate (10.10) and calculate how many times the equivalent mantle volume has been recycled as a function of age. Results for four combinations of parameter values are shown in Figure 10.3, if the whole mantle is being sampled. To convert to upper mantle values, multiply the ordinate values by 2.95. By inspecting curve 4, for example, in Figure 10.3, one can see that the equivalent to the entire mantle volume has passed through the oceanic crust/depleted lithosphere in the last 1.5 b.y., twice in the last 2 b.y., and four times in the last 3 b.y.

No simple analytical solution exists for the age distribution in the nonsteady state when $\dot{V}_r$ varies as in (10.10), however, the age distribution is easily calculated numerically by evaluating (10.2) and (10.10). As an initial condition, the mantle was assumed to be both isotopically and chemically homogeneous. In Figure 10.4 are shown age distributions for three of the cases shown in Figure 10.3 (similar line types in Figures 10.3 and 10.4 correspond to the same model). For the cases with the shorter thermal half-life the age distribution is sharper and the mean age smaller (see below). Longer thermal half-lives result in less reprocessing: curves 1 and 2 both have a d_p = 20 km, but curve 1 has a thermal half-life of 1.5 b.y., while for curve 2 it is 1.5 times longer. Larger sampling depths result in greater rates of reprocessing: curves 1 and 3 both have the same thermal history, but the present sampling depth, d_p, for curve 3 is a factor of 5 greater. The age distributions shown in Figure 10.4 become much narrower on a cooling earth than on a steady-state earth (Figure 10.1). Moreover, for most parameter values, the age distributions are skewed to the last 2 b.y., because of the large amount of reprocessing before 2 b.y. ago.

This skewing of the age distributions is mostly a manifestation of (8.6): that convective velocities go as the square of the heat flux.

The mean age of reprocessing, $\langle\tau\rangle$, can be found by carrying out the integration of (10.5) on the age distribution. Listed in Table 10.1 are mean ages for convection confined both to the upper mantle and to the whole mantle. Note that the mean ages are not the same age (and actually less than the age) since one mantle volume has been processed. The half-life of the heat flux and the constants ϕ and d_p of (10.7) are also varied. Despite the large spread between both input parameters and their resulting curves in Figure 10.3, the mean ages of reprocessing only vary between 500 m.y. and 2 b.y. (i.e., by a factor of 4). One reason for the small spread is the very vigorous reprocessing of the mantle before 2 b.y. (displayed for most parameter values, Figure 10.3); this effectively obliterates any age contribution prior to 2 b.y. B.P., and hence the spread in the mean ages is less than might be expected from a large uncertainty in the input parameters.

Despite the uncertainty surrounding the depth of sampling and how it has varied in the past, the greatest contribution to recycling is due to the increased convective velocities of the past. This is shown when the dependence of partial melt depth on temperature is ignored (by letting ϕ vanish): the mean ages increase only by a factor of 20 - 30% when the recycling depth remains constant. Thus unless vastly different length scales of melting are found to exist beneath ridges, the ages presented here should be representative of mantle reprocessing dominated by convective velocities.

10.4 Effect of Depth-Dependent Viscosity

If the ambient fluid has depth-dependent viscosity some additional mixing phenomena occur. In particular, the sampling time of recycled material increases as the viscosity of the deeper regions increase. However, if the viscosity contrast is made too large (perhaps $\bar{\eta}/\eta_0 > 50$) most of the recycled material is sampled before it has time to be stirred into the deeper parts; the sampling time decreases as the depth-scale of viscosity decreases. On the other hand, the sampling time for a layer of tracers initially at the base can increase indefinitely with increasing viscosity. Definitive scalings cannot be made because the exact dependence of the sampling time of recycled material on either $\bar{\eta}/\eta_0$ or $\bar{\eta}_L/\bar{\eta}_U$ is unknown.

The sampling time for basal tracers as a function of viscosity contrast is known, e.g. as presented originally as Figure 9.4, and a crude scaling can be made. It was determined in the previous section, for reasonable parameters, that $\langle\tau\rangle$ was controlled more strongly by the the time dependence of the convection velocity than by the time dependence of the sampling depth. Assuming a constant sampling depth, the ordinate of Figure 10.5 (Figure 9.4), in transit times, is scaled using (8.9), the scaled time to make that many transits of the mantle with an exponential thermal history. The scalings are made using a thermal half-life of 2 b.y. The dashed line in Figure 10.5 is the predicted effect of halving d_s from 0.05 to 0.025. For $\beta > 2$, the time to sample 75% of the tracers scales to > 3 b.y. and if d_s < 75 km, the sampling times scale to > 4 b.y. This clearly shows that a significant fraction of material can escape sub-ridge sampling over most of the age of the earth, despite whole-mantle convection.

Shown in Table 10.2 are the number of transit times to sample 75% of the tracers. This time is chosen in lieu of an exponential decay constant because single exponentials did not fit the sampling time versus tracer curves for all cases. As shown, the time to sample the basal and recycled tracers is the same for both the constant viscosity case and the case with a mild increase of viscosity with depth, β=2. However, for the case with the rather strong increase in viscosity with depth, β=3.5 ($\bar{\eta}/\eta_0$ = 60), there is a large difference between the time to sample the recycled tracers (120 transit times) compared to the time to sample the basal tracers (280 transit times). As shown in Table 10.2, when these times are scaled to the mantle assuming an exponential thermal history, there is a ≈ 1 b.y. time difference. This obviously has important implications for the geochemical evolution of the mantle: there can be a significant difference in "age" between the lower parts of the fluid and the upper parts despite flow through the whole layer.

10.5 Effect of Intrinsic Density

The intrinsic density of recycled material also prolonged the residence times. Four "scenarios" were considered for scalings in Chapter 9: separation of oceanic crust from the depleted lithosphere or oceanic crust and lithosphere remain layered after subduction for both upper mantle and whole-mantle convection. For three of the four scenarios listed in Table 9.3, $\lambda_m^{-1}/t_f < 1.6$ and this is not considered significant as the scaled mean ages would still be in the range 1 to 2 b.y. for whole-mantle convection. However, for the case of the complete separation of crust from the underlying lithosphere, a large increase in residence time was found, $\lambda_m^{-1}/t_f = 3.3$, for a whole-mantle Rayleigh number. The residence time increases because the recycled material formed high density patches under the warm upwelling areas; although not clearcut, two (interacting) reservoirs develop. Assuming a constant sampling depth, d_s, of 0.05 (150 km): one flux time scales to 2 b.y. using Figure 8.2, while 3.3 flux times scale to almost 3.5 b.y. Thus for this rather extreme case, there is a strong distinction between average age of reprocessing and average age of recycled material. It seems unlikely, however, that the ages could be increased by this much, as this requires the complete separation of oceanic crust from the underlying mantle. Any significant increase in residence time of recycled material will be limited by how rapidly crust can separate from the lithosphere.

TABLE 10.1

Calculated Mean Ages of the Mantle

Heat Flux Half-Life, b.y.	ϕ, km/K	d_p, km	Initial Depth p.m., km	Curve in Figures 10.3 & 10.4	$\langle\tau\rangle$, b.y.	
					Whole Mantle	Upper Mantle
1.50	0.2	20	120	(1)	1.56	1.05
2.25	0.2	20	84	(2)	2.04	1.31
1.50	0.4	30	230		1.29	0.83
2.25	0.4	30	157		1.66	1.03
1.50	0.6	100	400	(3)	0.89	0.50
2.25	0.6	100	291	(4)	1.09	0.57
2.00	0.2	20	92		1.89	
2.00	0.0	20	20		2.49	
2.00	0.4	30	175		1.54	
2.00	0.0	30	30		2.13	
2.00	0.6	100	317		1.03	
2.00	0.0	100	100		1.21	

TABLE 10.2
Scaled times for Depth-Dependent Cases

Viscosity model		Time to sample 75% of tracers $d_s < 150$ km			
		recycled tracers		basal tracers	
β	$\bar{\eta}/\eta_o$	transit times	B.y.*	transit times	B.y.*
0	1	110	2.4	128	2.7
2	10	220	3.3	220	3.3
3.5	60	120	2.5	280	3.6

* Model assumes exponential thermal history with, 2 b.y. half-life.

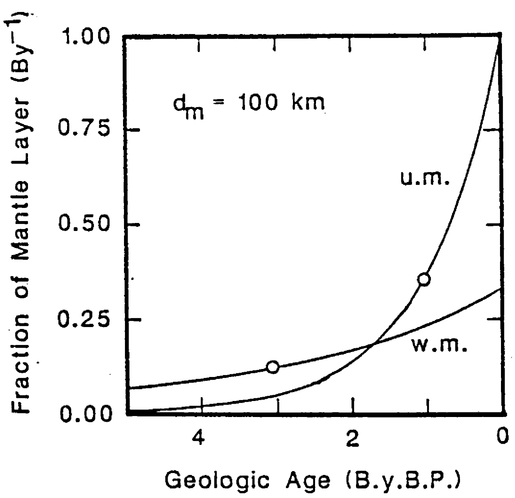

Fig. 10.1 Age distributions of mantle rocks since last reprocessing beneath mid-ocean ridges. The areal rate of convection has been held constant at 3 km^2/yr and D_m = 100 km. The open circles on each curve denote the mean age of reprocessing, $\langle \tau \rangle$.

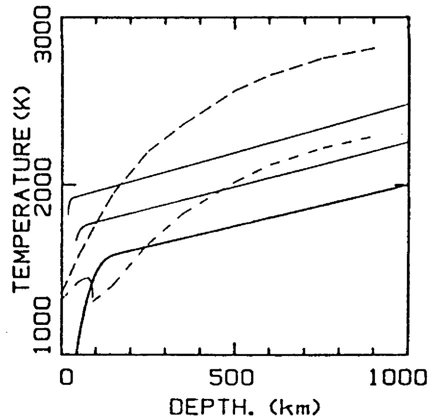

Fig. 10.2 Average mantle geotherms and estimates of mantle melting curves. The lowest geotherm (heavy solid line) is an estimate of the present average oceanic mantle. Higher geotherms are for 10% and 20% higher mean temperatures. Solidi for 0.1% H_2O saturated pyrolite (short-dashed line) and dry peridotite (long-dashed line) are estimated from Ringwood [1975] and Wyllie [1971] and extrapolated to depth with the theoretical solidi of Kennedy and Higgins [1972]. The figure illustrates that as the mantle has cooled, the depth of the melting beneath ridges has probably become shallower.

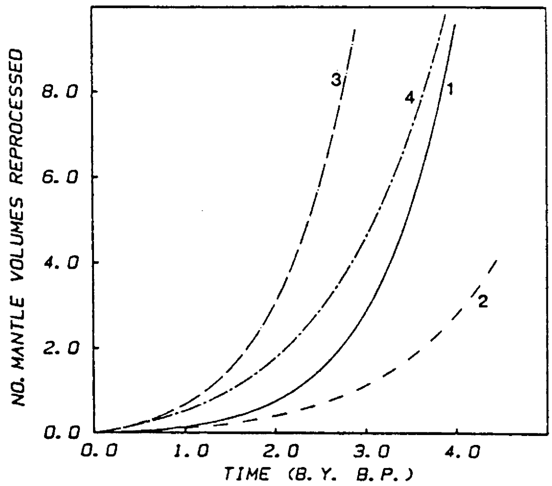

Fig. 10.3 Number of times the equivalent to the whole mantle has passed through the oceanic crust/depleted lithosphere by an integration of (10.10) back in time for four sets of parameter values; the parameters describing each curve are given in Table 10.1. The curves become very steep earlier than 2 b.y. B.P. (illustrating very rapid recycling) due to the dependence of velocity on heat flux to the second power.

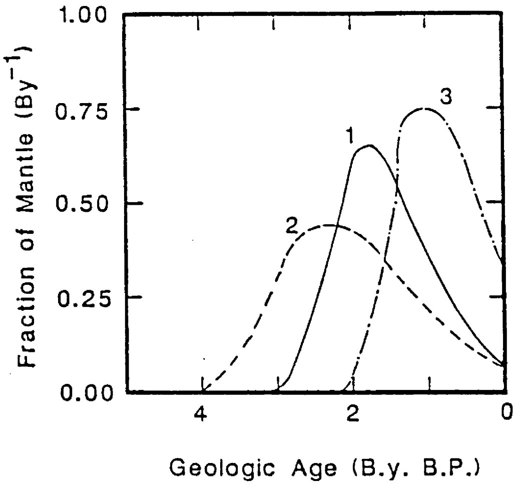

Fig. 10.4. Age distributions of mantle rocks since last reprocessing beneath mid-ocean ridges, assuming whole-mantle convection. The parameters describing each curve are given in Table 10.1. Similar line types in Figure 10.3 correspond to same model.

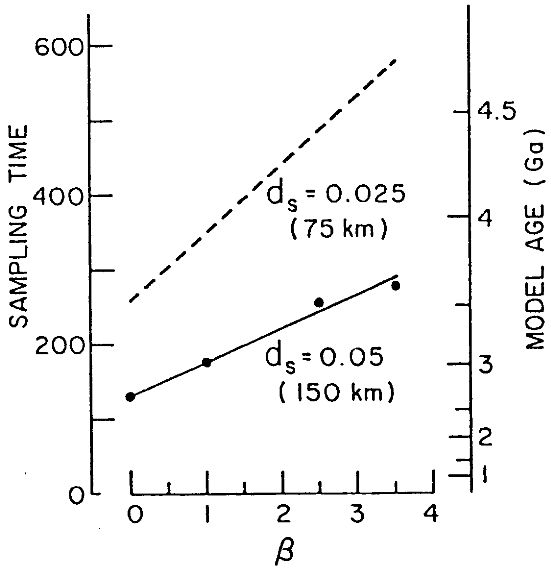

Fig. 10.5. Time sample 75% of the basal tracers as a function of β (e.g. $\eta = 10\beta^{(1-y)}$). This figure was originally presented as Figure 9.4. The left ordinate (in transit times) has been scaled using (8.9) and a thermal half-life of 2 b.y.

CHAPTER 11

SUMMARY AND CONCLUSIONS

The formation and cooling of the oceanic lithosphere accounts for most of mass and heat transfer within the earth and, therefore, the motion of the lithosphere is the dominant mode of mantle convection. Moreover, the dominant source of chemical heterogeneity within the mantle, i.e. the generation of oceanic crust at ridges and its subsequent subduction, is intimately coupled with this mode of convection. These statements pose important questions. How does plate-scale flow, i.e. the flow associated with the lithosphere, stir subducted lithosphere and crust (i.e. how is a thin sheet on the margin of an unsteady convection cell mixed) ? What is the ultimate fate of subducted crust and lithosphere? At what rate does plate-scale convection reprocess the mantle through the lithosphere (i.e. what is the residence time of mantle rocks) ?

In order to address these questions, the mixing of chemical heterogeneities has been investigated in two-dimensional flows constrained by dominant features of plate motions. These features are the unsteady kinematics of the plates and the introduction of chemical anomalies at subduction zones. Only the large-scale flow associated with plate motion has been studied; by choosing Rayleigh numbers scaled down from mantle values, small scale flow instabilities of the thermal boundary layers have been purposely suppressed. The effects of heterogeneities being smaller than the scale of flow, the introduction of heterogeneities as sheets on the margins of cells, the intrinsic chemical density of subducted fluid, and depth-dependent viscosity of the ambient fluid have all been investigated. Although the calculations are highly simplified, they should provide first-order approximations to mixing by plate-scale flow and provide a sound base for more realistic calculations. The following important results have been arrived at:

1. If a passive heterogeneity is mixed by scales of flow larger than the heterogeneity itself, then the heterogeneity is predominately stirred by laminar flow, even if the flow is unsteady. A small heterogeneity is stirred by unsteady flow and subsequently consists of large blobs (containing a large fraction of the fluid) connected

to long tendrils. Over time the surface area of the entire heterogeneity is dominated by the surface area of tendrils and the existence of blobs is obscured. After an initial period, the surface area of the heterogeneity increases exponentially and the average width decays exponentially, as predicted by a turbulent mixing law; the turbulent mixing law holds because tendrils are larger than the scale of flow and they are frequently advected into stagnation points and stirred by normal strains. However, the size of blobs decays much more slowly, in fact more slowly than predicted by laminar mixing. The size of blobs decay slowly because they are occasionally unmixed when they are transferred to adjacent convection cells. The time for the maximum sized heterogeneity to be stirred down to 10% of its initial size was about 220 transit times which scales to 13 b.y. in whole-mantle convection with a constant thermal history and to greater than 3 b.y. assuming a realistic thermal history.

2. If the fluid is injected as a thin sheet on the margin of an unsteady convection cell these mixing phenomena still hold because the thickness of the sheet is much smaller than the size of convection cells. When the perimeter of a thin sheet was defined by a material line, it was found that there were blobs on the order of the initial thickness persisting for at least 20 transit times. For unsteady thermal convection calculations, tracers were introduced below converging plate margins and it was found that significant clumps of tracers survived for up to 40 transit times and this survival time was shown to be insensitive to the particulars of plate evolution. This survival time scales to 560 m.y. and 2.4 b.y. for upper and whole-mantle convection, respectively. Using a realistic scaling model in which plate velocities were going much more rapidly in the past, 40 transit times scales to 470 m.y. (for upper mantle convection) and 1.4 b.y. (for whole-mantle convection).

3. The tracers, originally injected into the flow below trenches (converging margins), were removed near the ridge (diverging margin) in order to simulate the reincorporation of fractionated mantle into the lithosphere. The average time passive tracers are resident in the constant viscosity fluid from subduction to sampling is within 20% of the time expected for an area, equivalent to the box area, to flux through the sample region, the flux time. Residence times, which depend on sampling depth and the rate of convection, have

been scaled to obtain model mean ages of the mantle using realistic thermal histories. For a wide range of plausible parameters, model mean ages vary between 500 m.y. and 1.3 b.y. for upper mantle convection and between 900 m.y. and 2.3 b.y. for whole-mantle convection.

4. The effect which depth-dependent viscosity has on the stirring of passive heterogeneities has also been investigated. Exponential and layered viscosity distributions were incorporated into thermal convection calculations. In general, the survival time of heterogeneity increased as the viscosity of the deeper regions increased. The survival of clumps of tracers could be increased from the 40 transit times in constant viscosity fluids to ~60-100 transit times for cases with acceptable depth-dependent viscosity distributions (e.g. $\bar{\eta}/\eta_0$ ~ 20-60). These survival times scale to 2-3 b.y. assuming a realistic thermal history. Residence times were also increased with increased viscosity contrasts. It was also found that if $\bar{\eta}/\eta_0$ became larger than ~ 50, that the tracers were sampled before they could be stirred into the basal regions of flow; consequently, the scaled residence times cannot be increased to more than ~ 2 b.y. This contrasts with the stirring and sampling of a layer of passive tracers, initially at the base, where scaled sampling times range from 3 to > 4.5 b.y. for acceptable viscosity contrasts.

5. The recycled tracers were also given an intrinsic density in thermal convective flows. It was found that after stirring by the background flow, that tracers tended to segregate to the base of hot upwelling regions, with a greater amount of segregation taking place in internally heated flows compared to bottom heated ones. The residence times of tracers were increased. However, only for a density difference appropriate to the complete separation of subducted oceanic crust from the depleted lithosphere could any significant segregation take place. In the case of the whole-mantle convection scenario, the residence times were increased significantly to more than three times the value for completely passive material.

These results have clear and immediate implications for the relationship between the isotopic signature of mantle derived rocks and mantle convection. Chemical heterogeneities can survive as blobs in a convecting unlayered mantle for billions of years. Since isotopic systematics require that there are at least four [White, 1985] or five [Zindler and Hart, 1986] mantle component types or reservoirs, a two layered mantle would still require that chemical heterogeneities survive, within the layers, for hundreds of millions to billions of years. The results presented here show that heterogeneities can survive for such time-scales. Blob survival time is maximized in an unlayered system because the shear strain rate, the principle quantity controlling mixing, is less for thicker layers. If the purpose of a mantle model is to preserve chemical heterogeneity for billions of years, nothing is gained by invoking two mantle layers instead of one.

The average model age of mantle reprocessing is 1 to 2 b.y. for whole-mantle convection. Mean ages are primarily less than 2 b.y. because of the (most-likely) rapid convection rates prior to 2 b.y. ago. Moreover, most of the recycled fluid is still distinct (i.e. the heterogeneity is much larger than the length scale over which chemical diffusion would operate) and therefore the recycled fluid is capable of maintaining its chemical and isotopic identity for > 2 b.y. These reprocessing ages and survival times are consistent with observed isochrons: the 1.6 b.y. average age deduced for the source of MORB and OIB from Rb-Sr systematics [Brooks, et al., 1976], the 1.8 b.y. average Pb-Pb isochron of the source of oceanic basalts [Church and Tatsumoto, 1975], and the 1 to 2.5 b.y. range of Pb ages for the sources of individual oceanic island [Chase, 1981].

This correspondence between model ages and observed ages is consistent with the idea that the isotopic variation observed for mantle-derived basalts results from large-scale recycling driven by plate-scale thermal convection and is also consistent with the more specific hypothesis that the OIB source is recycled MORB [Chase, 1981; Hofmann and White, 1982].

The results also show that if oceanic crust separates from the underlying, depleted lithosphere (a possibility yet to be quantitatively evaluated, but unlikely to be very efficient) then it will efficiently segregate to the base of the convecting system, as hypothesized by Hofmann and White [1982]. Hofmann and White [1982] invoked this mechanism to "store" the crust in the mantle for 1-2 b.y. The results of the mixing of passive tracers reveals that no such extra storage time is needed, as the natural reprocessing time of whole-mantle convection with plausible thermal histories is 1 to 2 b.y.

The cases with depth-dependent viscosity illustrate that it is possible to have flow extending throughout the convecting region and have both a 1 to 2 b.y. mean age of recycled material, on the one hand, and have mantle material survive stirring for > 4.5 b.y., on the other. Primitive material can even survive in spite of a realistic thermal history wherein the mantle was convecting much more vigorously in the past. This "bimodality" of ages is consistent with Rb-Sr and Pb-Pb average MORB and OIB isochrons, on the one hand, and with the continuing flux of ^{3}He out of the mantle [Lupton and Craig, 1975] and the ^{129}Xe/^{130}Xe ratios in OIB and MORB [Allègre et al., 1983], on the other. The possibility that significant amounts of primitive material survives in spite of whole-mantle convection means that ^{3}He/^{4}He and ^{129}Xe/^{130}Xe systematics do not falsify whole-mantle convection as previously thought [Allègre et al., 1983; O'Nions and Oxburgh, 1983].

REFERENCES

Allègre, C. J., T. Staudacher, P. Sarda, and M. Kurtz, Constraints on evolution of earth's mantle from rare gas systematics, Nature 303, 762-766, 1983.

Anderson, D. L., The upper mantle transition region: ecologite?, Geophys. Res. Lett., 6, 433-435, 1979.

Anderson, D. L., Isotopic evolution of the mantle: a model, Earth Planet. Sci. Lett., 57, 13-24, 1982.

Batchelor, G. K., The effect of homogeneous turbulence on material lines and surfaces, Proc. Roy. Soc. Lond., A213, 349-366, 1952.

Batchelor, G. K., An Introduction to Fluid Mechanics, 615 pp., Cambridge University Press, New York, 1967.

Booker, J. R., Thermal convection with strongly temperature-dependent viscosity, J. Fluid Mech., 76, 741-754, 1976.

Brooks, C., S. R. Hart, A. W. Hofmann, and D. E. James, Rb-Sr mantle isochrons from oceanic regions, Earth Planet. Sci. Lett., 32, 51-61, 1976.

Brown, L., J. Klein, R. Middleton, I. S. Sacks, and F. Terra, ^{10}Be in island-arc volcanics and implications for subduction, Nature, 299, 718-720, 1982.

Burke, K., J. F. Dewey, and W. S. F. Kidd, Dominance of horizontal movements, arc and mirocontinental collisions during the later permobile regime, in The Early History of the Earth, edited by B. F. Windley, John Wiley, New York, pp. 113-129, 1976.

Carter, N. L., Steady state flow of rocks, Rev. Geophys. Space Phys., 14, 301-360, 1976.

Cathles, L. M., The Viscosity of the Earth's Mantle, 386 pp., Princeton University Press, Princeton, N.J., 1975.

Cazenave, A., Thermal cooling of the oceanic lithosphere: New constraints from geoid height data, Earth Planet. Sci. Lett., 70, 395-406, 1984.

Chase, C. G., The n-plate problem of plate tectonics, Geophys. J. R. Astron. Soc., 29, 117-122, 1972.

Chase, C. G., Extension behind island arcs and motions relative to hot spots, J. Geophys. Res. 83, 5385-5387, 1978.

Chase, C. G., Oceanic island lead: Two-stage histories and mantle evolution, Earth Planet. Sci. Lett., 52, 277-284, 1981.

Chase, C. G. and D. R. Sprowl, The modern geoid and ancient plate boundaries, Earth Planet. Sci. Lett., 62, 314-320, 1983.

Church, S. E., and M. Tatsumoto, Lead isotope relations in oceanic ridge basalts from the Juan da Fuca-Gorda ridge area, N.E. Pacific Ocean, Contri. Mineral. Pertrol., 53, 253-279, 1975.

Creager, K. C. and T. H. Jordan, Slab penetration into the lower mantle, J. Geophys. Res., 89, 3031-3049, 1984.

Creager, K. C. and T. H. Jordan, Slab penetration into the lower mantle beneath the Mariana and other western Pacific island arcs, J. Geophys. Res., 91, 3573-3586, 1986.

Crough, S. T., Hotspot swells, Ann. Rev. Earth Planet. Sci., 11, 165-193, 1983.

Davies, G. F., Whole-mantle convection and plate tectonics, Geophys. J. Roy. Astron. Soc., 49, 459-486, 1977.

Davies, G. F., Thickness and thermal history of continental crust and root zones, Earth Planet. Sci. Lett., 44, 231-238, 1979.

Davies, G. F., Review of oceanic and global heat flow estimates, Rev. Geophys. Space Phys., 18, 718-722, 1980a.

Davies, G. F., Thermal histories of convective earth models and constraints on radiogenic heat production in the earth, J. Geophys. Res., 85, 2517-2530, 1980b.

Davies, G. F., Geophysical and isotopic constraints on mantle convection: An interim synthesis, J. Geophys. Res., 89, 6017-6060, 1984.

Davies, G. F., Mantle convection under simulated plates: Effects of heating modes and ridge and trench migration, and implications for the core-mantle boundary, bathymetry, the geoid, and Benioff zones, Geophys. J. R. Astron. Soc., 84, 153-183, 1986a.

Davies, G. F., Wadati-Benioff zone shapes and mantle flow structure (abstract), EOS Trans. American Geophys. Union, 67, 381, 1986b.

De Paolo, D. J., Crustal growth and mantle evolution: Inferences from models of element transport and Nd and Sr isotopes, Geochim. Cosmom Acta, 44, 1185-1196, 1980.

De Paolo, D. J. and G. J. Wasserburg, Inferences about magma sources and mantle structure from variations of ^{143}Nd/^{144}Nd, Geophys. Res. Lett., 3, 743-746, 1976.

Duncan, R. A. and W. Compston, Sr-isotopic evidence for an old mantle source region for French Polynesian volcanism, Geology, 4, 728-732, 1976.

Eckart, C., An analysis of the stirring and mixing processes in incompressable fluids, J. Marine Res., 7, 265-275, 1948.

Gast, P. W., Trace element fractionation and the origin of tholeiitic and alkaline magma types, Geochim. Cosmich. Acta, 32, 1057-1086, 1968.

Goldstein, S., A. Zindler, and E. Jagoutz, Evolution of the mantle-crust system: Quantitative geochemical modeling of Pb, Sr, and Nd isotopic systematics (abstract), EOS Trans. Am. Geophys. Un., 63, 460, 1982.

Griffiths, R. W., Dynamics of mantle thermals with constant buoyancy or anomalous internal heating, Earth Planet. Sci. Lett., 78, 435-446, 1986.

Gurnis, M., Quantitative bounds on the size spectrum of isotopic heterogeneity within the mantle, Nature, 323, 317-320, 1986.

Gurnis, M., and G. F. Davies, Simple parametric models of crustal growth, J. Geodyn., 3, 105-135, 1985.

Gurnis, M. and G. F. Davies, Numerical study of high Rayleigh number convection in a medium with depth-dependent viscosity, Geophys. J., 85, 523-541, 1986.

Hager, B. H., Subducted slabs and the geoid: Constraints on mantle rheology and flow, J. Geophys. Res., 89, 6003-6015, 1984.

Hager, B. H., and R. J. O'Connell, Kinematic models of large-scale flow in the earth's mantle, J. Geophys. Res., 84, 1031-1048, 1979.

Hager, B. H., and R. J. O'Connell, A simple global model of plate dynamics and mantle convection, J. Geophys. Res., 86, 4843-4867, 1981.

Hart, S. R., A large-scale isotopic anomaly in the southern hemisphere mantle, Nature, 309, 753-757, 1984.

Heestand, R. L. and S. T. Crough, The effect of hot spots on the oceanic age-depth relation, J. Geophys. Res., 86, 6107-6114, 1981.

Heller, J. P., An unmixing demonstration, Am. J. Phys., 28, 348-353, 1960.

Hilde, T. W. C., Sediment subduction versus accretion around the Pacific, Tectonophysics, 99, 381-397, 1983.

Hilde, T.W.C., S. Uyeda, and K. L. Kroenke, Evolution of western Pacific and its margins, Tectonophysics, 38, 145-165, 1977.

Hoffman, N. R. A., and D. P. McKenzie, The destruction of geochemical heterogeneities by differential fluid motions during mantle convection, Geophys. J. R. Astron. Soc., 82, 163-206, 1985.

Hofmann, A. W. and S. R. Hart, An assessment of local and regional isotopic equilibrium in the mantle, Earth Planet. Sci. Lett., 38, 44-62, 1978.

Hofmann, A. W., and W. M. White, Mantle plumes from ancient oceanic crust, Earth Planet. Sci. Lett., 57, 421-436, 1982.

Houston, M. H. and J. Cl. DeBremaecker, ADI solution of free convection in variable viscosity fluid, J. Comp. Phys., 16, 221-234, 1974.

Hussong, D. M., and S. Uyeda, Tectonic processes and the history of the Mariana arc: A synthesis of the results of Deep Sea Drilling Project Leg 60, in Initial Rep. Deep Sea Drilling Proj., 60, 909-929, 1982.

Isacks, B. and P. Molnar, Distribution of the descending lithosphere from a global survey of focal-meachanism solutions of mantle earthquakes, Rev. Geophys. Space Phys., 9, 103-174, 1971.

Isacks, B., J. Oliver, and L. R. Sykes, Seismology and the new global tectonics, J. Geophys. Res., 73, 5855-5899, 1968.

Jarvis, G. T., Time-dependent convection in the earth's mantle, Phys. Earth Planet. Int., 36, 305-327, 1984.

Jordan, T. H., Lithospheric slab penetration into the lower mantle beneath the Sea of Okhotsk, J. Geophys., 43, 473-496, 1977.

Jurdy, D. M., An alternative model for early Tertiary absolute plate motions, Geology, 6, 469-472, 1978.

Kennedy, G. C., and G. H. Higgins, Melting temperatures in the earth's mantle, Tectonophysics, 13, 209-228, 1972.

Kurz, M. D., W. J. Jenkins, and S. R. Hart, Helium isotopic systematics of oceanic islands and mantle heterogeneity, Nature, 297, 43-47, 1982.

Kurz, M. D., W. J. Jenkins, S. R. Hart, and D. Clague, Helium isotopic variations in volcanic rocks from Loihi Seamount and the Island of Hawaii, Earth Planet. Sci. Lett., 66, 388-406, 1983.

Landau, L. D. and E. M. Lifshitz, Fluid Mechanics, Pergamon Press, New York, 536 pp., 1959.

Lupton, J. E., Terrestrial inert gases: Isotopic tracer studies and clues to primordial components in the mantle, Ann. Rev. Earth Planet. Sci., 11, 371-414.

Lux, R. A., The effect of a moving lithospheric plate on convection in the earth's interior, 87 pp., Thesis, University of Rochester, Rochester, New York, 1978.

McKenzie, D., Finite deformation during fluid flow, Geophys. J. R. Astr. Soc., 58, 689-715, 1979.

McKenzie, D. P., J. M. Roberts, and N. O. Weiss, Convection in the earth's mantle: Towards a numerical simulation, J. Fluid Mech., 62, 465-538, 1974.

McKenzie, D. P. and N. O. Weiss, Speculations on the thermal and tectonic history of the earth, Geophys. J. R. Astron. Soc., 42, 131-174, 1975.

McKenzie, D., A. Watts, B. Parsons, and M. Roufosse, Planform of mantle convection beneath the Pacific Ocean, Nature, 288, 442-446, 1980.

McKenzie, D. P. and F. M. Richter, Parameterized thermal convection in layered region and the thermal history of the earth, J. Geophys. Res., 86, 11667-11680, 1981.

Meijer, A., Pb and Sr isotopic data bearing on the origin of volcanic rocks from the Mariana island-arc system, Geol. Soc. Am, Bull., 87, 1358-1369, 1976.

Moore, D. R. and N. O. Weiss, Two-dimensional Raylei gh-Bènard convection, J. Fluid Mech., 58, 289-312, 1973.

Morgan, J. W., Convection plumes in the lower mantle, Nature, 230, 42, 1971.

Nakada, M. and K. Lambeck, Glacial rebound and relative sealevel variations: a new appraisal, Geophys. J. Roy. Astron. Soc., submitted, 1986.

O'Connell, R. J., Pleistocene glaciation and the viscosity of the lower mantle, Geophys. J. Roy. Astron. Soc., 23, 299-327, 1971.

O'Connell, R. J., On the scale of mantle convection, Tectonophysics, 38, 119-136, 1977.

O'Connell, R. J., and B. H. Hager, On the thermal state of the earth, in Physics of the Earth's Interior, edited by A. Dzeiwonski and E. Boschi, North-Holland, Amsterdam, 270-317, 1980.

O'Connell, R. J., and B. H. Hager, Velocity anomalies, convection, heat transport and the viscosity of the lower mantle (abstract), EOS Trans. Am. Geophys. Un., 65, 1093, 1984.

Olson, P. and I. S. Nam, Formation of seafloor swells by mantle plumes, J. Geophys. Res., 91, 7181-7192, 1986.

Olson, P., D. A. Yuen, and D. Balsiger, Mixing of passive heterogeneities by mantle convection, J. Geophys. Res., 89, 425-436, 1984a.

Olson, P., D. A. Yuen, and D. Balsiger, Convective mixing and the fine structure of mantle heterogeneity, Phys. Earth Planet. Int., 36, 291-304, 1984b.

O'Nions, R. K. and E. R. Oxburgh, Heat and helium in the earth, Nature, 306, 429-431, 1983.

O'Nions, R. K., N. M. Evensen, and P. J. Hamilton, Geochemical modeling of mantle differentiation and crustal growth, J. Geophys. Res., 84, 6091-6101, 1979.

Parmentier, E. M., D. L. Turcotte, and K. E. Torrance, Studies of finite amplitude non-Newtonian thermal convection with application to convection in the earth's mantle, J. Geophys. Res., 81, 1839-1846, 1976.

Parsons, B. and J. G. Sclater, An analysis of the variation of ocean floor batymetry and heat flow with age, J. Geophys. Res., 82, 803-827, 1977.

Peltier. W. R., Ice age geodynamics, Ann. Rev. Earth Planet. Sci., 9, 199-225, 1983.

Reisberg, L. and A. Zindler, Extreme isotopic variability in the upper mantle: Evidence from Ronda, Earth Planet. Sci. Lett., submitted, 1986.

Richards, M. A. and B. H. Hager, The earth's geoid and the large-scale structure of mantle convection, in Proc. NATO Adv. Study Inst., edited by S. K. Runcorn, in press, 1986.

Richter, F. M., Mantle convection models, Ann. Rev. Earth Planet. Sci., 6, 9-19, 1978.

Richter, F. M., Time and space scales of mantle convection, in Patterns of Change in Earth History, edited by H. D. Holland and A. F. Trendall, pp. 271-289, Dahlem Konferenzen, Berlin, 1984.

Richter, F. M., S. F. Daly, and H.-C. Nataf, A parameterized model for the evolution of isotopic heterogeneities in a convecting system, Earth Planet. Sci. Lett., 60, 178-194, 1982.

Richter, F. M. and N. M. Ribe, On the importance of advection in determining the local and isotopic composition of the mantle, Earth Planet. Sci. Lett., 43, 212-222, 1979.

Ringwood, A. E., Composition and Petrology of the Earth's Mantle, 618 pp., McGraw-Hill, New York, 1975.

Ringwood, A. E., Phase transformations and differentiation in subducted lithosphere: Implications for mantle dynamics, basalt petrogenesis, and crustal evolution, J. Geol., 90, 611-643, 1982.

Roache, P. J., Computational Fluid Mechanics, Hermosa Publishers, Albuquerque, N.M., 446 pp., 1982.

Sammis, C. G., J. C. Smith, G. Schubert, and D. A. Yuen, Viscosity-depth profile of the earth's mantle: Effects of polymorphic phase transitions, J. Geophys. Res., 82, 3747-3761, 1977.

Schroeder, W., The empirical age-depth relation and depth anomalies in the Pacific Ocean basin, J. Geophys. Res., 89, 9873-9883, 1984.

Schubert, G. and D. L. Turcotte, One-dimensional model of shallow mantle convection, J. Geophys. Res., 77, 945-951, 1972.

Schubert, G., D. Stevenson, and P. Cassen, Whole planet cooling and the radiogenic heat source content of the earth and moon, J. Geophys. Res., 85, 2531-2538, 1980.

Sleep, N. H., Thermal history and degassing of the Earth: Some simple calculations, J. Geology, 87, 671-686, 1979.

Stacey, F. D., Physics of the Earth, 2nd ed., 414 pp., John Wiley, New York, 1977.

Sun, S.-S., Lead isotopic study of young volcanic rocks from mid-ocean ridges, oceanic islands, and island arcs, Phil. Trans. R. Soc. Lond., A297, 409-445, 1980.

Sun S.-S., and G. N. Hanson, Evolution of the mantle: Geochemical evidence from alkali basalts, Geology, 3, 297-302, 1975.

Swarztauber, P. N. and R. Sweet, Efficient FORTRAN subprograms for the solution of elliptic partial differential equations, Report No. NCAR-TN/IA-109, National Center for Atmospheric Research, Boulder, CO., 1975.

Sweet, R. A., A generalized cyclic reduction algorithm, SIAM J. Numer. Anal., 11, 506-520, 1974.

Tatsumoto, M., Isotopic composition of lead in oceanic basalts and its implication to mantle evolution, Earth Planet. Sci. Lett., 38, 63-87, 1978.

Torrance, K. E. and D. L. Turcotte, Thermal convection with large viscosity variations, J. Fluid Mech., 47, 113-125, 1971.

Turcotte, D. L., On the thermal evolution of the earth, Earth Planet. Sci. Lett., 48, 53-58, 1980.

Turcotte, D. L., and E. R. Oxburgh, Finite amplitude convection cells and continental drift, J. Fluid Mech., 28, 29-42, 1967.

Turcotte, D. L. and G. Schubert, Geodynamics: Applications of continuum mechanics to geological problems, 450 pp., John Wiley, New York, 1982.

Vassiliou, M. S., B. H. Hager, and A. Raefsky, The distribution of earthquakes with depth and stress in subducting slabs, J. Geodynamics, 1, 11-28, 1984.

Von Huene, R., M. Langseth, N. Nasu, and H. Okada, A summary of Cenozoic tectonic history along the IPOD Japan Trench, Geol. Soc. Am. Bull., 93, 829-846, 1982.

Weertman, J., The creep strength of the earth's mantle, Rev. Geophys. Space Phys., 8, 145-168, 1970.

White, W. M., Sources of oceanic basalts: Radiogenic isotopic evidence, Geology, 13, 115-118, 1985.

White, W. M., and A. W. Hofmann, Sr and Nd isotope geochemistry of oceanic basalts and mantle evolution, Nature, 296, 821-825, 1982.

White, W. M., and J. Patchett, Hf-Nd-Sr isotopes and incompatible element abundances in island arcs: Implications for magma origins and crust-mantle evolution, Earth Planet. Sci. Lett., 67, 167-185, 1984.

Wyllie, P. J., The Dynamic Earth, 415 pp., John Wiley, New York, 1971.

Yuen, D. A., W. R. Peltier, and G. Schubert, On the existence of a second scale of convection in the upper mantle, Geophys. J. R. Astron. Soc., 65, 171-190, 1981.

Zindler, A. and S. Hart, Chemical geodynamics, Ann. Rev. Earth Planet. Sci., 14, 493-570, 1986.

Zindler, A., H. Staudigel, and R. Batiza, Isotope and trace element geochemistry of young Pacific sea mounts: Implications for the scale of upper mantle heterogeneity, Earth Planet. Sci. Lett., 70, 175-195, 1984.